Non-invasive, silicon-based beam monitor for medical accelerators

Thesis submitted in accordance with the requirements of the University of Liverpool for the degree of Doctor in Philosophy

by

Roland Schnuerer

June 2020

"The time is always right to do what is right."

— Martin Luther King, Jr., 1929-1968

Contents

Acknowledgements **V**

Abstract **VII**

1 Introduction **1**

1.1 Impact of cancer on society 1
1.2 History of the project 3
1.3 Thesis outline and objectives 7

2 State of the art of radiotherapy **11**

2.1 Physics of radiotherapy 12
2.1.1 Interaction of ionising radiation in matter 12
2.1.2 Dose distribution of the Bragg-curve 17
2.1.3 Proton beam halo 20
2.2 Medical accelerators 22
2.2.1 Cyclotrons 22
2.2.2 Modulation of the energy 25
2.2.3 Delivery modes of proton beams 25
2.3 Treatment room 30
2.4 The MC40 proton beamline at the University of Birmingham 31
2.5 Summary 34

3 Beam monitoring for medical accelerators **35**

3.1 Ionisation chambers 39
3.1.1 Applications of ionisation chambers in radiotherapy 40
3.2 Film 44
3.3 Silicon semiconductor detectors 46
3.3.1 Principles of silicon semiconductors 46
3.3.2 Current technologies for radiotherapy 49

3.4 Summary . . . 52

4 The LHCb VELO detector modules 53

4.1 LHCb VELO technology . . . 54

4.1.1 Sensor . . . 54

4.1.2 Readout electronics . . . 58

4.1.3 Trigger and Timing control for the LHCb VELO detector . . 63

4.2 System adaptations of the stand-alone LHCb VELO detector system for medical accelerators . . . 66

4.2.1 Requirements for the VELO detector modules in a clinical proton beamline . . . 66

4.2.2 Adaptations for a clinical environment . . . 67

4.2.3 Electronics and hardware changes . . . 69

4.2.4 Post-processing software platform . . . 73

4.3 Summary . . . 79

5 Implementation of the LHCb VELO detector modules at the MC40 proton beamline at the University of Birmingham 81

5.1 Setup of the VELO detector modules at the MC40 proton beamline 81

5.1.1 Requirements and aims for the irradiation study . . . 83

5.2 Results . . . 85

5.2.1 Preliminary beam parameter consideration . . . 86

5.2.2 Impact of proton irradiation on the VELO detector modules 91

5.2.3 Phase scan . . . 95

5.2.4 Beam current measurements . . . 96

5.2.5 Beam profile measurements . . . 103

5.3 Summary . . . 118

6 Beam Halo to Dose correlation 119

6.1 Summary . . . 126

7 Discussion 127

7.1 The LHCb VELO detector modules as a beam monitor in a proton beamline . . . 127

7.1.1 Evaluation of the measurement results . . . 127

7.1.2 Advantages and challenges of the LHCb VELO detector modules as a proton beam monitor . . . 129
7.1.3 Possibilities for improvement of the stand-alone detector system . . . 130
7.1.4 Assessment of the LHCb detector modules as a proton beam monitor . . . 131
7.2 The impact of the LHCb VELO detector modules of current and future beamlines and beam delivery systems . . . 133
7.2.1 Detector systems for current and future beamlines . . . 135
7.3 Summary . . . 137

8 Conclusion **139**
8.1 The LHCb VELO detector modules as a non-invasive, silicon-based beam monitor for medical accelerators . . . 139
8.2 Outlook . . . 141

List of Abbreviations **147**

List of Figures **151**

List of Tables **159**

Bibliography **161**

Acknowledgements

First, I would like to thank my supervisor Prof. Carsten Welsch for giving me the opportunity to carry out this interesting project and enabling me to take part in the European network Optimisation of Medical Accelerator (OMA), which was a big part in my personal and professional development. Also, I want to express my gratitude to my supervisors Dr. Javier Resta-Lopez and Dr. Jason Parsons for their support and valuable discussions.

As part of the Quasar group, I would like to thank its members for all the good moments and laughs we shared and especially for the cake meetings every Friday. Special thanks are going to Jacinta Yap and Dr. Hao Zhang for their continuous help and support during my work and Dr. Joseph Wolfenden for proofreading my thesis. Also, I would like to thank the members of the OMA network for the great collaborations and all the activities we took part in.

My deepest gratitude extends to Dr. Tomasz Szumlak, AGH, Krakow, Dr. Guido Haefeli and Dr. Oliver Girard, EPFL, Lausanne. Without their technical support to enhance the VELO technology for medical accelerators, this work would not have been possible.

I would like to thank Dr. Tony Smith, Dr. David Hutchcroft, Dr. Karol Hennessy, University of Liverpool, Jan Buytaert and Dr. Kazu Akiba, CERN for their technical expertise of the LHCb VELO detector modules and for the fruitful discussions around it.

To the fantastic team of the MC40 cyclotron, University of Birmingham, especially Dr. Tony Price and Ben Phoenix, I would like to thank them for supporting the measurements and helping to make them a success. My gratitude also goes to Andrzej Kacperek from the Clatterbridge Cancer Centre, UK for the continuous interest in the project and his shared expertise.

To my parents, brother, family and friends, who I am proud to have in my life, my dearest thanks for making my life easier and for inspiring me to persevere along the way. I am grateful to have shared most of my time during this PhD project with my lovely partner Maddy, who always makes me smile.

Abstract

In proton beam therapy knowledge of the detailed beam properties is essential to ensure effective dose delivery to the patient. Clinical settings currently implement interceptive ionisation chambers which require daily calibration and suffer from slow response times. With new and emerging treatment techniques using ultra high dose rates, there is a demand for the development of novel beam monitors, which are fast, non-invasive and calibration-free.

This work presents a new non-invasive method for online dose monitoring. It is based on the multi-strip silicon sensor LHCb VELO (VErtex LOcator), developed originally for the LHCb experiment at CERN. The semi-circular detector geometry offers the possibility to correlate the beam intensity through halo measurements without interfering the beam core. Several adaptations needed to be carried out to transfer this technology from the CERN environment to a stand-alone setup. This included the development of a venting and cooling system for safe operation in air. A positioning system was also developed for secure and precise handling of the modules.

The VELO detector modules were implemented at the 40 MeV proton beamline at the University of Birmingham, UK and synchronised with an ionisation chamber and the RF cyclotron frequency. This required a modification to the timing control of the readout boards. Proton beams with beam currents, from 0.2 nA to 6 nA, and different beam sizes, from a diameter of 7 mm to 20 mm, were precisely measured online using only the beam halo information.

Experimental results demonstrate the linearity, accuracy, reproducibility and sensitivity of the VELO detector modules for a suitable use as a beam monitor. The standard deviation of the registered hits are very low and equal or below 1%. Furthermore, the results were used to derive a characteristic beam Halo to Dose relationship via comparison with beam tracking GEANT4 simulations and EBT3 GAFchromic film measurements.

These results have demonstrated the applicability of the VELO detector modules as a beam monitor for medical accelerators, however the outdated electronics hardware and pre-processing software make more improvements difficult and would highly benefit from a redesign.

1 Introduction

1.1 Impact of cancer on society

In 2018, 17 million new cases of cancer were registered worldwide, where 52% of the cases were diagnosed in men. 9.6 million people died from cancer, making it the second largest cause of death. Europe has a share of 20.3% of all cancer related deaths yet has only 9% of the worldwide population; thus it is a big impact on society. The most common cancers, which are diagnosed in more than 40% of all incidents are: lung, with the highest death rate of 18.4%; female breast with the fifth highest death rate of 6.6%; bowel and prostate cancer, corresponding to 3.8% of all deaths. Worldwide, cancer incidents are estimated to rise by 61% by 2040, which corresponds to 27.5 million new cases of cancer each year. The increasing cancer rate is based on several factors; from population growth and ageing, to changes in social and economic development. To tackle these trends, major effort needs to be undertaken to advance cancer treatment and technology, as well as changing habits in society regarding physical activity and a well-balanced diet [1, 2].

The three most common and most available cancer treatment options are surgery, radiotherapy and chemotherapy. Emerging treatment types are focussing on targeting the tumour more specifically, such as immunotherapy [3].
Radiotherapy is used in approximately 50% of all cancer cases and is separated into uncharged radiation, such as gamma or X-ray radiation, and charged particle radiation, such as electrons, protons or heavier ions. Charged particle radiation therapy is becoming increasingly popular, offering more precise tumour irradiation, sparing more healthy tissue in the process. The first proposed medical use of protons for cancer therapy was published by Robert R. Wilson in 1946 [4]. Although significant advances have been made, proton therapy has still not maximised the

health care benefits it is capable of and extensive research and development programs are necessary to address these challenges. Further work is needed to: shrink the size of the proton therapy facilities, which are three times more expensive than conventional X-ray radiotherapy systems; reduce the uncertainty margin during the treatment through better instrumentation and image guidance; make proton therapy more available to the public by health care providers [5]. Amongst the challenges in accelerator technology and facility design, effective monitoring of the beam for quality assurance, treatment monitoring and overall machine and patient safety is of critical importance. It is estimated, that 10% of the total medical accelerator facility cost is raised for beam diagnostics [6]. Advancing sensor technologies, to get detailed information of multiple beam parameters, while having a low maintenance, is necessary to optimise the proton centre workflow and save valuable time, which can be used to treat more patients and ultimately save more lives.

In this work, a novel silicon-based, stand-alone, non-invasive, online beam monitor for medical accelerators is developed. The technology is based on the LHCb Vertex Locator (VELO), used originally for experiments for the Large Hadron Collider (LHC) at the European Organization for Nuclear Research (CERN). The LHC is a two-ring superconducting hadron accelerator and collider located in Geneva, Switzerland. The circumference of the accelerator ring is 26.7 km with a total energy of 14 TeV. The motivation to transfer this technology was made in 2010 and since then has been conceptualised and further developed in subsequent years, which is outlined in the next section.

1.2 History of the project

In 2010, G. Casse and others from the High-Energy Group at the University of Liverpool proposed the LHCb VELO detector modules as a beam quality monitor for proton therapy beams [7]. They argued, that design specifications of the silicon sensor with low mass, high spatial resolution, speed and radiation hardness are very suitable. The novelty of the method was to measure the proton beam halo only, thus the outer, low intensity tail of the beam, while the core beam spot, used in therapy, will not interfere with the sensor.
This is a fundamental difference to currently used beam monitors in proton therapy, which intercept the beam. The backbone of these monitors are ionisation chambers. They are simple, robust and easy to operate, however they require daily calibration and their response time is slow, despite efforts to optimise material and readout time [8].

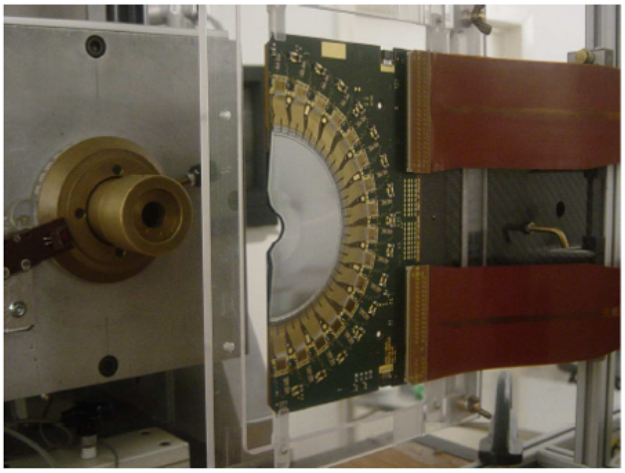

Figure 1.1 – Setup of the test measurement with one LHCb VELO detector module at the proton beamline of the Clatterbridge Cancer Centre.

Therefore, the first preliminary test with one VELO module was carried out at the 60 MeV proton therapy beamline at the Clatterbridge Cancer Centre (CCC), UK, normally used to treat ocular tumours (see Fig. 1.1) [9]. In the experiment, the VELO module was positioned at various distances after the beam exit brass aperture collimating the proton to a diameter of 15 mm. Several beam spots and the corresponding halo were measured and the results were found to be of sufficient

quality (see Fig. 1.2). Thus, the technology was pursued to be transferred to a stand-alone setup for medical accelerators.

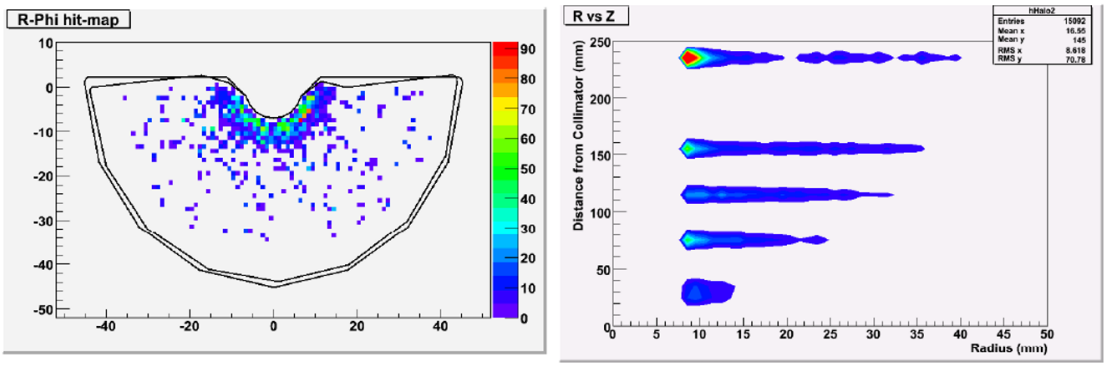

(a) **(b)**

Figure 1.2 – a) Proton beam halo hit map of the LHCb VELO detector module. b) Extent of the proton beam halo for different distances from the aperture.

From 2010 to 2014, Tomasz Cybulski working at the Cockcroft Institute as a member of the QUASAR Group, took over the project to develop a stand-alone system of the LHCb VELO detector modules [10]. The setup and changes are outlined in chapter 4 in detail; however, a brief overview about the achieved developments are summarised in the following. A setup for the safe operation of the detector system outside of the LHC environment was required. The new system would be used in air and without the in-house LHC cooling system. Thus to avoid overheating and to minimize noise, an efficient venting and cooling system had to be designed and implemented. Additionally, to support the LHCb VELO detector modules sufficiently and protect them from getting damaged, a dedicated frame and positioning system was developed.
For the proposed experiment, a Faraday Cup (FC) was designed to correlate the measured output of the VELO detector modules with each other. The work was concluded with a brief test at the Clatterbridge Cancer Centre.

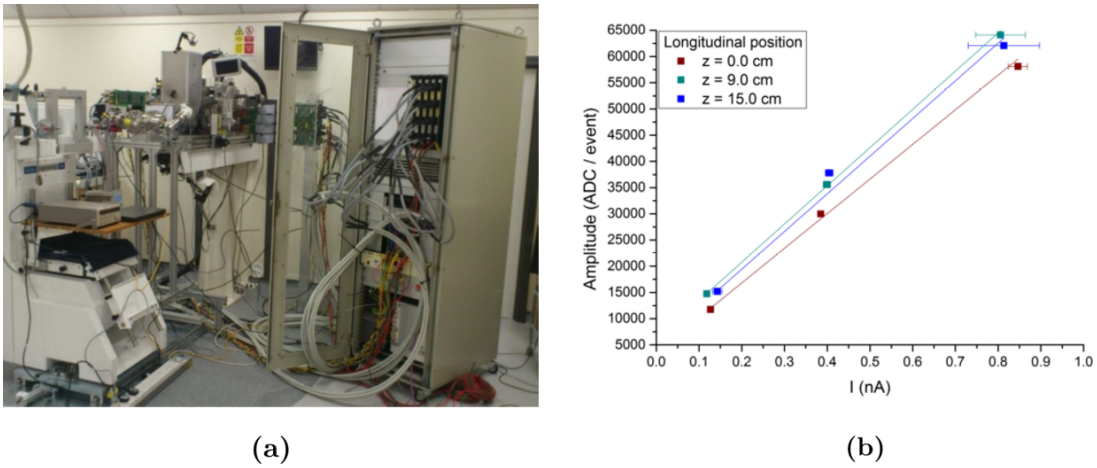

(a) **(b)**

Figure 1.3 – a) Setup of the stand-alone LHCb VELO detector modules at CCC. The detector modules are in the integration zone between the green repeater boards. The Faraday Cup is positioned at the beam exit.
b) Measured results for three different positions of the modules in the integration zone. It shows the average increase of the integrated ADC values in the PHI-sensor per readout event versus the proton beam intensity measured by the FC.

While the results indicated the viability of the detector for an estimation of the beam current, the experiment had various shortcomings listed below, which will be specifically addressed in this thesis.

1. The VELO detector modules are collecting events at the LHCb experiment at CERN at a frequency of 40 MHz, corresponding to the bunch crossing frequency. The proton bunches in medical accelerators are arriving with different frequencies, thus for an optimal readout, the parameters should be adjusted. This was not implemented, resulting in proton bunches being randomly sampled by the VELO detector modules, which can result in a negative signal in the worst case.

2. The readout of the VELO detector modules and the Faraday Cup were not synchronised. The data collection flow is outlined in [10], chapter 6.1, Fig. 67. The data acquisition systems of VELO and the FC were operated independently. The simultaneous start and stop was only predicted. An internal trigger delay before starting the data acquisition in the VELO readout electronics was estimated by 19 s, but was found to vary by a few seconds. In [10], it was reported that the accuracy of the integrated average amplitude

per sensor per readout event, corresponding to a specific average beam current value, was subject to uncertainties reaching as high as 15% (see Fig. 1.3). Because of the missing timing readout, the total collected output values of the VELO detector modules were not expressed, instead the average amplitude per collection event was correlated to the readout of the Faraday Cup. Also, in the experiment, only three different beam current settings were used to indicate a linear response of the VELO detector modules with the Faraday Cup.

3. The analysis of the measured data by the VELO detector modules was carried out completely offline, thus an insight of the value of the measured parameters was not available during the experiments. These affected the result, if beam current fluctuations during the data acquisition occurred. This is unacceptable for a beam monitor used in a medical environment.

In conclusion, the work was successful in building a stand-alone setup that was able to be operated in a medical environment. The described flaws resulted in an insufficient quality of results during the measurement campaign. The further development of the system was picked up two years after the last measurement and is the scope of this thesis. Further optimisation of the stand-alone setup was conducted; in particular, the three major points are addressed in detail. The objectives and structure of the work is outlined in the following section.

1.3 Thesis outline and objectives

This work will explore the feasibility of using the LHCb VELO detector modules as a beam monitor for proton radiation therapy. In order to give a qualified answer, the following objectives need to be addressed within this thesis.

1. Review of the current state of medical accelerators to identify crucial characteristics for a beam monitor.
2. Review of detector technologies commonly used for medical accelerators and to show their limitations.
3. Description of the LHCb VELO detector modules stand-alone setup and the addressing of the shortcomings described in the previous section by newly developed hardware and software modifications.
4. Characterisation of the LHCb VELO detector modules in a proton beamline as a beam monitor.
5. Derivation of the Halo to Dose relationship based on the measurements results, necessary for a clinical implementation.
6. Discussion of the results, showing potential advantages over current detector technologies and review of possible application areas.

The objectives are all addressed in the chapters of this thesis. A brief overview of each chapter is given below.

In the second chapter of the thesis the state of the art of proton radiotherapy is described. The basic physics and interactions of uncharged and charged ionising radiation with matter are characterised. In particular, the important relationships of the stopping power, the dose and the dose distribution of protons will be derived and correlated. In the second part of the chapter, a general cyclotron based proton therapy centre is outlined. The layout of proton radiation facilities shows the application areas of beam monitors and what characteristics have to be observed to successfully operate medical accelerators. The last section will describe the technical details of the proton beam test facility, the MC40 cyclotron proton beamline

at the University of Birmingham, where the LHCb VELO detector modules are thoroughly tested.

The third chapter describes current technologies for beam monitoring in medical accelerators. A brief overview of existing types of detectors is given and in which part of the accelerator they are located. As ionisation chambers are the current back bone of beam monitoring in medical accelerators, details of operating principles and current examples in several treatment facilities are reviewed. Also, advantages and disadvantages are listed to conceptualise what future detectors need to achieve to optimise or replace ionisation chambers. Further, radiographic film is described, as it was utilised as a detector during the tests in the proton beam. The VELO detector modules are based on silicon semiconductor technology; therefore, the physical principles of silicon semiconductors are described. Current technologies are reviewed and evaluated.

The fourth chapter reviews the technology of the detector, which was used at the LHCb experiments and the work undertaken to transfer the technology to a standalone system for medical accelerators. Moreover, the advances completed during this work are detailed. These focus on the firmware updates of the readout system introducing a convenient way to synchronise the proton bunch arrival with the readout of the VELO detector modules. The restructuring and extending of the data acquisition scripts allows a perfectly timed readout of the detector modules and a second instrument, which is an ionisation chamber in this case. The data processing and analysing has been completely revised to introduce various new features and allows a quasi-online readout. Finally, the complete system, ready for implementation, is summarised.

The fifth chapter covers the implementation and measurement campaign using the MC40 cyclotron at the University of Birmingham. The setup process is described and the measurement goals are stated. The ultimate goal is to correlate the measured parameters by the VELO detector modules for different beam currents and beam sizes to the dose. Therefore, considerations about the different effects of the proton beam are made by calculating the expected measured signal and using GEANT4 simulations of the MC40 cyclotron beamline model. Results are presented to verify the implemented changes to achieve a synchronised readout, to show the response of the VELO detector modules to different settings of beam

current from 0.2 nA to 6 nA and the differences of beam sizes by using collimators from 7 mm to 20 mm in diameter. The results are compared where possible to the GEANT4 simulations and film measurements.

The sixth chapter is summarising the results to derive a Halo to Dose relationship. Based on the found relationship, the dose for one measurement run is calculated and compared to the dose levels at the LHC. The outcome of the measurements will be discussed in chapter seven and the VELO detector modules are assessed as a proton beam monitor. The impact of the VELO detector modules for current and future beamlines is outlined. Finally in chapter eight, the work is concluded and an outlook for the VELO detector modules and beam monitoring systems for medical accelerators is given.

2 State of the art of radiotherapy

Depending on the research area and profession, radiotherapy is a broad topic with different aspects. Fundamentally, three points of view are important to consider: the aspects of physics and technology, of radiobiology and of the clinic. Radiobiology investigates the cell response of tumours and the normal tissue environment to radiation. Particularly, the direct and indirect damage of DNA strands with different radiation types are explored. This is important in understanding the cancer mechanics and for planning treatments and dose fractionation during treatment sessions.
The clinical side will look into the outcome of treatments with radiotherapy. In clinical trials, patients with identical cancer diagnosis will be grouped and treated with different methods, e.g. comparing surgery and chemotherapy with radiotherapy or using different types of radiation. These studies are important to refine and optimise cancer treatment, but also support the clinical evidence for using the more expensive particle therapy.
Within the scope of this thesis, the physics and technology aspect is described.

Thus in this chapter, the basic physics of radiation types and components of a modern medical particle therapy centre are presented. The interactions between particles and matter are described and the equation of the stopping power, characterising the energy loss of the particles in matter, is defined. The relationship is used to describe the dose and its distribution in water. The section will be concluded by describing the proton beam halo. After that, a cyclotron based particle therapy centre from its source to the patient treatment room is outlined. Moreover, technical details about the test facility, the MC40 proton beamline at the University of Birmingham, are given, which is used to characterise the VELO detector modules.

2.1 Physics of radiotherapy

2.1.1 Interaction of ionising radiation in matter

Ionising radiation is distinguished between indirectly ionising radiation and directly ionising radiation. Indirectly ionising radiation uses high energetic X-rays or photons in conventional radiotherapy. Direct ionising radiation is characterised by electrically charged particles like electrons, protons or heavy ions like oxygen and carbon. The topic of this work is based on proton radiation therapy, so photon-matter interaction will be discussed briefly only based on [11].

Photon-matter interaction

When indirectly ionising radiation interacts with matter, the energy of the photon can be converted to kinetic energy of secondary particles or radiation. The attenuation of the incident photon beam is described by the absorption coefficient μ resulting from the fluence Φ and the thickness x:

$$\Phi(x) = \Phi_0 \times e^{-\mu \cdot x} \qquad [\Phi] = m^{-2} \tag{2.1}$$

The energy transfer of photons can be summarised by three major interactions and are shown in Fig. 2.1:

1. Photo-electric effect: The incident photons transfer their entire energy to an atomic bound electron. The kinetic energy of the electron is high enough to leave the electron shell and is able to interact with neighbouring atoms directly. The effect is dominating from energies at 10 keV to 100 keV and is rather insignificant for radiotherapy.

2. Compton effect: The photon is scattering inelastic off the atomic bound electron and only a part of the incident energy is transferred. The electron can be absorbed in the matter and emit Bremsstrahlung. The scattered photon can further interact with matter and is important to consider for the energy range from 6 MeV to 25 MeV used in radiotherapy.

3. Pair production: If the energy of the photon is higher than 1.022 MeV, it is able to produce an electron-positron pair in the electromagnetic field of the atomic nucleus. The positron will annihilate with an electron within a few mm and gamma radiation is emitted. Pair production is dominant for energies higher than 20 MeV.

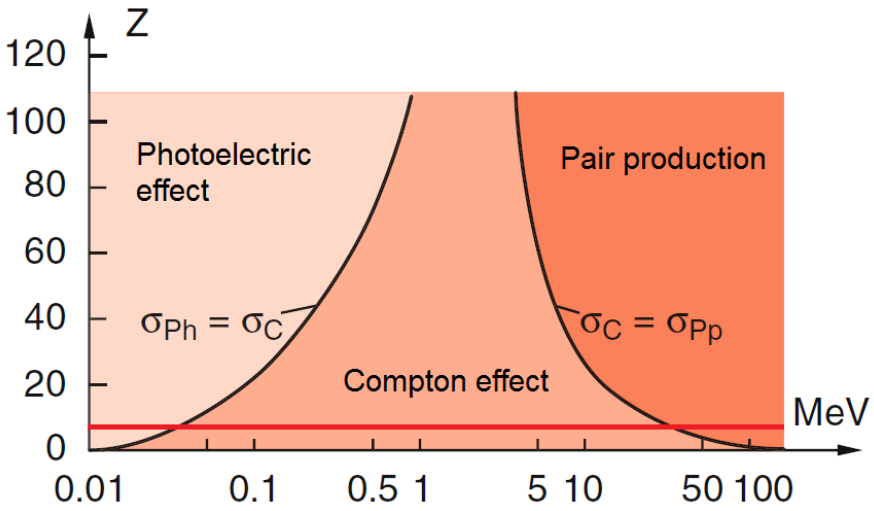

Figure 2.1 – Dominating photon-matter interactions according to the atomic number Z and photon energy. For organic tissue Z=7 (red line), the Compton effect is the most common interaction with photons for the therapeutic energy range from 6 MeV to 25 MeV. (Modified after [12].)

According to Eq. 2.1, the photon beam will remain a fraction of photons with the initial fluence Φ_0 or consist of scattered photons that will leave the matter at different angles respectively to their incidence. Therefore, the range of the photon beam cannot be defined and has direct consequences on the dose distribution in a patient.

Proton-matter interaction

Interaction between charged particles and matter is dominated by Coulomb's law, thus they transfer the energy directly. The force F is dependent on the squared

distance r between the charges, the atomic number Z of the matter and the atomic number of the scattering particle z.

$$F = \frac{1}{4\pi\epsilon}\frac{Zze^2}{r^2}, \tag{2.2}$$

where e is the elementary charge and ϵ is the dielectric constant. Induced energy losses by charged particles are characterised by the energy loss per unit length dE/dx and the density of the matter ρ. The mass stopping power S was derived by Bethe and Bloch around 1930 [13]:

$$\frac{S}{\rho} = -\frac{dE}{\rho dx} \qquad \left[\frac{S}{\rho}\right] = \frac{MeV}{g/cm^2} \tag{2.3}$$

Passing through matter, direct ionising radiation will be attenuated through three major processes. These can be classified as stopping from continuous collisions with atomic electrons, scattering due to deflections off atomic nuclei or interactions with nuclei from head-on collisions (see Fig. 2.2). The effects are described in more detail in the following based on [14, 15].

Protons passing through matter scatter via nonelastic collisions with bound electrons due to Coulomb interactions in the medium and lose energy with every scattering event. This continuous slowing down (CSD) process due to the *electronic stopping power* S_{el} results in ionised atoms. Since the proton rest mass is 1836 times higher than the electron rest mass, the proton path is rather unaffected and high energy protons scatter millions of times with bound electrons until they stop at the well-defined depth given by the beam energy. The energy loss of a scattering event is about 20 eV. The scattering event can produce loose electrons that are able to ionise further atoms emitting delta-electrons, which are immediately absorbed in the medium because of their low kinetic energy.

Further, protons interact with the Coulomb field of the nuclei of the atom. The *nuclear stopping power* S_{nuc} describes elastic scattering events, also known as multiple Coulomb scattering (MCS), where the kinetic energy loss of the protons is transformed into the repulsion energy of the nucleus. The repulsive potential energy of the atom can cause a change of direction of the proton. Most of the protons are scattered with small angles ($<16°$) resulting in an angular and radial deviation. The nuclear stopping power increases with High-Z-materials.

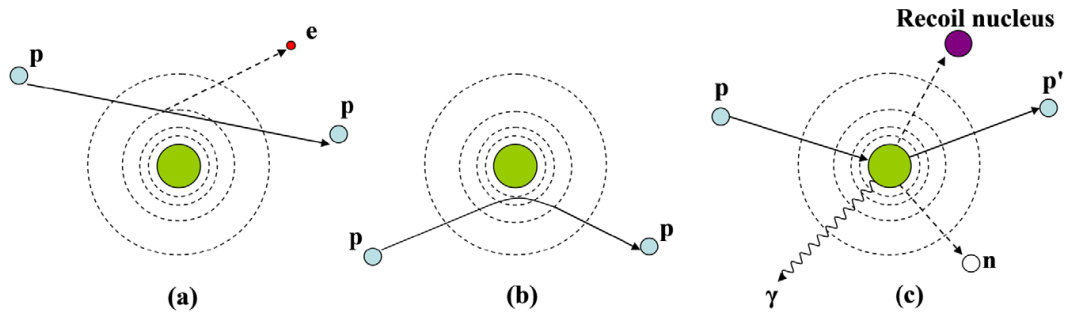

Figure 2.2 – Proton-matter interactions: a) Continuous slowing down (CSD) process via inelastic Coulomb interaction, b) Multiple Coulomb scattering (MSC) via elastic scattering with nucleus c) Inelastic nuclear interaction. [14]

Furthermore, accelerated charged particles can emit electromagnetic waves, called Bremsstrahlung. This *radiation stopping power* depends on the reciprocal squared mass $S_{rad} \sim 1/m^2$, thus, it is negligible for protons.
In addition to these interactions, an inelastic collision of a proton with a nucleus of an atom can result in a loss of the proton from the beam and in the excitation of the nucleus that leads to a release of secondary radiation (single subatomic particles or gamma radiation). These interactions are called *nuclear interactions*. The particles transfer their energy to the absorbing medium as well as the strongly scattered protons. This causes an energy spread of the beam, which decreases the particles' travel distance. Inelastic collisions with nuclei cause a severe energy loss and large deflections of the protons.

The mass stopping power was derived by Bethe [13] in 1930 and Bloch [16] in 1933 and is given by:

$$\frac{S}{\rho} = -\frac{1}{\rho}\frac{dE}{dx} = 4\pi N_A r_e^2 m_e c^2 \frac{Z}{A}\frac{z^2}{\beta^2}\left[ln\left(\frac{m_e c^2 \gamma^2 \beta^2}{I}\right) - \beta^2 - \frac{\delta}{2} - \frac{C}{Z}\right], \tag{2.4}$$

where N_A is Avogadro's number, r_e is the classical electron radius, m_e is the mass of an electron, z is the charge of the projectile, Z is the atomic number of the absorbing material, A is the atomic weight of the absorbing material, c is speed of light, β is the kinematic term $\frac{v}{c}$ with v as the projectile velocity and γ is the Lorentz factor $(1-\beta^2)^{-1/2}$. I is the mean excitation energy of the target material, which has to be determined empirically. δ is the density correction arising from

the shielding of remote electrons by close electrons and will result in a reduction of energy loss at higher energies and C is the shell correction, which is important only for low energies where the particle velocity is near the velocity of the atomic electrons [14].

Considering the case of protons, Eq. 2.4 is written as [15]:

$$\frac{S_p}{\rho} = 0.3072 \frac{Z}{A} \frac{1}{\beta^2} \left(ln \frac{W_m}{I} - \beta^2 \right), \tag{2.5}$$

where $W_m = \frac{2m_{ec}^2 \beta^2}{1-\beta^2}$ characterises the largest possible proton energy loss in a single collision with a free electron (see Fig. 2.3).

Equation 2.5 is used to derive the distinct distance of the travelled proton between the entrance of the material with its initial energy E_{in} and to the point the energy reaches very low values E_{fin}. Therefore, the total path length is calculated as the reciprocal integral of the mass stopping power:

$$R(E_{in}) = \int_{E_{in}}^{E_{fin}} \left(\frac{dE}{\rho dx} \right)^{-1} dE \quad [R] = cm \tag{2.6}$$

The multiple scattering of the protons results in a non-straight path and each path is different for each proton. The mean projected range is smaller than the total path length. This results in the approximation given by the Bragg-Kleeman rule [17]:

$$R(E_0) = \alpha E_0^p, \tag{2.7}$$

where $\alpha = \left[\frac{cm}{MeV^{-p}} \right]$ is a proportionality factor ($\sim \sqrt{A/\rho}$) and p the exponent of the range-energy relation.
For proton energies from 10 MeV up to 200 MeV, the best fit for protons in water is [18] (see Fig. 2.3):

$$R(E_0) = 0.0022 \cdot E_0^{1.77} \tag{2.8}$$

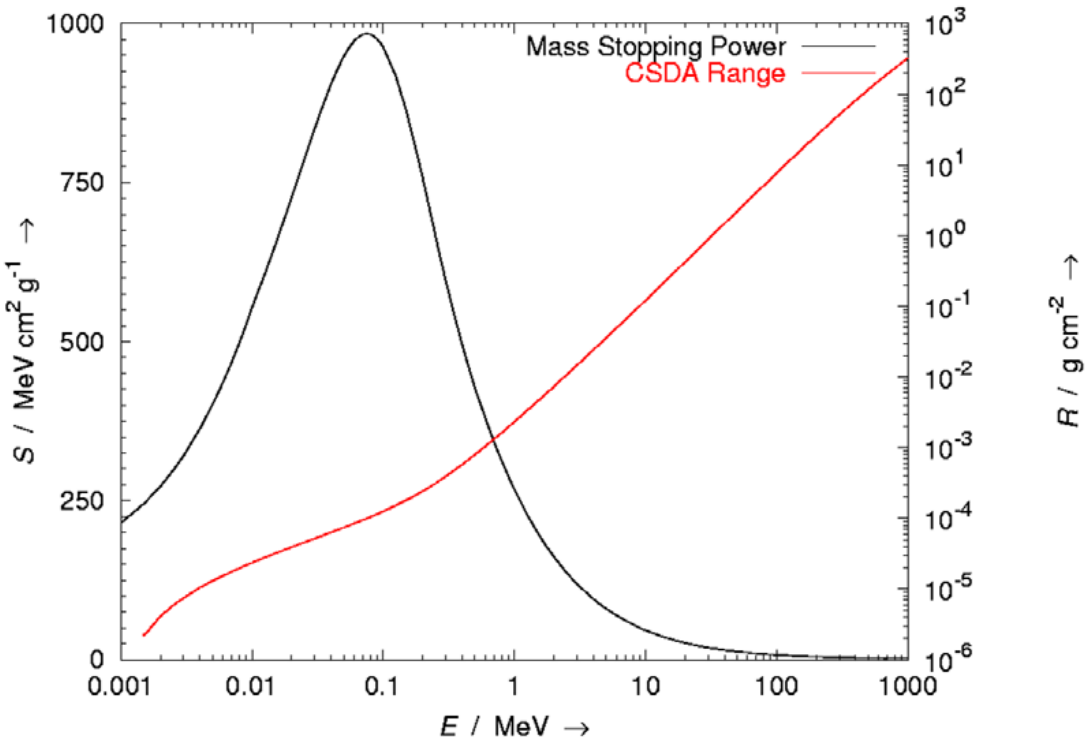

Figure 2.3 – Proton mass stopping power S in water (black line) plotted against the energy based on Eq. 2.5. Additionally, the equivalent range (red line, Eq. 2.7), assuming the CSD approach, is plotted. [14]

2.1.2 Dose distribution of the Bragg-curve

The absorbed energy in matter per unit mass in a medium is defined as the physical absorbed dose.

$$D = \frac{dE_{abs}}{dm_{med}} \qquad [D] = Gy = \frac{J}{kg} \tag{2.9}$$

The SI unit is Joules per kilogram, known as Gray.

Assuming dN protons passing through an infinitesimal cylinder of the area dA and thickness dx, the correlation of the physical absorbed dose and mass stopping power S is given by:

$$D = \Phi \frac{S}{\rho}, \tag{2.10}$$

where Φ is the proton fluence $\Phi = \frac{\#protons}{A} = \frac{Gp}{cm^2}$.

The derivation of Eq. 2.11 is the dose rate as a function of the proton beam current i_p with i_p/A in nA/cm^2:

$$\dot{D} = \frac{i_p}{A}\frac{S}{\rho} \qquad \left[\dot{D}\right] = \frac{Gy}{s} \tag{2.11}$$

With Eq. 2.5 simplified with Eq. 2.7, the dose distribution $D_\mathrm{BP}(d)$ of a monoenergetic proton beam in water, called Bragg curve, is expressed [19]:

$$D_{BP}(d) = \frac{S}{\rho} = -\frac{1}{\rho}\frac{dE}{dd} = \frac{1}{\rho p \alpha^{1/p}(R-d)^{1-1/p}} \tag{2.12}$$

However, energy losses of protons will have a statistical distribution, thus they will not stop at the same depth.
In mathematical terms, the depth-dose distribution of a mono-energetic, narrow (pencil-like) Bragg-curve can be described as the convolution of the stopping power (continuous slowing down approximation) and the range straggling distribution. Range straggling is a result of scattering events and nuclear interactions. Also, the energy distribution of the protons is not homogeneous, the beam energy spread of the protons leads to a decreased range, so the Bragg-peak is broader and rounded. Both effects combined can be approximated by a Gaussian distribution [19, 20]. Considering all effects, the analytical equation to calculate a Bragg curve for proton energies between 10 and 200 MeV is written as follows [19]:

$$D(z) = \Phi_0 \frac{e^{-\zeta^2/4}\ \sigma^{1/p}\ \Gamma(1/p)}{\sqrt{2\pi}\rho p \alpha^{1/p}(1+\beta R_0)} \left[\frac{1}{\sigma} D_{-1/p}(-\zeta) + \left(\frac{\beta}{p} + \gamma\beta + \frac{\varepsilon}{R_0}\right) D_{-1/p-1}(-\zeta)\right], \tag{2.13}$$

where $D(z)$ is the depth dose, z is the depth, ϕ_0 is the primary fluence, R_0 is the range of the proton beam, σ is the standard deviation of the Gaussian distribution of the proton depth, $\zeta = (R_0 - z)/\sigma$, α and p are material-dependent constants (cp. Eq. 2.7), ε is the fraction of low-energy proton fluence to total proton fluence, $\Gamma(x)$ is the gamma function and $D_\mathrm{y}(x)$ is the parabolic cylinder function, which is tabulated [14].

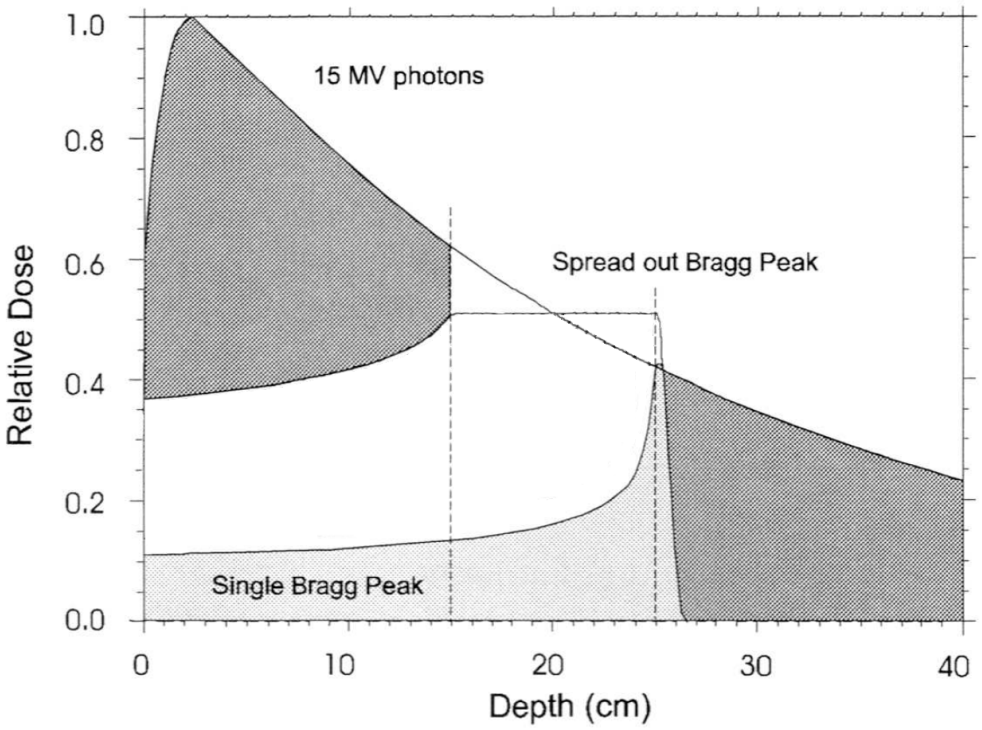

Figure 2.4 – Depth dose distribution in water of a photon beam (E_{ph}= 15 MeV), of a single Bragg-peak and of a spread-out Bragg peak (SOBP) of protons (E_{max}= 200 MeV). The target volume lies between the two dashed lines. The unwanted 'dose bath' of photons (dark grey area) can be spared by using protons. [21]

Comparing percent depth dose profiles of photons or electrons in water or matter with protons (see Fig. 2.4), clear deviating characteristics are obvious. The whole percent depth dose profile of protons is called Bragg-curve and the surface dose which protons create, is two or three times lower than the surface dose of photons. After a dose plateau an abrupt dose rise to the dose maximum called Bragg-peak occurs. This is due to the high stopping power at the end of the proton trace. After a few millimetres past the Bragg-peak the depth dose distribution immediately runs to values near zero. These characteristics show directly the advantages of proton therapy. The main dose is around the Bragg-peak, whereas there is a significant dose input around the target volume in healthy tissue by photon therapy, that can be only partly circumvented with crossed photon beam approaches.

The primary proton beam is a narrow, pencil-like beam. It is monoenergetic and has a defined depth of the Bragg-peak in matter. A tumour as a target volume has a certain extent in all directions, thus a single Bragg-curve cannot achieve a uniform radiation of the target volume. To solve this problem, one superimposes several monoenergetic depth-dose profiles that are varied in their kinetic energies and their lateral axis. The top proton energy correlates with the distal end of the target volume defining also the dose input on each layer. In the following, one delivers less weighted Bragg-peaks with descending energies to achieve a uniform high-dose coverage of the target region. The accumulation of all single Bragg-peaks adds up to the so called spread-out Bragg-peak (SOBP) (see Fig. 2.4). Thus crucial adjustments are: the choice of the energy range to reach the depth and the homogeneous dose of the SOBP. The SOBP depth dose distribution is approximated as follows [19]:

$$D_{SOBP}(r) \approx \frac{D_0}{1 + 0.44 r^{0.6}} \tag{2.14}$$

Methods to generate the SOBP are discussed in section 2.2.2.

2.1.3 Proton beam halo

For the proposed measurements with the VELO detector modules, only the proton beam halo is measured. The beam halo is correlated with the beam width of the proton beam. However, there are different definitions of the beam halo depending on the application area.

In particle accelerators inside the vacuum chamber, the halo around the beam is formed due to the elastic Coulomb scattering of particles with residual gas atoms [22].

In [23], the significance of the beam halo inside water (patient) is emphasised. The pencil proton beam dose distribution in water is divided into the core, halo, and aura. (see Fig. 2.5).

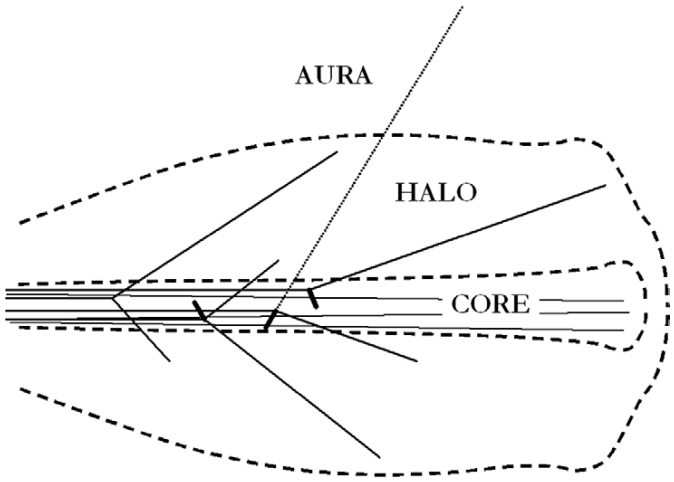

Figure 2.5 – Concept of describing the pencil proton beam dose distribution. Dashed lines are 10% and 0.01% isodoses drawn to scale [23].

The core follows the CSD and MCS processes described above. The aura consists of neutral secondaries, e.g. gamma rays and neutrons, and need to be considered for radiation protection. The halo consists mainly of secondary charged particles. These particles are generated by elastic and inelastic scattering at the nucleus of oxygen and hydrogen. These secondary protons contribute only a few percent to the total fluence, however with a much wider angular distribution, they form a long, low dose tail to the lateral dose profile. In dose calculations to plan the treatment with protons, they are usually ignored, although errors of up to 9-10% can be observed, which can lead to an unaccounted biological damage in tissue [15, 24].

The detector will be neither operated in vacuum nor water, thus in this work, the beam halo is generated by the scattering components inside the proton beamline. The scatterer will spread the pencil proton beam into a Gaussian profile. The material of the scatterer is made of high-Z materials, such as lead or tantalum. This maximises the amount of scattering by reducing the energy range loss. Thus the beam halo will be the low intensity tail of the beam profile.

2.2 Medical accelerators

The first accelerator using ionising radiation for medical purposes was the X-ray tube developed by Wilhelm C. Roentgen in 1895 [25]. Since then, radiotherapy has evolved to be one of the main treatment options for cancer. History shows that the technological concepts and the first treatments with photons and protons were almost performed at the same time. For conventional radiotherapy, electron linear accelerators (LINACs), proposed by Gustav Ising in 1924 [26] and constructed by Rolf Wideroe in 1928 [27], were used for the first treatment at the Hammersmith Hospital, London, UK in 1953 [28]. The technical advances combined with imaging solutions, e.g. computer tomography or magnetic resonance imaging, led to highly developed and compact systems with over 10,000 LINACs worldwide. Only one year later than Wideroe, Ernest Lawrence invented the cyclotron [29]. After Robert Wilson outlined the potential use of protons for radiotherapy in 1946 [4], the first patient was treated in 1954 [30]. The first hospital based proton therapy facility was the Clatterbridge Cancer Centre (CCC), Wirral, UK in 1989 [9]. However technically challenging and costly, over 60 proton therapy facilities are in existence today [15]. With the invention of the synchrotron 1944/45 [31], heavy particles (helium, oxygen, carbon) were utilised to treat patients first at HIMAC (Heavy Ion Medical Accelerator in Chiba), Japan, in 1994 and eleven more facilities were built up to this date [32]. By the end of 2018, over 220,000 patients have been treated with particles [33]. The measurements with the VELO detector modules were performed at a cyclotron based proton beamline. The concept and its application will be explained in the following.

2.2.1 Cyclotrons

In clinical use, protons need to reach depths from 3 cm (ocular tumour) to 32 cm (prostate tumour). According to Eq. 2.7, energies from 60 MeV to 235 MeV are required. To accelerate protons to this energy, commonly cyclotrons are used (see Fig. 2.6).
In the simple case, cyclotrons are ring accelerators consisting of two D-shaped pill boxes (Dees) with a uniform magnetic field. The accelerating field is generated between the Dees by a radio frequency (RF) cavity. Protons are produced in the

source in the centre of the cyclotron using the Penning effect. Two cathodes, kept with a negative voltage of a few kV, emit free electrons spontaneously (cold cathode case). The electrons spiral in the magnetic field, are accelerated and will ionise the injected hydrogen gas. The hydrogen ions and electrons form a plasma. The protons diffuse through a hole or slit by being pulled by the nearest Dee and are further accelerated. The beam current can be adjusted by the gas flow and the arc current between the cathodes and the ground [15].
Protons will circulate on orbits with increasing radius as their energy increases. The radial frequency of the protons has to be equal with the angular frequency of the high voltage. This condition of cyclotron resonance is given by the equation [22]:

$$f = \frac{\omega}{2\pi} = \frac{1}{T} = \frac{1}{2\pi}\frac{ZeB}{m}, \qquad [f] = Hz \tag{2.15}$$

where B is the magnetic field.

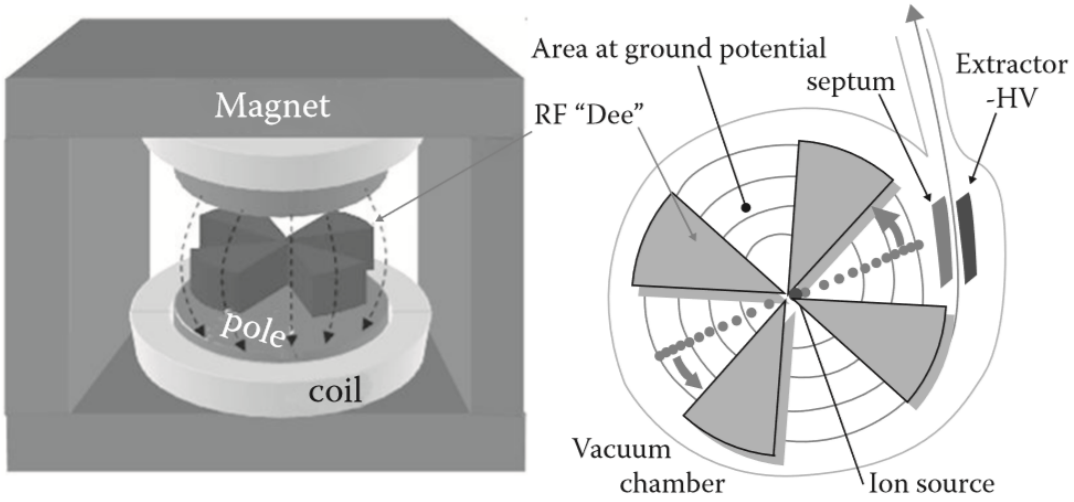

Figure 2.6 – Schematic picture of a cyclotron [15]. Protons are extracted from ionised gas (proton source). An alternating electric field is applied between two or four D-shaped electrodes (Dees) to accelerate the protons.

However, it only applies to non relativistic energies smaller than 20 MeV and therefore protons used for treatment have to be treated as relativistic, since with the

gain of effective mass, the resonance condition is not fulfilled any more. Equation 2.15 is extended by a relativistic term [22]:

$$f = \frac{1}{2\pi}\frac{ZeB}{mc\gamma}h, \tag{2.16}$$

where c is the speed of light, $\gamma = 1/\sqrt{1 - v^2/c^2}$ is the Lorentz factor and h is the harmonic number.

As a result, the cyclotron needs to be modified. This can be done in two different ways by either scaling the magnetic field or the RF frequency.

The **isochronous cyclotron** changes the magnetic field in radial dependence:

$$f \sim \frac{B[r(t)]}{\gamma(t)} \tag{2.17}$$

A common way to realise it, is to decrease the gap between the magnet poles with the increasing radius. An increasing magnetic field defocusses the proton beam vertically, which needs to be compensated by a focussing power. Therefore, the magnet poles are split up in sectors called hills and valleys with the Dees mounted in the valley. Examples of these types are the MC40 cyclotron used at the University of Birmingham and the Scanditronix MC-60 PF cyclotron in the Clatterbridge Cancer Centre.

The **synchro cyclotron** varies the RF frequency with the deviation of the Lorentz factor γ.

$$f \sim \frac{1}{\gamma(t)} \tag{2.18}$$

Used types are the IBA S2C2 cyclotron [34] with a 2.5 m diameter and a magnetic field of 5.7 T and the Mevion S250 cyclotron [35] with a 1.8 m diameter and a magnetic field of 8.7 T.

With the advances of the superconducting technology in the 1980s becoming available for cyclotrons, higher magnetic fields in a more compact design were achieved. This led to the reduction of weight from the first commercially available cyclotron from IBA of 200 t to Mevion's with 22 t.

When protons reach their final energy, they are guided out of the cyclotron through an extraction system. Parallel to the beam, a thin vertical blade called a septum separates the extracted protons from the ones still making turns. Parallel to the septum at a larger radius, a cathode applies tens of kV to lead the protons in the extraction channel between coils and through the yoke [15].

The maximum energy of cyclotrons is usually fixed, thus an energy selection system is needed.

2.2.2 Modulation of the energy

The modulation of the energy is crucial to get a homogeneous dose plateau of the SOBP. In order to shift the range of the proton beam, the energy of the protons needs to be reduced. This is achieved by inserting a variable amount of low-Z-material, the degrader, after the accelerator. Examples for degraders are either a spinning carbon wheel with different thickness or several carbon wedges, which are inserted quickly in the beamline for depth variation. The loss of energy of the proton is accompanied by scattering (MCS), which increases the beam size, energy spread or emittance and creates neutrons, which is relevant for shielding considerations. Following the degrader, collimators and a magnet bending system, the energy selection system (ESS) is selecting the protons with right energy into the beam transfer line. Within the transfer line, bending and focussing magnets and beam diagnostics must be corrected for the used beam energy to maintain the quality of the proton beam. The range modulation should last <0.5 s to switch from one energy to another. If passive scattering is used, range modulators are inside the nozzle as rotating disks (see Fig. 2.7) [15].

2.2.3 Delivery modes of proton beams

A tumour as a target volume has a certain extent in all directions, thus a narrow proton beam is not directly applicable to a radiation therapy. To solve this problem, the primary proton beam has to be varied in its energy as discussed previously and its lateral axes. Lateral broadening of the beam is achieved by passive beam shaping or by scanning systems.

Passive beam shaping

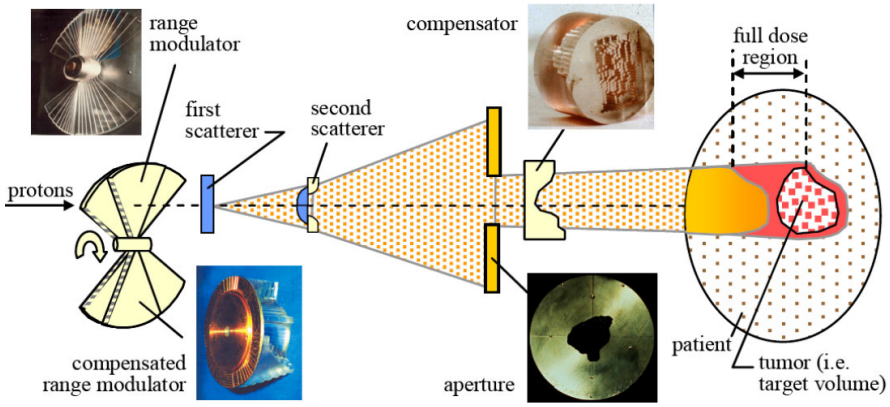

Figure 2.7 – Setup of a double-scattering system used at the MGH Francis H. Burr Proton Beam Therapy Center [36].

The main idea of the passive beam shaping is to spread the proton beam to a uniform area in a lateral direction by putting scattering material in the beam line (see Fig 2.7). In a clinical environment, the shaping is done in two steps (double-scattering system). The first scatterer, a homogeneous thick high-Z-material (lead, tantalum), spreads the beam to a lateral Gaussian distribution. The second scatterer flattens out the primary distribution. The bi-material device combines a high-Z scattering material in the centre with a low-Z compensation material (plastic, carbon, aluminium) on the outside. So protons hitting the centre lose more energy than those going through the periphery parts to create a uniform, flat lateral beam along the beam width. In the CCC (see Fig. 2.8), the two scattering foils are made of 25 µm thick tungsten [9]. A range shifter and modulation wheel generate the SOBP. A field-specific aperture, made of brass and a compensator, made of plastic, are used to conform the beam laterally and to the distal end of the target. The compensator and the aperture are mounted on a retractable snout [36].

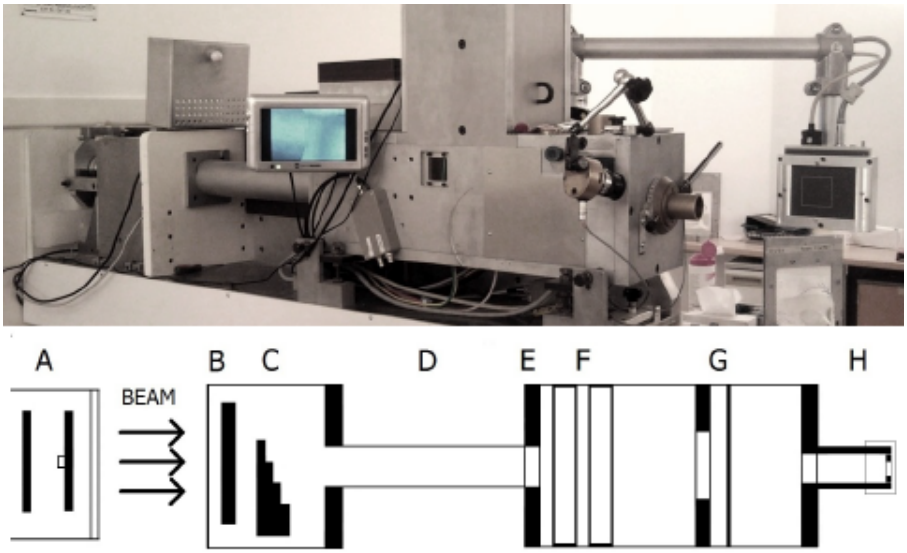

Figure 2.8 – Double scattering and beam modulation system of the CCC. Beam is passing through the two scattering foils (A) and is shaped by the range shifter and modulation wheel (B, C). Beam monitoring ICs (F) and cross wires (G) to measure dose and profile. Nozzle and aperture (H) for final beam shaping. [37]

Scanning systems

In contrast to passive beam shaping, in scanning systems the narrow beam will not be widened to the maximum field size, but only be minimal scattered to a spot with a diameter up to 20 mm at the end of the particle trace. The spot/beam size is affected by any material in the beam path. Apertures or beam-focusing magnets can tune the beam size.

Particle beam scanning (PBS) (or pencil beam scanning) uses a beam deflection tube with two fast magnets (sweeper magnets) for the x- and y-axis deflection of the proton beam over the target area in a zigzag spot pattern (see Fig. 2.9). The amplitudes of the intensity in vertical or lateral directions are adapted to the shape of the tumour regarding the depth. The depth change is done by energy modulation (see section 2.2.2). The maximum beam range is given by the maximum energy. To ensure a uniform target dose and to reduce uncertainties, each layer (2D irradiation at a single energy, up to 20-30 times) is intensity modulated and may be delivered

more than once. As opposed to the double-scattering systems, a uniform SOBP is not always required and non uniform depth dose distributions are applied.

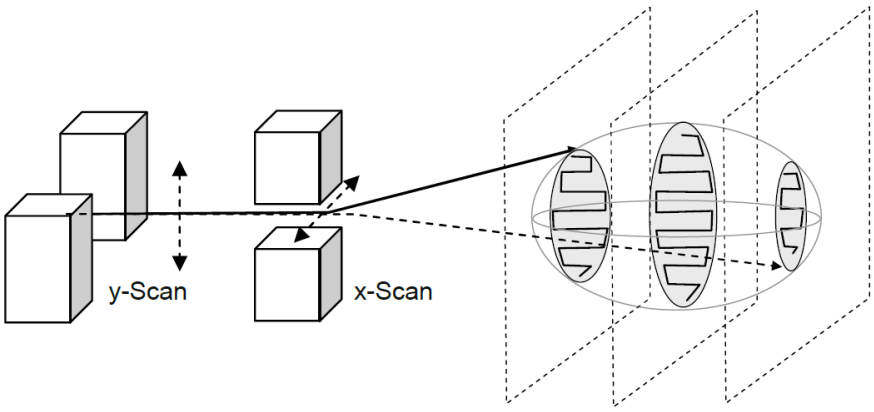

Figure 2.9 – Deflection of the pencil beam via sweeper magnets in x- and y-direction of a scanning system. The layers (grey) are adapted to the three dimensional tumour volume (light grey lines). [38]

A simple delivery method of the scanned beam is the step and shoot technique. The beam current is switched off after the dose is delivered at a static spot. Once turned on again, magnets deflect the beam to the next spot. Another used scanning method is the continuous spot scanning technique. In this case the proton beam is scanned fully continuously across the target volume. In order to deliver the right dose at each point in three-dimensional space (voxel) within one energy layer, the intensity of the proton delivery has to be varied as needed during the scan. The intensity modulation is achieved by changing the dose rate, so the output of the beam source is modulated. The time the beam spends at any given voxel can also be modulated, so the intensity modulation is dependent upon the beam speed determined by the power supply system and the sweeper magnets. Both intensity modulation methods can be combined, however this requires higher demands on the control circuitry. Using the continuous spot scanning significantly reduces the required time covering all layers compared to the step and shoot technique. [15]

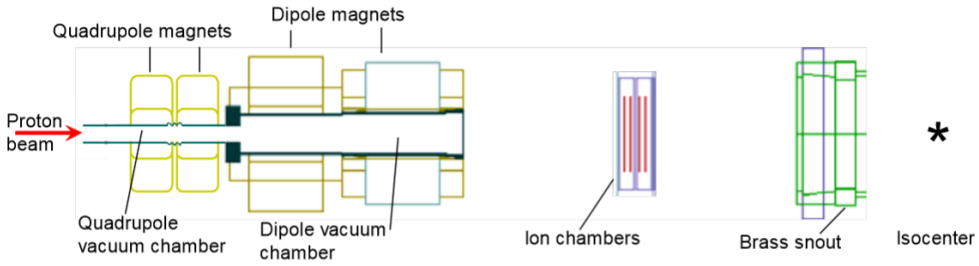

Figure 2.10 – Schematic sketch of the nozzle used for pencil beam scanning at MGH. Quadrupole magnets control the beam size, a pair of scanning dipoles deflect the beam to the desired position and ion-chambers measure the dose, position and beam profiles. [15]

One advantage of using scanning systems is the optional use of apertures or compensators to determine the three dimensional field shape (see Figs. 2.10 and 2.11). Thus, a smaller width and a sharper distal fall-off of the Bragg-peak can be achieved. Moreover, the reduction of damage to healthy tissue and less production of particles due to less nuclear interactions is observed. In terms of the clinical routine, reduced treatment times and simpler treatment planning techniques are possible [39].

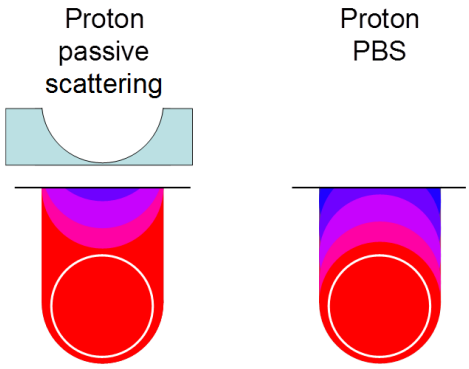

Figure 2.11 – Schematic dose distribution for a target volume (white circle) for a single field delivered by a passive scattering and scanning system. More sparing of the healthy tissue of high dose levels can be achieved by scanning systems. [40]

However, the most important advantage is the ability to deliver intensity-modulated proton therapy (IMPT). The IMPT allows the three dimensional localisation of

dose with varying proton fluence [41]. For pencil beam scanning and IMPT, more sensitivity to organ motion and dose calculations in comparison to passive scattering is observed [42, 43]. Therefore, range verification methods for proton beam therapy are highly desirable and needed [44].

2.3 Treatment room

Before the proton beam is exiting to the patient, important beam instrumentation and beam shaping devices are inside the treatment head or nozzle. They monitor the beam position, symmetry, beam size and also measure the integrated charge, which is proportional to the number of protons (see Fig. 2.10).
To perfectly include the shape of the tumour, it is necessary to irradiate the immobilised patient on the patient couch from different directions of the treatment head. This is achieved by a *gantry system*. Gantries are large and weigh up to 200 t [45], since the magnets need to bend the beam with therapeutic energies with large radii and also because of the size of the nozzle (length: $\sim$2.5 m). However, the mechanics of the gantry have to ensure a precise dose delivery within 1 mm under all rotation angles. Similar to the development of cyclotrons, superconducting gantries for proton therapy offer the possibility to reduce the weight by a factor five to ten to about 25 t [45]. The first superconducting gantry for carbon therapy was used for treatment at the National Institute of Radiological Sciences in 2017 and weighs 300 t [46].

2.4 The MC40 proton beamline at the University of Birmingham

In recent years, the Clatterbridge Cancer Centre showed a steep incline in patient numbers. Due to the restricted access and the large logistic efforts needed to move the VELO setup, an alternative testing facility needed to be found. Therefore, the MC40 proton beamline at the University of Birmingham was selected. The history of accelerators at the University of Birmingham dates back to 1948, when the first 60" Nuffield cyclotron was installed. It was able to accelerate protons to 10 MeV and alpha particles to 40 MeV. The currently used MC40 cyclotron is the third one and was installed from 2002 to 2004, after being transferred from Minneapolis. The radius is 53 cm and a maximum magnetic field of 1.8 T is used. It is commonly used to accelerate the following particle types: protons (E_{max}=39 MeV), deuterons (E_{max}=19.5 MeV), alpha particles (E_{max}=39 MeV), $^{3}He^{2+}$ (E_{max}=54 MeV) and nitrogen $^{14}N^{4+}$ (E_{max}=46 MeV), $^{14}N^{5+}$ (E_{max}=70 MeV). The cyclotron is mainly used for isotope production, such as ^{81}Rb for ^{81m}Kr generators, and radiation effect studies for detectors in accelerators and space electronics. Further, radiobiology, dosimetry and nuclear physics experiments are conducted [47]. The studies and experiments are conducted in two experimental rooms (see Fig. 2.12).

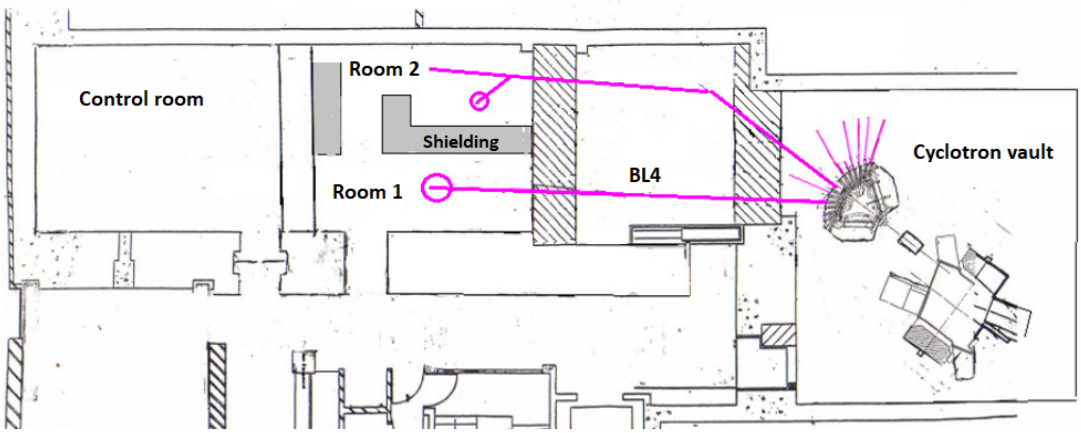

Figure 2.12 – Layout of the irradiation facility of the University of Birmingham, featuring the cyclotron vault, the high intensity irradiation area, and the operator control room. Two experimental rooms are dedicated for studies. These include studies for detectors used at ATLAS (room 2) or for Medical and Nuclear physics experiments (room 1). [47]

The beam and timing characteristics of the cyclotron for protons are summarised in Tab. 2.1. The parameters and layout of the beamline were obtained through private communication with the technical manager Ben Phoenix and the Lecturer in Medical Applications of Accelerators Dr. Tony Price, University of Birmingham. The beamline follows the pink lines in Fig. 2.12.

Table 2.1 – Cyclotron time structure and beam parameters.

Parameter	Value
Ion type	p+
RF frequency	14.2-28 MHz
RF period	70.92-35.71 ns
Ion kinetic	11-39 MeV (N=1)
energy	3-9.5 MeV (N=2)
Energy spread	0.5%
Beam current	(1) pa - 60 μA
Number of ions/s	$6.24 \cdot 10^6$ - $3.75 \cdot 10^{14}$

After extraction of the cyclotron, the beam intensity can be measured with a Faraday cup (FC1). The beam then passes through a 12-way splitting dipole magnet to select the beamline. Studies for Medical and Nuclear physics applications are conducted on beam line 4 (BL4). The beam is deflected into the magnet room, where the second Faraday cup is held (FC2). Approximately 6 m from the final collimator is a set of quadrupoles magnets (Q1), which focus the beam. Two meters from the quadrupoles magnets (4 m before the final collimator), the beam passes through a brass collimator with an aperture diameter of 5 mm and is incident upon an 80 μm tantalum foil. The foil causes low angle scattering and enlarges the beam to a Gaussian shape. The following collimator consists of an aluminium collimator of 50 mm in diameter onto which an ionisation chamber is mounted to monitor the beam current on an electrometer. The exit collimator consists of another 50 mm diameter aperture, over which it is possible to slot the desired final collimator. The experimental equipment is usually setup approximately 20 cm behind the final collimator on a height adjustable table (see Fig. 2.13).

Figure 2.13 – Dedicated experimental room with height adjustable table behind the final collimator for studies with the LHCb VELO detector modules.

2.5 Summary

Particle radiation therapy uses the unique characteristic of the Bragg-curve. The sharp peak is able to target tumours precisely to spare healthy tissue. Based on the proton-matter interactions of the continuous slowing down process via inelastic Coulomb interaction, multiple Coulomb scattering via elastic scattering with the nucleus and inelastic nuclear interactions, the mass stopping power can be derived. This fundamental unit relates directly to the finite range of protons and the absorbed dose. The proton beam halo, which will be detected by the VELO detector modules, is the low intensity tail of the Gaussian beam profile, which is the result of scattering components inside the beamline. Medical accelerator consists of an accelerator, e.g. the cyclotron, the beam transfer line and the treatment head. Protons produced by cyclotrons have a fixed energy and need to be modulated in energy. Two delivery modes for proton beams are used. The passive beam shaping, usually used for ocular tumour treatment, e.g. in the 60 MeV proton facility at the CCC, consists of two scattering components to shape the beam. Apertures and compensators are made patient specific for the coverage of the tumour volume. Modern facilities use pencil beam scanning systems with two sweeper magnets to cover the tumour volume faster and more precisely. The irradiation tests of the VELO detector modules were performed using the MC40 proton beamline at the University of Birmingham. This cyclotron based research facility allows energy modulation of protons from 3-39 MeV and beam currents from pA to μA for varying beam sizes. Therefore, it is a perfect testing environment for the detector studies.

3 Beam monitoring for medical accelerators

Beam diagnostics are the 'eyes and ears' of the operator to control a modern accelerator system and guarantee the Quality Assurance (QA). Online beam monitoring is essential for ion beam therapy to assure effective delivery of the beam and maintain patient safety for cancer treatment.

Beam diagnostics for a medical accelerator are highly diverse and cover an extended area of responsibility in different locations. They have to monitor the accelerator performance throughout operation to prevent radiation damage and monitor the radiation levels for protection of the personnel. In clinical radiotherapy, QA procedures are described in the International Atomic Energy Agency (IAEA) Technical Report Series (TRS) number 398 on absorbed dose determination in external beam radiotherapy [48]. It includes requirements on daily, weekly and annual measurements. The main checks for diagnostics are the calibration and performance control, since they have to verify the absolute dose and dose rate or the control of the planned dose distributions from a treatment planning system before patient treatments. Further, they are used for the development of the accelerator and diagnostics out of the treatment hours. Therefore, the design and purpose of a detector needs to be chosen carefully for its requirements. As an example, in the heavy ion treatment centre at MedAustron, 153 devices in total make up the entire beam diagnostics system [49]. Up to 10% of cost of the entire accelerator facility must be dedicated to diagnostic instrumentation [6], which shows the significance for research and development to optimise monitoring systems further.

In general, the following characteristics are important for any instrument. Its exact specifications are dependent on the requirements of the proton therapy centre. As an example, specifications for the proton beam of the CCC are listed [9].

1. Sensitivity
   The smallest signal that can be resolved. In CCC, proton currents are as low as 1 nA.

2. Accuracy
   How close the measured value is to the real value. If not, correction factors may be applied. Maximum uncertainties have to be limited to 1-2% for the integral flux or current and 0.5 mm for the transversal beam position and 1 mm for the transversal shape [50].

3. Resolution
   The smallest change that can be measured. Beam current measurements are resolved in tens of pA. Time resolution in the current system is in the range of a few kHz.

4. Dynamic Range
   The ratio between the largest and smallest signals that can be measured. The current reaches up to 30 nA. Additionally, devices need to be capable of dealing with the applied current or dose rate as a second important factor. The dose rate is between 1 to 40 Gy/min.

5. Measurement speed
   How long it takes to make a measurement. Is the signal monitored online or does it need offline analysis? Online beam monitoring is necessary in a clinical environment.

6. Reliability
   The diagnostic instrument should be fully available at all times and not give the wrong output. The instrument should be easy to calibrate and be stable throughout the usual 10 h of the daily operation of the accelerator.

Further, it is important to determine, if the instrument is non-invasive, invasive, or destructive to the beam. The instrument should be easy to use and fulfil the size requirements of the dedicated implementation area.

Within the beamline of medical accelerators, four application areas are identified for monitoring, described in section 2.2:
Diagnostic instruments need to measure quantities within the accelerator and

beamline, in the nozzle and at iso-centre at the end of the beamline where the patient will be located. Further, measurements using the patient as an instrument (in-vivo measurements) are performed. The latter will not be included within the scope of this thesis.

In the following, an overview of the most used detectors, the quantities they measure and where they are situated, are summarised in Tab. 3.1 [6, 51].

The next sections will cover the instruments that will be used during the measurements at the MC40 proton beamline. That includes especially ionisation chambers as the current backbone of radiotherapy, the new emerging field of silicon semiconductor detectors for beam monitoring and films.

Table 3.1 – Overview of detectors used in medical accelerators [6, 51].

Detector type	Application area	Physical effect	Measured unit	Invasiveness
Faraday Cup	beamline	charge collection	charge, current	destructive
Current Transformer	beamline	electromagnetic field induction	charge, intensity	non-invasive
Beam Profile Monitor	beamline	electromagnetic field induction	profile	non-invasive
Wire Scanner	beamline	charge collection	size	invasive
Scintillating screens	beamline	luminescence	profile, emittance	invasive
Pepper Pot	beamline	luminescence	emittance	destructive
Pick-ups	beamline	electromagnetic field induction	position, tune	non-invasive
Ionisation-chamber	beamline, nozzle iso-centre	gas ionisation	charge, current, profile	invasive
Film	nozzle, iso-centre	photoelectric effect	intensity, profile	invasive
Calorimeter	iso-centre	heat deposition	absorbed dose	destructive
Silicon diode	iso-centre	bulk ionisation	absorbed dose	invasive

3.1 Ionisation chambers

Ionisation chambers (IC) are current best practice in particle therapy to monitor the beam in the nozzle and to perform QA at iso-centre [15]. They stand out because of the high accuracy and reproducibility, small energy dependence, as well as their robustness and easy operation [51, 52]. The structure of the IC is relatively simple (see Fig. 3.1). Between two parallel conducting metal plates or foils, the anode and the cathode, a gas is contained. The two plates are kept at a high voltage difference up to several kVs. If an ionising particle passes through the chamber, gas molecules are ionised. The resulting ion and free electron will be accelerated in the electric field towards the plates in opposite direction where they are collected. This creates a current that can be measured. The applied voltage has to be high enough that the electric field can remove the generated ions before they can recombine with each other or before the gas is saturated [50].

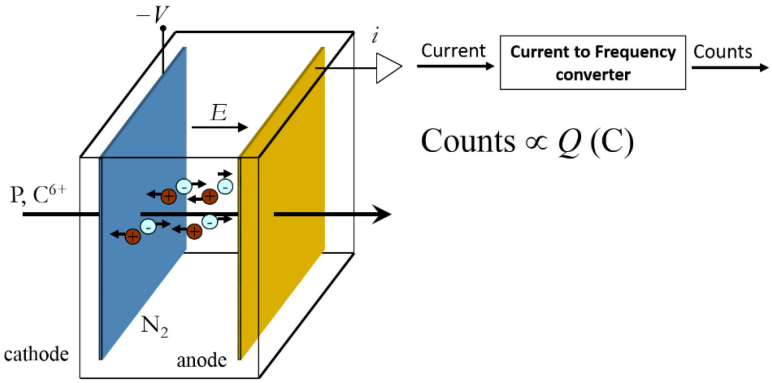

Figure 3.1 – Ion beam passing through the parallel-plate ionisation chamber filled with nitrogen, which creates ion pairs accelerated towards the cathode and anode. [50]

However, a very high voltage has the result that the accelerated ions can ionise the gas itself creating an electron avalanche. This is an unwanted effect, when operating ICs in a particle therapy centre, but is applied in proportional counters. Therefore, ICs operate in a plateau region, where the measured charge for a continuous particle beam is not increasing with the voltage. In this mode, all generated ions contribute to the current [50]. Therefore, the energy deposit of the ionising particle creating the ion pairs is solely proportional with the measured

charge. The average intensity $I = Q/t$ in a monoenergetic beam is given by the flux Φ as the total number of particles N_p per time interval t, the mass electronic stopping power S/ρ for a gas g, the density ρ and the mean free path in the gas x and the mean energy needed to produce an ion pair for a charged particle of an energy E in the gas $W(E)$ [50]:

$$I = \varepsilon \cdot \Phi \cdot \frac{(S_g/\rho) \cdot \rho \cdot x}{W(E)}, \qquad [I] = A \tag{3.1}$$

where ε is the collection efficiency and is an important coefficient, since the biggest source of collection errors in an IC is the recombination of ion pairs before they reach the electrodes. Recombination can appear at the initial point of the ion pair generation, along the path of the ionising particle or within the volume of the chamber. This depends on the angle the beam is passing through and the beam density.
The two most common used gas types are air and nitrogen. Their W-value for electrons (and similar to protons) is $W_\mathrm{air} = 34.2$ eV per ion pair and $W_{\mathrm{N}_2} = 35.4$ eV per ion pair [50].
Ionisation chambers are applied to measure the absorbed dose based on the Bragg-Gray principle, which states that the cavity is small enough to not perturb the charged particle field and the dose is deposited entirely by charged particles crossing [53]:

$$D = W_{gas} \cdot S_g \cdot P, \tag{3.2}$$

where P is the number of ion pairs per unit mass formed in the gas.
Usually multiple correction factors $\mathrm{k_c}$ are applied to account for any differences from the ideal conditions used to derive the mass stopping power. Especially in ionisation chambers filled with air and open to the atmosphere, the output will depend on the ambient air temperature, pressure and relative humidity. Therefore, these chambers need to be calibrated daily to reference conditions [52]. The incomplete knowledge of the corrections is a major disadvantage.

3.1.1 Applications of ionisation chambers in radiotherapy

Ionisation chambers have a wide range of types for different applications. Within the treatment head or nozzle, transmission ICs, parallel plate ICs or strip ICs with

thin entrance and exit windows are used. For QA, small cavity ICs are used for dosimetry [52]. Further, 2D or 3D detector arrays consist of cavity or parallel plate ICs [51]. Requirements for ionisation chambers are to cover the maximum irradiation field size, but still be thin to save material cost and space. Also, the response of the chamber should be uniform at any point of the detector. The correction values for pressure and temperature of the gas need be continuously measured and corrected [50].

Ionisation chambers inside the treatment head

Plane parallel ionisation chambers as transmission chambers are typically used in the nozzle and treatment head. The output of these chambers is expressed in monitor units (MU), which is a normalised dose value to a corresponding reading from a radiation dosimeter [52]. In the proton therapy beamline "Gantry 1" at the Paul-Scherrer-Institute (PSI), up to four different ionisation chambers are used (see Fig. 3.2) [54]. The first three ICs integrate the beam flux and check the applied spot dose in MUs. While the first IC defines the spot dose, IC two and three will compare and check the dose. The beam will be switched off when the expected value has been reached by IC one. The distance between the electrodes, 20 µm thick Mylar foils, is 0.5 cm for monitor one and 1 cm for monitor two with a total window size of 23×3 cm^2. Their readout time is 90 µs ($\sim$ 11 kHz) for monitor one and 350 µs ($\sim$ 2.8 kHz) for monitor two, which is good enough to measure one spot with an average duration of 10 ms.

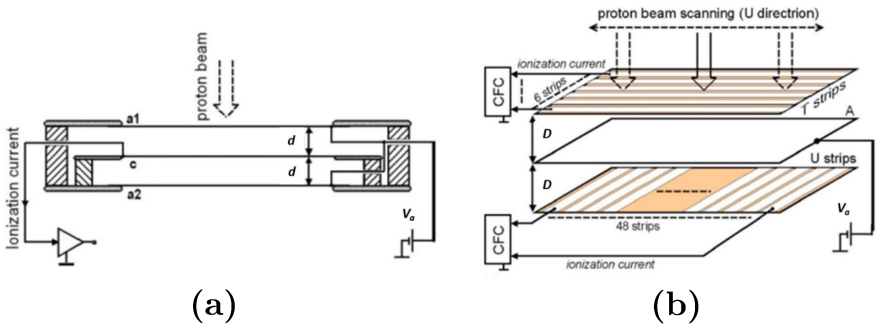

Figure 3.2 – a) Schematics of IC1 and IC2 of the PSI parallel-plate ionisation chambers b) Schematics of strip ionisation chamber. [50]

The last IC measures the beam profile and beam position including the flatness and symmetry of the beam. To measure a beam profile or beam position, the anode of the ionisation chamber is split up into strips or wires. The wires are 4 mm wide Aluminium strips with a 0.4 mm spacing between two strips. The strips provide readings of the beam profiles in two directions with 48 channels in the direction of the proton beam scanning and 6 strips in the direction of the electric field. The geometry size is $47.5 \times 22.2 \times 11.0$ cm^3 [54].

In the heavy ion facility in CNAO, Pavia, Italy, five ion chambers are used, two to integrate the beam flux, two strip chambers and one pixel chamber to measure the beam position and beam width. The ICs' material interaction with the beam corresponds to 0.9 mm of water equivalent thickness (WET) and is one of the main contributions to lateral beam dispersion. It is minimised by installing the system close to the patient [55]. Moreover, commercialised treatment centre solutions supplied by Ion Beam Application (IBA), Louvain-La-Neuveuse, Belgium, use four large 32×32 cm^2 integral and segmented ion chambers with 15 Mylar foils separated by 5 mm air gaps. The time resolution is 500 µs and spatial resolution is 20 µm. The WET of around 0.19 mm is almost five times smaller than the WET of the beam monitors of CNAO [56].

Therefore, material reduction to reduce multiple Coulomb scattering and increasing the readout speed are significant factors. However, with new treatment technologies arising, which will use 10 times higher current, ionisation chambers will have difficulties to cope due to the recombination effect [57].

Ionisation chambers at iso-centre

Ionisation chambers used as a reference instrument or field instrument are the current code of practise to calibrate proton beams as stated in the TRS-389 report [48]. Small cylindrical and plane parallel ionisation chambers are used with a cavity volume of 0.1 cm^3 to 1 cm^3 calibrated at a standard laboratory. Water is the reference medium for the measurement of the absorbed dose. Additionally, measurements of the Bragg-peak and SOBP are taken [51]. The relative standard uncertainty of absorbed dose to water for a clinical proton beam, based on a chamber calibration with ^{60}Co gamma radiation can be up to 2.3% [48].

Combining multiple ionisation chambers led to the development of multi-channel devices. These can be either a 2D array of multiple cylindrical ICs or even a 3D array where multiple stacks of ICs are put behind each other. The latter enables to measure the depth dose distribution in a single measurement. For the QA of the PSI Gantry 2, a system was developed with 128 ionisation chambers (Multi Leaf ICs) with a total length of 35 cm. Together with a dedicated readout system all 115 clinical used energies are verified in a minute with a range accuracy of 2.27 mm, which would take the same amount of time for one energy with conventional methods [58]. Also, manufactured by IBA Dosimetry, Schwarzenbruck, Germany, the "Zebra" is available with 180 ion chambers and 0.5 mm range accuracy. 2D arrays can easily measure the flatness and lateral profiles for QA. Examples are the Matrixx Evolution by IBA with 1020 ICs with a chamber diameter of 4.5 mm and a distance of 7.62 mm between ICs and the Octavius Detector 1500, PTW, Freiburg, Germany with a 4.4 mm chamber diameter and a distance of 7.1 mm.

3.2 Film

Film has been fundamental to the development of radiology, radiation therapy and radiation protection [52]. Radiographic films are mainly used to image X-ray beams. They consist of a suspension of silver bromide (AgBr) grains, with up to 10% silver iodide in a gelatine matrix, bonded in a polyester base material. The size of the grains is from 0.2 µm to 10 µm. X-rays produce electrons through the photo-electric effect, which recombine with the silver ions to form a latent image [59]. In a chemical process, bromine is removed and the presence of elemental silver is detected optically and related to the absorbed dose [52].
The film appearance is expressed in terms of optical density (OD) [59]:

$$OD = log_{10}\left(\frac{I}{I_0}\right), \tag{3.3}$$

where the ratio of I/I_0 is the called the Transmission T, I is the transmitted irradiation and I_0 the source of the irradiation.

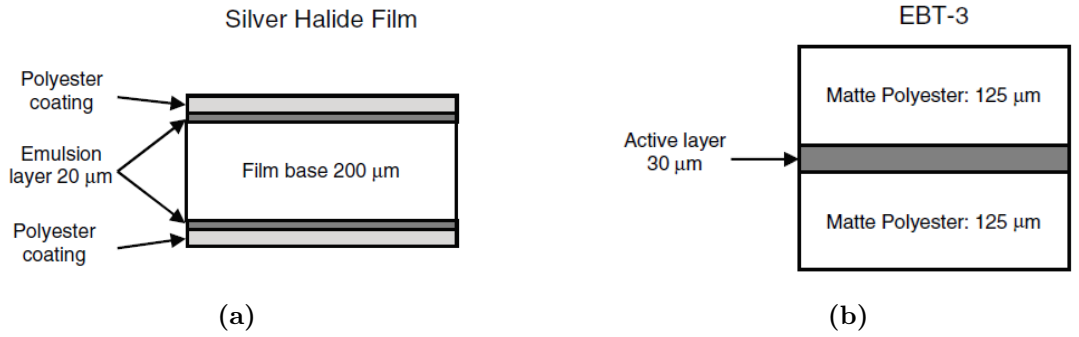

Figure 3.3 – Cross-sections of (a) radiographic silver halide film and (b) radiochromic EBT-3 film [59].

Mainly used for radiotherapy dosimetry are poly-diacetylene-based **radiochromic films**. The $GAFCHROMIC^{TM}$ films were introduced in the early 1990s by International Specialty Products, Wayne, NY, USA [60]. Their weak energy dependence, high spatial resolution (1200 lines per mm), near tissue equivalence and easy handling is very beneficial for QA procedures. Further, the main advantage of the films is their insensitivity to visible light [52]. With exposure to ionising radiation, a dye is created by polymerisation, connecting monomer molecules to

chains, which results in a change of colour. Also, no separate chemical development process is needed. The currently used film EBT-3 is the third generation with an active layer of 23 µm embedded in matte polyester of 125 µm thickness (see Fig. 3.3). The film is read out by a flatbed scanner using RBG channels. The total dose can be up to 100 Gy [60], before the film saturates.
The logarithmic film response can be described using a calibration equation containing a linear and single power term [61]:

$$D = b \cdot netOD + c \cdot netOD^n \tag{3.4}$$

The following equation was shown to provide a good description to the observed behaviour.

$$\zeta = (-1) \cdot \frac{netOD^{\frac{2}{3}}}{ln(netOD)} \tag{3.5}$$

The parameter ζ is found to show a linear relationship with dose within $\pm 2\%$.

The main disadvantage of using film is the post processing time. It is recommended to read out the film 8 h after the irradiation due to the slow polymerisation reaction. However, it is reported that the polymerisation does not stop, so the film should be analysed after 24 h at the latest. They are also energy dependent and should be stored at constant temperature. During the readout the orientation of the films for calibration should not change, since they are polarisation sensitive [59].
The main application of radiochromic film includes the provision of high-resolution maps of two dimensional dosimetric parameters of particle beams [52].

3.3 Silicon semiconductor detectors

3.3.1 Principles of silicon semiconductors

In solid state physics, elements are separated between insulators, semiconductors and conductors. The difference is defined by their crystalline structure and the number of electronic states per energy and volume (electronic density of states). The sum of all states in the structure is called bands. The highest occupied band is called the valence band and the lowest unoccupied or partial occupied band is called the conduction band. The probability, that bands are occupied by electrons, is given by the Fermi-Dirac distribution:

$$f(E,T) = \frac{1}{e^{(E-\mu)/k_b T} + 1}, \tag{3.6}$$

where E is the energy, μ is the chemical potential, which is a state with a 50% chance of being occupied, k_B is the Boltzmann's constant and T is the Temperature. At T=0 K, the chemical potential is equal to the Fermi-energy. If the Fermi-energy is within the conduction band, the structure is a conductor, e.g. iron or gold, electrons can move freely. If the Fermi-energy is within the gap between valence band and conduction band, the structure is an isolator. However, with increasing temperature, the Fermi-Dirac distribution is smeared by $\delta E = k_\mathrm{b} T$ around μ. If the band gap is small (below 3 eV), at room temperature, there is a probability that electrons from the valence band are occupying states in the conduction band. These structures with small band gaps are semiconductors, e.g. silicon (Si) or germanium, which are insulators at T=0 K, but have thermally excited conducting electrons at sufficient temperatures. Insulators, e.g. glass (SiO_2) or diamond (carbon) have band gap values of more than 5 eV and all states in the valence band are occupied [62, 63].

Focussing on silicon in its pure (intrinsic) form, it shares its four valence electrons with four neighbouring Si atoms and forms covalent bonds. The formed crystal lattice of the Si atoms is a tetrahedron. The bonds fill up each Si valence band with eight electrons. The binding energy of the electron is 1.1 eV, corresponding to the band gap value. At room temperature (300 K), the thermal energy $\delta \mathrm{E} = \mathrm{k_b T}$ is only 0.026 eV, very small compared to the band gap and to excite electrons.

Thus, the intrinsic Si semiconductor would be still an insulator. However, the conducting properties are changed drastically, if impurities are introduced in the Si lattice with a small amount of different elements [64].

The process is called doping and creates extrinsic semiconductors. The aim is to induce an additional amount of electrons in the conduction band by replacing a Si atom in the lattice by an element with five valence electrons, e.g. arsenic (As) or phosphor (P). The fifth electron of As in the SiAs lattice is not participating in a covalent bond and is loosely bound to the As ion. Therefore, the extra electron has a very small binding energy of about 0.01 eV to the conduction band and can easily jump to it by thermal excitation. The electron is called the donor electron and the energy state is called the donor band. Such semiconductor is a n-type semiconductor (see Fig. 3.4a) [64].

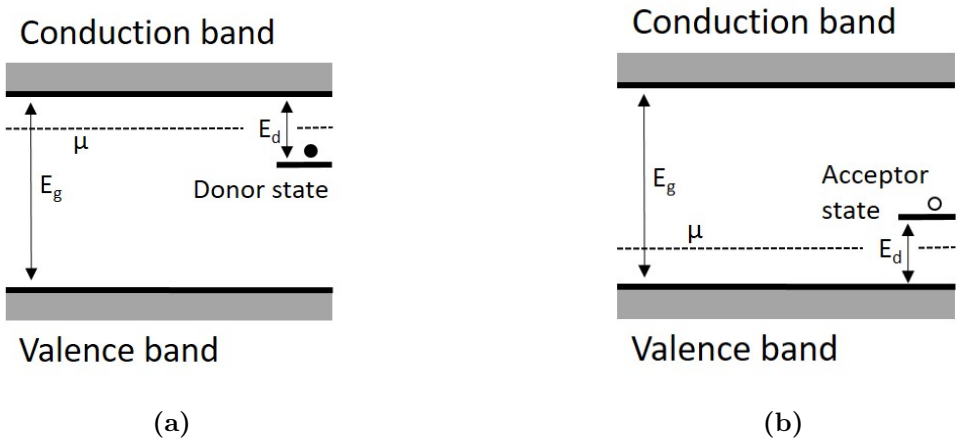

Figure 3.4 – a) N-type semiconductor b) P-type semiconductor

In the same way, elements with three valence electrons, e.g. boron (B) or aluminium (Al), can be used to form three covalent bonds with the Si atoms and one unsaturated bond, which lacks one electron and has a hole. The hole can be filled by a neighbouring electron and creates a hole in its previous position. Thus, the hole can move away and around the boron ion. The hole has a slightly higher energy level than the valence band and at room temperature, electrons can easily fill the hole and create holes in the valence band. The hole is thus the acceptor and the band is called the acceptor band. Such semiconductor is a p-type semiconductor (see Fig. 3.4b) [64].

The electrons in the n-type semiconductor and the holes in the p-type semiconductor are majority charge carriers. Holes in the n-type and electrons in the p-type are also present, but usually 10,000 times less, thus they are called minority charge carriers [62].

The p-n junction

Most applications of semiconductors are based on the inhomogeneous combinations of p-type and n-type semiconductors. The simplest example is the junction between one of each type, the p-n junction (see Fig. 3.5). If both types are joined, electrons from the n-type diffuse into the p-type and holes from the p-type diffuse into the n-type. During the diffusion, holes and electrons recombine. The region is absent from mobile charge carriers and is called depletion layer. Only the charged dopant ions remain and create an electric field, which stops the diffusion process [62].

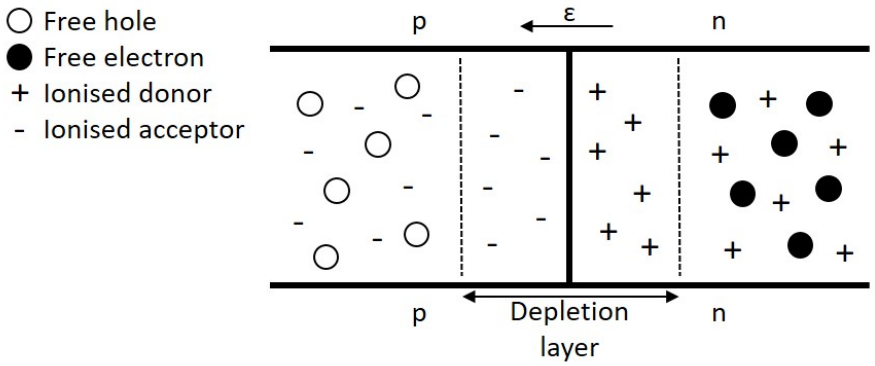

Figure 3.5 – P-n junction and forming of the depletion layer.

In a silicon semiconductor detector, ionising radiation traverses through and the deposit energy leads to a creation of electron-hole pairs. If these pairs are created in the depletion layer, the holes would drift to the p-type and the electrons to the n-type. To count the created pairs, an external reverse bias voltage is applied to separate the charges further and collect them at the electrodes (see Fig. 3.6). The negative potential is applied to the p-type and the positive potential to the n-type of the junction and the result is an extension of the depletion layer, since the

majority charge carriers are pulled towards the electrodes. However, the minority charge carriers are diffusing through the depletion layer and an unwanted leakage current, although very small, is detected. The leakage current is also a sign of damage in the silicon crystal. Mostly, radiation induced electron-hole pairs created in the depletion layer are the source of the detected current [64].

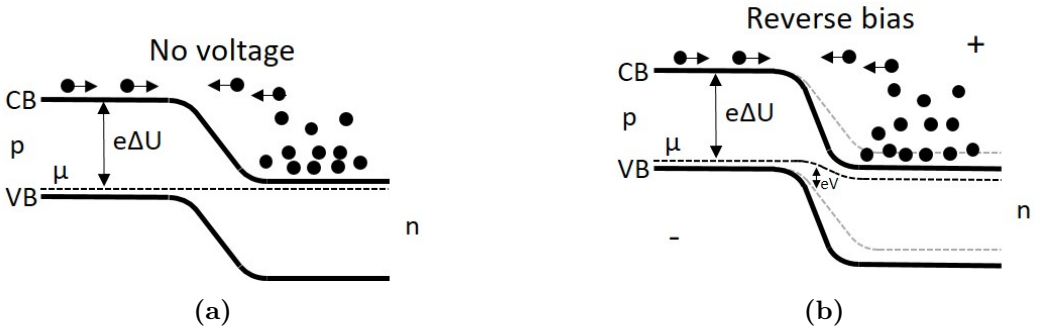

Figure 3.6 – a) P-n junction without voltage b) P-n junction with reverse bias voltage

3.3.2 Current technologies for radiotherapy

In high energy physics and particle accelerator physics, silicon detectors have a broad application spectrum [65]. At the LHC, all major experiments use the technology to detect subatomic particles resulting from proton proton collisions. In ATLAS for example, the silicon semiconductor tracker contains 61 m^2 of silicon detectors, with 6.2 million readout channels, but particle tracks can still be resolved to 200 μm [66].

However, silicon semiconductor based detector technologies for proton therapy are not commonly used. If currently used ionisation chambers had to be replaced one to one, the silicon detectors are interacting with the entire proton beam. Therefore, the limiting factors to apply these Si technologies are the lack of radiation hardness and the corresponding radiation damage in its bulk, signal pileup and readout complexity, which prohibits them to be widely used as monitors for high flux therapeutic beams [67, 68]. However, the potential use of silicon devices for conventional radiotherapy was reported early in 1963 [69], mentioning the advantage in sensitivity and size.

The most common application in proton therapy are single point detectors for QA measurements at the iso-centre. For small field dosimetry, silicon diodes were developed for proton beams and tested successfully with a linear response to dose [70]. Silicon microdosimeters are essential to measure the linear energy transfer (LET), defining the mean deposit energy per path length of a charged particle and proved to be advantageous over other existing detectors due to their small size [71, 72, 73].

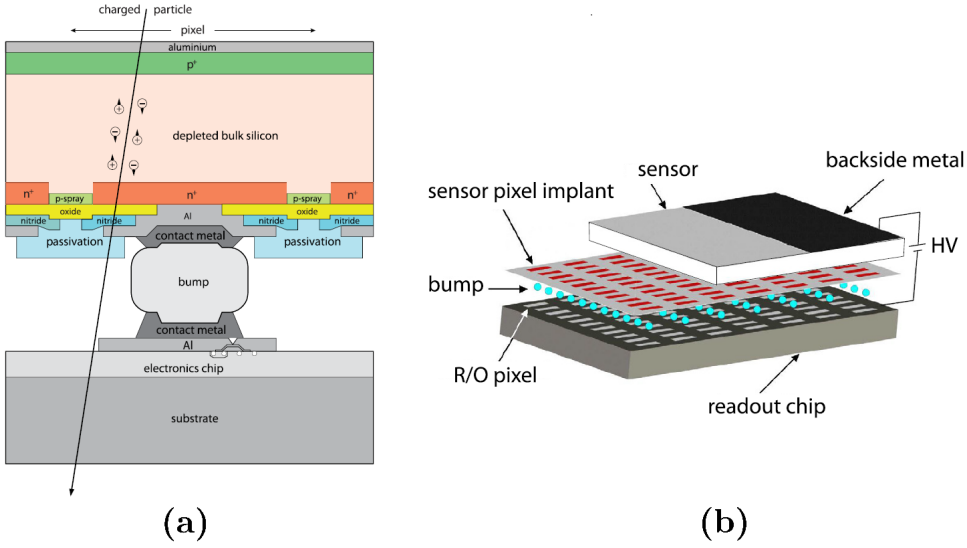

Figure 3.7 – a) Layout of a single cell of a hybrid pixel detector used for Medipix3 and Timepix3 b) Hybrid pixel matrix [74]

However, for beam monitoring within the beamline or nozzle, no technologies have been implemented, but new types are arising. H. F.-W. Sadrozinski et al. [75] proposed an ultra-fast silicon detector with 20-50 µm spatial resolution and 10-30 ps time resolution. The sensors are 50 µm thin. These low-gain avalanche detectors (LGAD) have a $n^{++} - p^{+} - p - n^{++}$ structure to achieve charge multiplication. At preliminary beam tests with proton beams from 62 to 227 MeV, the aim was to measure the bunch length by resolving the bunch structure, to determine the beam energy by using the time-of-flight method and to count single protons [76, 77].

Besides the LHCb VELO detector modules, detectors originally designed for the LHC at CERN were adapted for proton beam therapy in recent years. First and foremost, the Medipix3 and Timepix3 pixel readout chips, initially developed by

the CERN Medipix and Timepix Collaboration for particle tracking, have been applied for imaging of proton beams (see Fig. 3.7). The hybrid pixel detectors are based on CMOS technology with a 256×256 pixel matrix with a size of 55×55 μm^2 to 110×110 μm^2 and a time resolution of 1.56 ns (Timepix3). The Medipix3 sensor was used to characterise 60 MeV proton beam currents and sizes in comparison to film measurements [78]. A sufficient count rate linearity was reported and beam profiles were detected in real time.
The Timepix3 detector allowed characterisation of secondary radiation and determined their angular distribution from a therapeutic carbon beam in a water tank [79]. A cluster pattern recognition was used to identify low energy events such as gamma rays or particles produced during fragmentation such as protons.
Timepix3 was also applied for the CERN proton synchrotron to monitor the beam profile bunch by bunch using the ionised rest gas in the vacuum pipes [80]. After applying cluster findings and filters, the beam size was correctly measured to 0.05 mm accuracy and bunches spaced 254 ns were resolved.

Moreover, silicon strip detectors of similar technology used for the ATLAS experiment at CERN accurately measure the proton trajectory and energy loss [81]. Six strip detectors in two sets will be placed before the patient head and six behind, which are able to measure the high beam fluence and beam size and shape. Behind the detectors is a range telescope, which is used for patient imaging with a very low fluence to track the proton particles [82].
Further, a 2D silicon-segmented detector with 21×21 pixels in total was developed. The pixel elements had a size of 2×2 mm^2 and a distance of 3 mm between pixels. It was used for dose verification measuring points at the SOBP and lateral dose profiles [83]. The measured SOBP shows a good agreement with a single diode and also a good linearity in the dose range of 20–5000 cGy.

Several silicon technologies have been described for a variety of applications. However, all have in common that they are still directly interacting with the beam. Especially for the Medipix and Timepix applications to measure the beam size, the small number of pixels is not able to cover entire fields. An increased size comes with a high cost. Thus, a non-invasive approach is highly desirable, since the proton beam will pass through the detector undisturbed and the lifetime of the detector will be increased significantly.

3.4 Summary

Beam diagnostics are essential for medical accelerator systems to assure effective delivery of the beam and maintain patient safety for cancer treatment. Important characteristics such as sensitivity, resolution, measurement speed and reliability need to fulfil the requirements of a proton beamline. During the measurement campaign, an ionisation chamber, films and the VELO detector modules as silicon semiconductor detectors were used. The principles of all three detector types were described. Furthermore, their applications in radiotherapy were presented. Ion-chambers as the current backbone are used for dose and beam profile monitors in the treatment head and as QA instruments at iso-centre. However, they are intercepting the beam and the measurement speed is rather slow, which will be an insufficient quality for arising high dose rate treatments. Films have been used since the beginning of radiation therapy for QA measurements. Their high spatial resolution and easy handling makes them still a useful tool despite the long post processing time. Silicon semiconductor technologies are well established in high energy physics experiments, but not commonly used as a QA tool in medical accelerators yet. They excel in their sensitivity, size and readout speed, but are lacking in radiation hardness. Novel, silicon-based pixel detectors are developed and first tests with proton beams were conducted. However, most are still interceptive devices.

4 The LHCb VELO detector modules

The non-invasive online beam monitor is based on the VErtex LOcator in the Large Hadron Collider beauty experiment (LHCb VELO) at CERN [84] (see Fig. 4.1). The VELO detector modules are used to reconstruct production and decay vertices of beauty- and charm hadrons [85]. In the following section, the setup and technology of LHCb VELO at CERN is summarised [86]. Highlighted are the parts which are particular important for the stand-alone system of the detector modules, setup in the Cockcroft Institute (CI). In the last section, the specific adaptations are discussed, which were necessary for a stand-alone operation independent from the CERN environment.

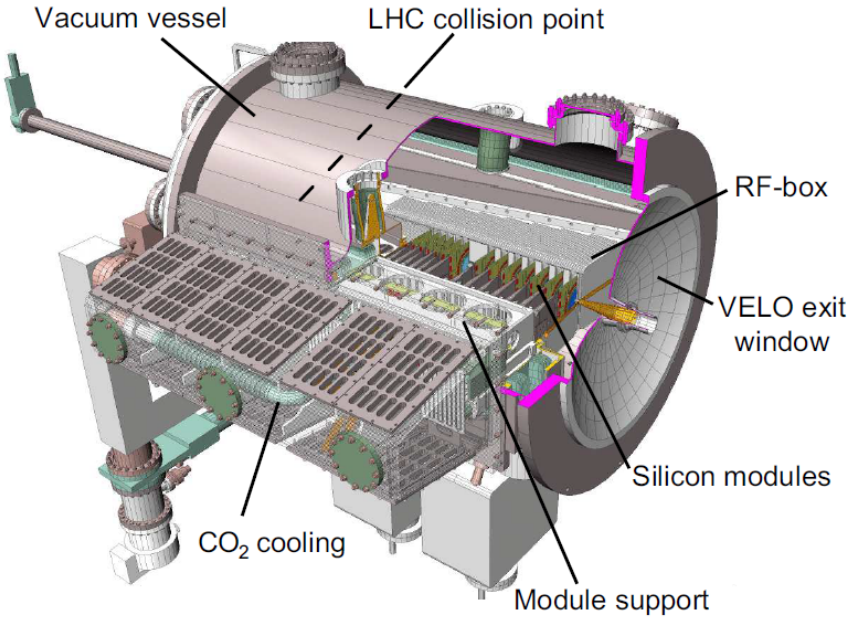

Figure 4.1 – Overview of the complete LHCb VELO experiment at the LHC in CERN. There are 42 silicon detectors in total to pick out produced B mesons. [84]

4.1 LHCb VELO technology

The VELO detector modules are semi-circular silicon micro strip detectors. The design of VELO was chosen according to the four main requirements of the tracking system, operating in the harsh LHCb environment [84].
The signal to noise ratio had to be greater than 14 and the overall channel efficiency was required to be at least 99%. The resolution of a spatial cluster had to be about 40 µm for 100 mrad tracks in the smallest pitch region. Also, the silicon of the VELO detector had to withstand the extreme radiation environment for one nominal year of accumulated luminosity of 2 fb equivalent to 1 MeV neutrons with a flux of 1.3×10^{14} $\mathrm{n_{eq}}$ cm^2 [87]. This enables the operation in the LHC beam pipe in vacuum conditions for precise measurements of the track coordinates.

4.1.1 Sensor

Several characteristics of the VELO detector modules are summarised in Tab. 4.1. Each VELO module comprises a semi-circular silicon micro strip detector with 300 µm thick silicon of type $n^+ - in - n$ (see Fig. 4.2) [88]. The bulk consists of lightly doped n-typed silicon. On top, shallow strips of n^+-type silicon are implanted and a layer of p-spray is used to maintain the isolation between the implants. While irradiation creates electron-hole pairs, a type inversion converts the n^+-type silicon by decreasing the dopant concentration to a p-type and an applied high voltage (reverse bias) up to 500 V depletes the sensor. Aluminium readout strips, isolated by a silicon oxide layer (SiO_2) and connected to a double metal routing layer, transfer the charge to the readout electronics [89].

Table 4.1 – Characteristics of the VELO detector modules.

	R-sensor	PHI-sensor
Silicon technology	$n^+ - in - n$	$n^+ - in - n$
Number of readout channels	2048	2048
Thickness of sensor [µm]	300	300
Number of sectors	4	2
Pitch [µm]	38.0–101.6	37.7–97.0
Radius of active area [mm]	Min. 8.1700 Max. 42.0000	Inner 8.1860–17.2105 Outer 17.2105–41.9840
Angular coverage [°]	180	182
Stereo angle [°]	/	Inner 20.00 Outer 10.35

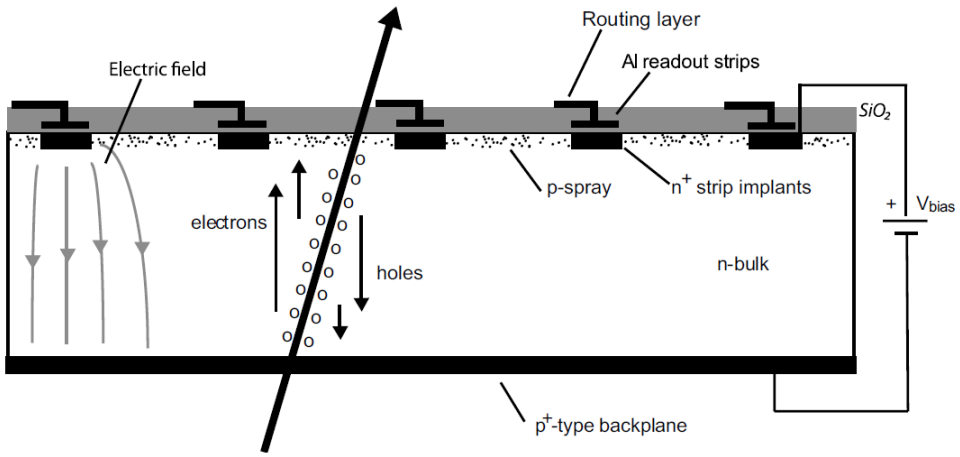

Figure 4.2 – Cross-section of a VELO silicon sensor of type $n^+ - in - n$. When ionising particles hit the bulk and create electron-hole pairs, the bias voltage depletes the sensor, so that electrons drift towards the implants. A SiO_2 layer forms an AC coupling to the strip implants. The Aluminium readout strips transport the signals to the front-end electronics via the routine layer. [89]

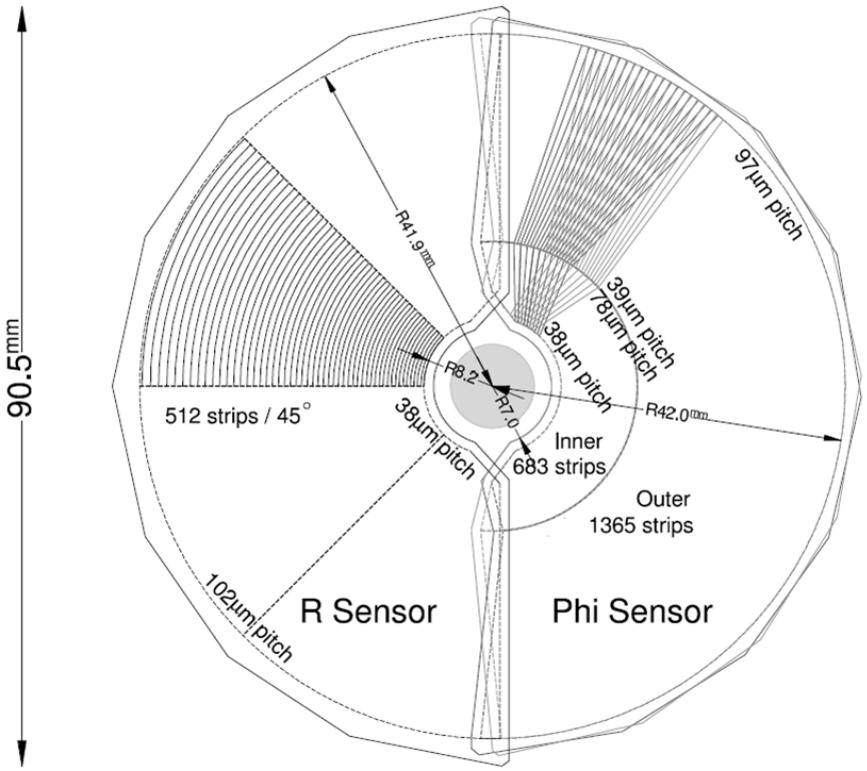

Figure 4.3 – Schematics of the VELO R-sensor and PHI-sensor. Each sensor consists of 2048 readout strips. The R-sensor is structured in four sectors with radially oriented strips and the PHI-sensor consists of two sectors and angled strips. [84]

The VELO detector combines two sensor types that are glued to each other with a different strip geometry, the R-sensor and PHI-sensor (see Fig. 4.3). Each sensor has 2048 strips with an active area covered by an inner radius of 8.2 mm to an outer radius of 42 mm.

The R-sensors are divided into four 45° sectors with each 512 concentric semi-circular segmented strips [90]. The inner strip pitch of 40 µm increases linearly as a function of the radius according to Eq. 4.1 [91] to an outer pitch of 108 µm. Thus, it provides the radial position information relative to the origin of the beam axis.

$$pitch\ [\mu m] = 40 + (101.6 - 40) \times \frac{r - 8190}{41949 - 8190} \tag{4.1}$$

The PHI-sensor is divided at the radius of 17.25 mm into two sectors with 683 strips in the inner sector and 1365 strips in the outer sector [92]. The strips are

tilted with a stereo angle in a dog-leg shape, 20° in the inner region, 10.35° in the outer region, providing an angular position information with an angular coverage of 182°. The strip pitch increases linearly in the inner sector from 37.7 µm to 79.5 µm and from 39.8 µm to 96.9 µm in the outer region (see Eq. 4.2 and 4.3).

$$pitch_{in}\ [\mu m] = 37.7 + (79.5 - 37.7) \times \frac{r - 8170}{17250 - 8170} \quad for\ r < 17250 \tag{4.2}$$

$$pitch_{out}\ [\mu m] = 39.8 + (96.9 - 39.8) \times \frac{r - 17250}{42000 - 17250} \quad for\ r > 17250 \tag{4.3}$$

As a result, the geometry enables precise measurements of particle tracks in polar coordinates. The sensor pair is embedded in a module support consisting of a core of Thermal Pyrolitic Graphite (TPG) encapsulated in a carbon fibre (CF) cladding joined with laminated circuits. The TPG acts as a heat conductor with a high thermal conductivity of 1700 $\mathrm{W\,m^{-1}\,K^{-1}}$. The temperature of the module is controlled by two Negative Temperature Coefficient (NTC) sensors. In addition to the structural positioning, the supporting base provides the connection to the electrical readout (see Fig. 4.4).

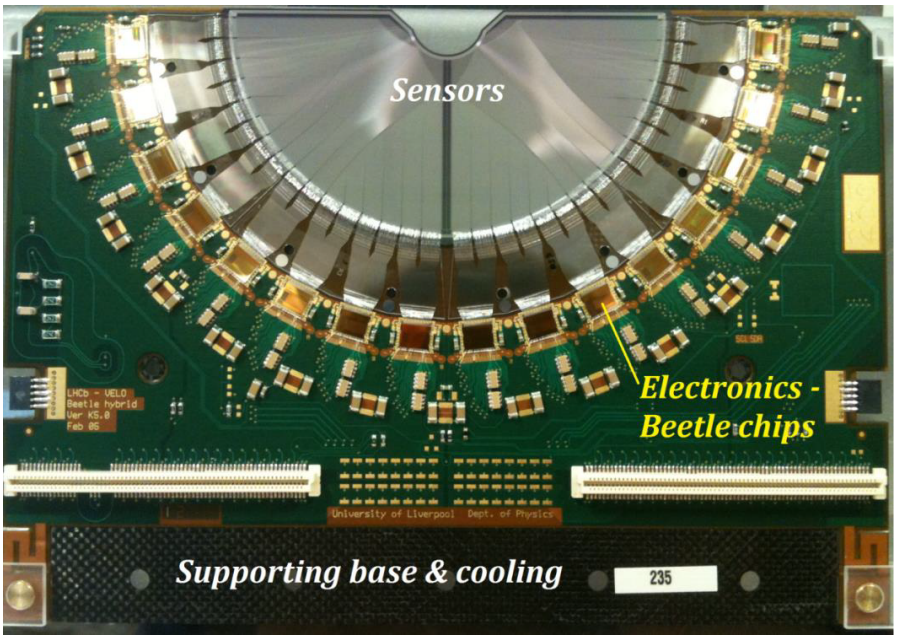

Figure 4.4 – Picture of a VELO module used for beam monitoring in the Cockcroft Institute.

4.1.2 Readout electronics

The VELO detector readout electronics consist of a chain of analogue and digital parts to transfer and process the collected signals from the sensor.
The Beetle chips, the front end (FE) analogue readout chips, integrate the signals received from the sensors, amplify them and transmit them to the repeater boards. The cards on the repeater boards are responsible for forwarding the signals to the digitiser boards and distribute the low and high voltage supply to the modules. TELL1 boards perform the digitisation of the signals and process them further. They also send out readout triggers for the data acquisition. Ultimately, the processed data is sent to a Linux platform based desktop PC to be stored.

Beetle chips

Surrounding the R- and PHI-sensors, 16 Beetle chips, based on CMOS technology, are mounted on each sensor side [93]. Having 2048 readout strips in total, each chip integrates 128 channels of the sensor. The Beetle chips consist of a low-noise charge-sensitive preamplifier and an active CR-RC pulse shaper, which form the analogue front end (see Fig. 4.5). The FE pulse shape is a semi-Gaussian pulse that fulfils the requirements of the application at the LHC beam (see Fig. 4.6). The rise time t_r is not more than 25 ns and the remainder R, which is the ratio between the signal voltage 25 ns after the peak and the peak voltage V_p, has to be below 30%. The output of the front end is sampled with the LHC bunch-crossing frequency of 40 MHz into a 160 deep analogue pipeline. An additional amplifier transfers the signals in 4 ports (Multiplexer), from where they are transferred out to the repeater boards via thin, flexible and radiation hard Kapton cables. The Beetle chips can be controlled by an $\mathrm{I}^2\mathrm{C}$ interface.

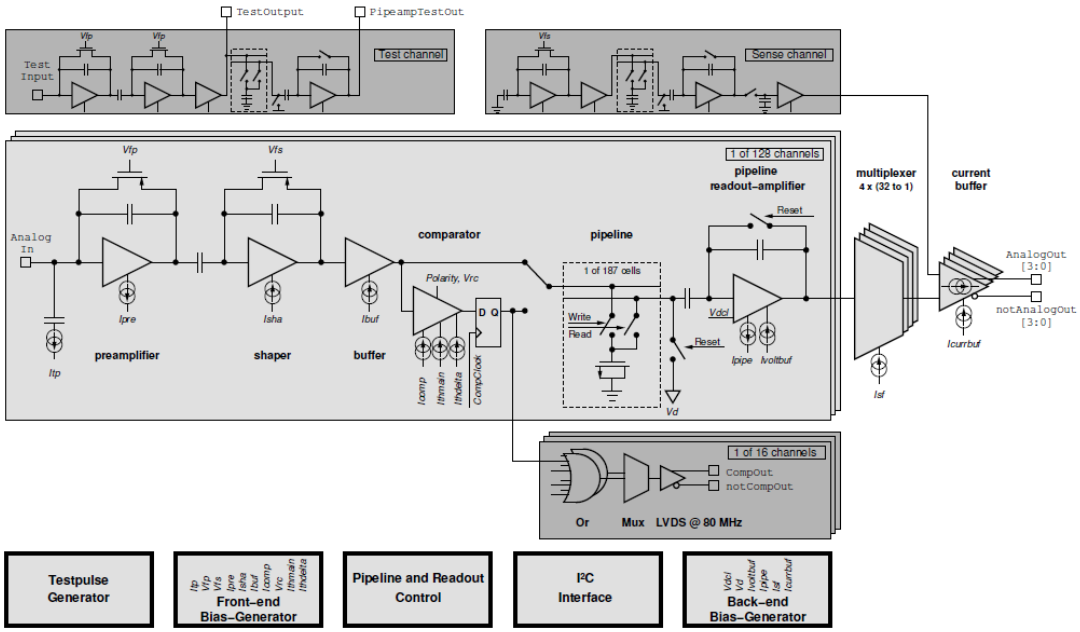

Figure 4.5 – Schematic block diagram of the Beetle readout chip. Sampled analogue signals are amplified, shaped and stored in a buffer until a readout signal is received. [93]

The operation of the chips produces approximately 27.5 W of heat per sensor, which needs to be dissipated. The waste heat is taken away by evaporators, small rectangular aluminium blocks with embedded coolant pipes inside, which attach on the base of the detector and the above described TPG. Moreover, liquid CO_2 is used to achieve a continuous cooling temperature of $-7\,°C$ at CERN that falls into the required temperature range for a long life-cycle operation between $-30\,°C$ and $0\,°C$ [94]. The CO_2 supply into the evaporator is realised by the 2-Phase Accumulator Controlled Loop (2PACL) method. Adaptations of the cooling system for the stand-alone setup will be discussed in section 4.2.

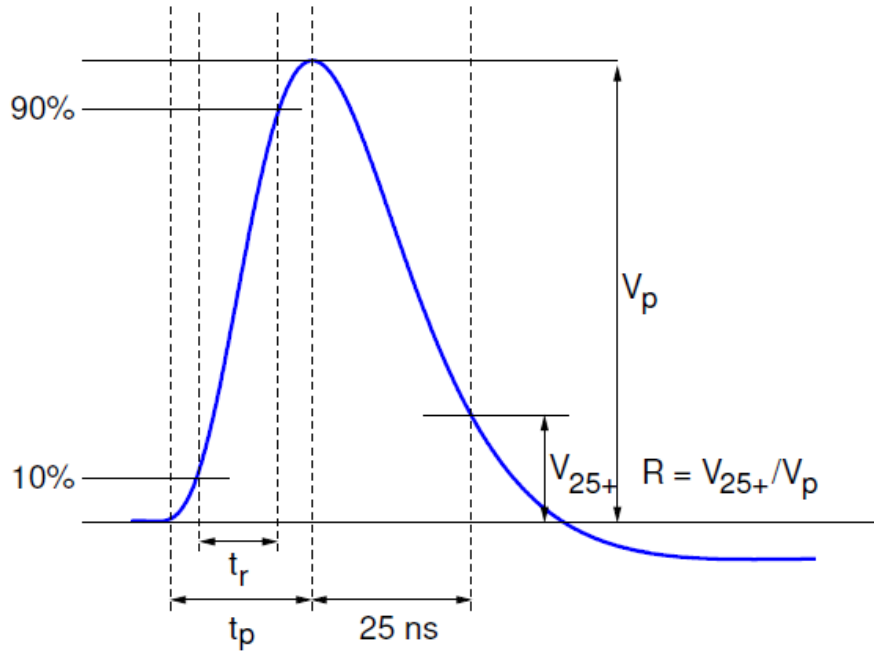

Figure 4.6 – Pulse shape of the output of the Beetle chips. The rise time t_r is not more than 25 ns and the remainder R has to be below 30% to meet the requirements of the LHC bunch-crossing. [93]

Repeater boards

The repeater boards control the LV and HV power supply and manage the signal transfer. One board consists of six mezzanine cards in total; four repeater driver cards, one low voltage (LV) card and one Experiment Control System (ECS) card [95].
The four repeater driver cards receive the signal pulse from the four ports of the Beetle chips and amplify them to overcome losses introduced by long transfer cables. The cables leading to the TELL1 boards are 60 m shielded CAT6 cables.
Powered by a LV desktop power supply, the LV card supplies the power to the Beetle chips and the remaining mezzanine cards. Voltage regulators on each board monitor the voltage amplification.
The ECS card repeats the I^2C commands and controls the LV regulators.

TELL1 boards

The Trigger Electronics and Level 1 (TELL1) board (see Fig. 4.7) is an electronic acquisition readout board and serves to digitise and process the readout of the analogue data from the front end electronics [96, 97]. The TELL1 board has four analogue receiver (ARx) cards. Each card has an input of 16 links with 32 channels per link to readout every strip channel ($4 \cdot 16 \cdot 32 = 2048$). The 64 ARx links digitise the signals with 10 bit Analogue to Digital Conversions (ADCs) sampling at 40 MHz. The data is either in a non-zero-suppressed (NZS) or zero-suppressed (ZS) format. NZS data carries full raw data information. The signals of the ARx cards are directly connected to four Pre Processor FPGAs that are responsible for the data synchronisation and data processing in the LHCb experiment.

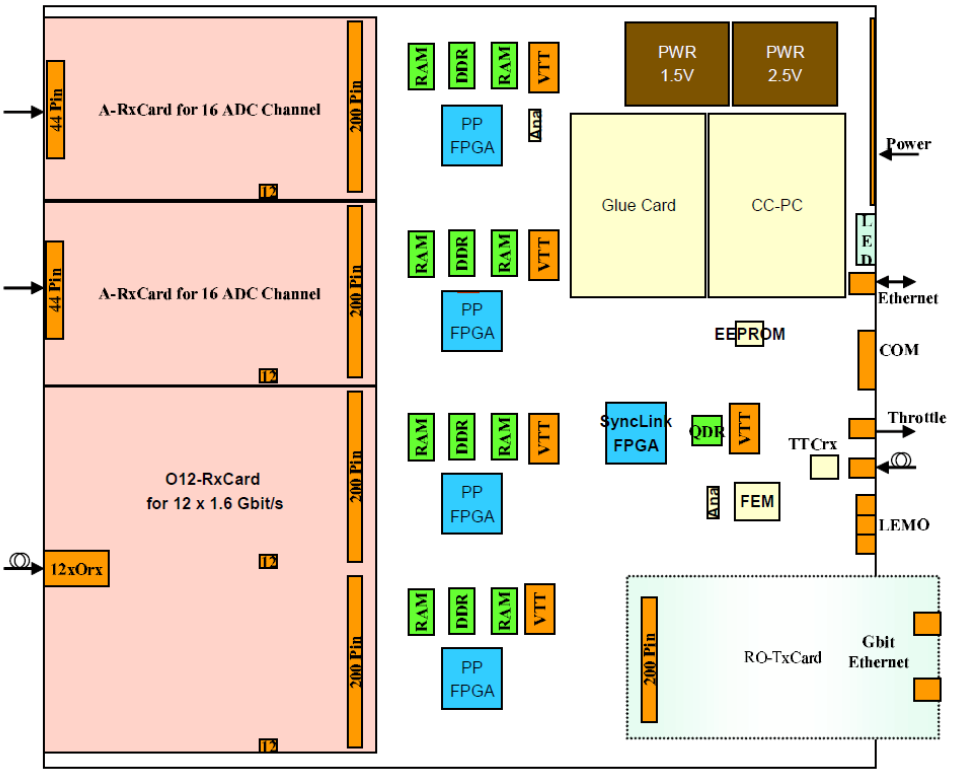

Figure 4.7 – The layout plan of the TELL1 board with its major components. For the LHCb VELO system, the optical receiver card (ORX) is substituted by two more ARx cards. The LEMO connectors can be used to inject external trigger (see section 4.2). [97]

The main processing steps are the following:
Header cross-talk: The analogue data chain of 32 channels from the Beetle chips carries header bits, which encode the four ports (Multiplexer) and the position in the Beetle pipeline buffer. With cross-talking, a fraction of the signal in the last header bit spills over into the first Beetle channel of the link and makes it appear noisy, if not corrected. A careful calibration of the signalling cables removes it [98].
FIR filter: Long data cables result in signal distortion due to cross-talking. A digital Finite Impulse Response filter corrects it [89].
Clustering: Once all previous corrections are applied, the last step of the processing is clustering [99]. When an ADC count passed a certain threshold, a seeding strip and up to three additional adjacent strips are added to the cluster, if their values are above the inclusion threshold. The threshold for noise suppression can be set individually depending on the Signal-to-Noise ratio [100].
Due to significant differences between the bunch structure (both in time and space) of the LHC and medical proton beams, it was not possible to perform the hit reconstruction and final event building on the TELL1 boards. Instead, the pass-through mode was used and the full raw data was stored using external trigger systems, described in sections 4.2.3 and 4.2.4.

Further parts of the TELL1 board are the Credit-Card PC (CCPC) and the Gluecard [101]. Both parts are used to send out I^2C commands for initiating the data acquisition of the Beetle chips and readout triggers. The CCPC has a Linux base system and is accessed via LAN connection. It has no actual storage and the Linux desktop computer acts as a server and booting machine for the CCPC. Ultimately, the processed data is then stored in buffers until a transfer is initiated to a computer by a High Level Trigger (HLT) [102].

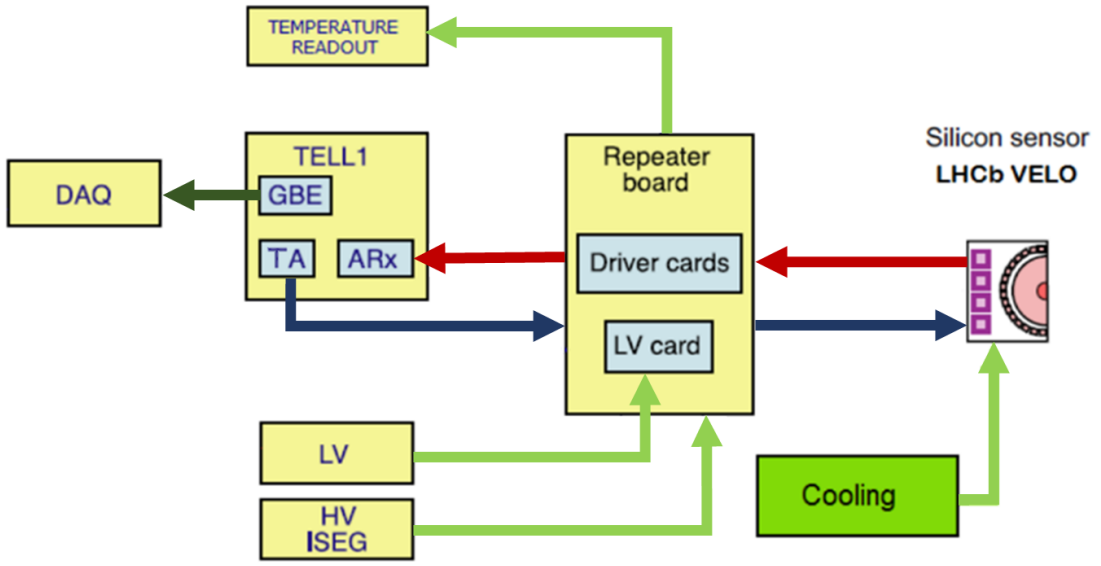

Figure 4.8 – The main readout process with the electronic parts. A readout trigger is sent out by the TELL1 board via the Repeater board to the Beetle chips (violet squares). Modified after [84].

Figure 4.8 summarises all electronic parts in the readout chain for the LHCb experiment. Trigger adapters (TA) send out the readout triggers from the TELL1 board via the Repeater boards to the Beetle chips. External power and cooling supplies guarantee a smooth operation.

4.1.3 Trigger and Timing control for the LHCb VELO detector

The stand-alone setup of the VELO detector modules requires modifications to synchronise the readout and therefore, a closer look at the VELO timing and trigger system and its configuration is needed [102, 103].
The readout electronics are designed to work in synchronism with the LHC bunch crossing frequency, $f_{LHC} = 40\,\text{MHz}$. To ensure this, a Timing and Fast Control (TFC) [104] system was installed in the LHCb experiment to distribute the LHC clock and synchronous reset and control commands to the FE electronics. The LV card on the repeater board receives the TFC signals and forwards them to the Beetle chips. As mentioned, Beetle chips sample events every 25 ns and store them in the pipeline with a specific column number (PCN) of up to 160 for each

strip. The sampling is configured with the standard LHCb latency time of 160 clock cycles (1 clock cycle: 25 ns). As a result, an event in a specific PCN, which was recorded exactly 4 µs before, is read out by the readout Level(L)0 trigger, which is sent out by the TELL1 board. The maximum data transfer frequency of the TELL1 board is 1.1 MHz (900 ns), which corresponds to the data train of 36 analogue levels [(4 header bits + 32 channel data) × 25 ns] of each port per Beetle chip. The trigger timing is controlled by the readout supervisor ODIN [105], which broadcasts the clock to the Timing Trigger and Control receiver on the TELL1 board. The digitisation of the received data needs be precisely synchronised to the data sampling of the Beetle chips to avoid a significant signal to noise loss. Therefore, 64 individual phase adjustable clocks in the Pre Processor FPGAs generate a fine delay for a precise digital conversion of the data. Test pulses, sent to the Beetle chips, are used to estimate delays in clock cycles by finding the sampling spot at the peak voltage V_p and thus prevent header cross-talk. Moreover, the determination of the delay includes identifying parameters that account the length of the used cables. An overview about the timing process and the specific delays, which need to be taken into account, is shown in Fig. 4.9. The decision to transfer the data to the storing computer is completed by a L1 trigger, which is a software based trigger. It uses information of the VELO FE electronics and trigger and time subdetectors and matches them to the previously selected events by the L0 trigger.

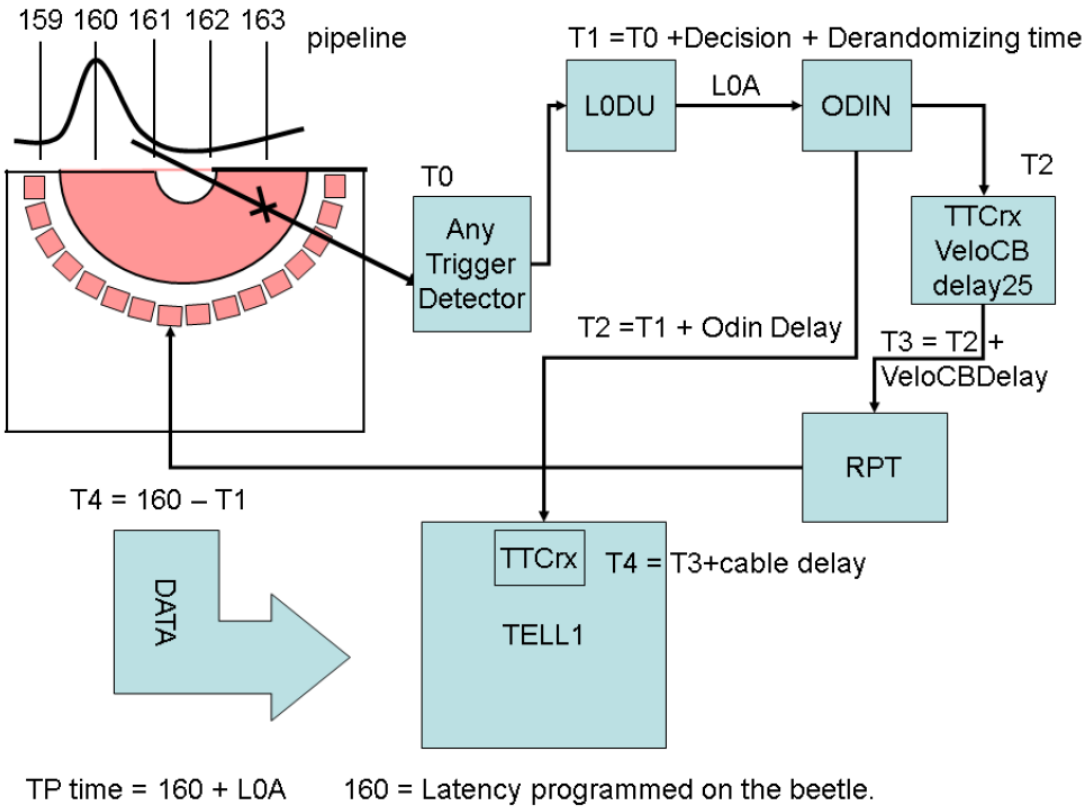

Figure 4.9 – Overview about the timing calibration on real beam data. A trigger decision T0 is done by the TFC system. The readout supervisor ODIN controls the readout of the TELL1 board. The time between the triggered event and the arrival of the readout trigger is exactly 4 µs (160 clock cycles). Hardware and cable delays need to be integrated. [103]

For the stand-alone VELO detector system, neither the TFC system nor the ODIN readout supervisor is available. The process involved in achieving readout synchronisation is discussed in the next section.

4.2 System adaptations of the stand-alone LHCb VELO detector system for medical accelerators

4.2.1 Requirements for the VELO detector modules in a clinical proton beamline

Several changes in the system setup were necessary to operate the VELO detector modules as a stand-alone system outside of the LHC environment as stated above. Two VELO detector modules (see Fig. 4.10) were utilised for this adapted system and set up in a laboratory in the Cockcroft Institute. Alteration and upgrades in the hardware and software of the stand-alone VELO setup are necessary for a synchronised and online data acquisition. Furthermore, adaptations of the setup must fulfil the specific needs of the environment of a medical facility. This includes the development of an effective venting and cooling system and a dedicated rack for the safe and precise positioning and integration within the treatment beamline. The following requirements were necessary for the performance and positioning of the detector.

1. Operation of the VELO modules in ambient air for temperatures of the sensors below 0 °C to prevent degradation of the silicon sensor and suppress noise.

2. Positioning of the VELO modules in the beam propagation direction z and its transverse plane x with an accuracy of 1 mm.

3. Alignment of the VELO modules co-centrically with the beam axis z with an accuracy of 1 mm.

4. Configuration of a new set of delay parameters in clock cycles for correct data sampling of the VELO modules due to hardware and cable changes in the new environment.

5. Matching the readout of the VELO modules with the proton bunch arrival given by the RF frequency of the medical cyclotron to sample at positive points of the output pulse.

The achieved results of the system regarding cooling, spatial alignment, calibration and readout are presented in the following sections.

4.2.2 Adaptations for a clinical environment

The first three items were mostly realised and described in [10]. A few additional optimisations were performed for a smoother operation of the system.

Venting and cooling system: In contrast to the experiments in the LHC, in a clinical environment, the VELO detector modules will be operated in air and the liquid CO_2 cooling had to be replaced. The chosen cooling system had to handle a waste heat load of 27.5 W per sensor and achieve the required operational temperature below 0 °C. The low temperatures are necessary to prevent the glue affixed to the Beetle chips from melting, to reduce the effects of radiation damage and minimise the leakage current to keep the noise levels consistent. In the LHC, the liquid CO_2 cooled the in vacuum operated VELO detector modules to the optimal operational temperature of around −7 °C.
In [10], heat transfer simulations were performed with Finite Element Analysis to determine the cooling requirements and to manage the produced heat load of 27.5 W per sensor. The result of the simulations showed, that a minimum cooling power of 130 W at a coolant temperature of −27 °C at ambient air is needed.

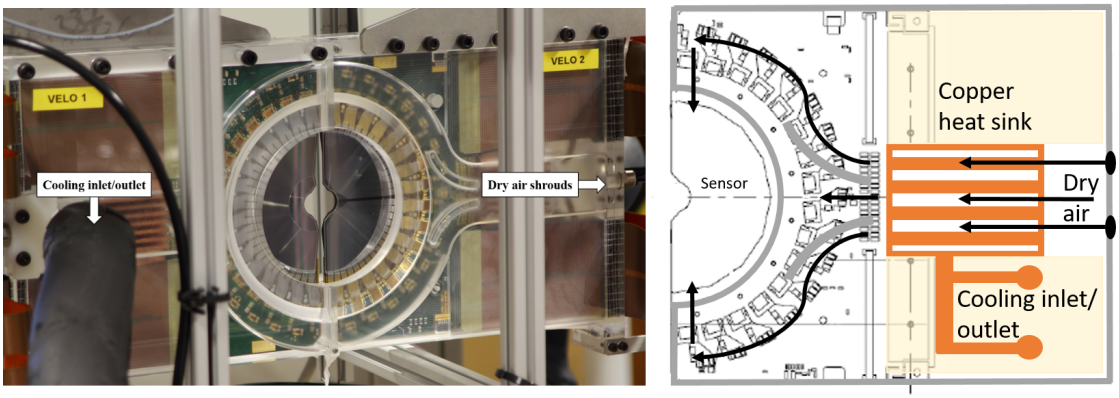

Figure 4.10 – a) The VELO detector modules embedded in a plastic case including the entrance and exit of the cooling and venting pipes b) Schematic of the airflow to guarantee a safe and smooth operation. Signal transmission to additional electronic parts is shown in Fig. 4.8.

Therefore, the ATC K3 chiller with a high cooling capacity of 3200 W and a temperature range of up to −30 °C was selected. The coolant pipes were wrapped with 19 mm thick Amaflex polyethylene insulation to reduce the heat absorption, caused by condensation build-up on the pipes. The low viscosity HYCOOL was used as the cooling liquid. The modules were surrounded by a machined plastic case, which matches the shape of the modules. The semi-circular VELO sensors were left open (see Fig. 4.10). The cooling pipes were fed inside the case to bronze-welded pipes, terminated with a copper heat exchanger, which is in thermodynamic contact with the VELO detector modules. Between the module and the heat exchanger, a 1 mm layer of α-Gel COH-6000LVC by Taica Corporation was applied. Moreover, on top of the heat exchanger, heat sinks were fitted symmetrically on each side to facilitate the heat exchange with the dry air to lower the temperature. The dry air was supplied at 4-4.5 bars with an air flow of 65 l/s with a dew point of up to −70 °C through dry air inlets on either sides of the case by the Ekom DK50 2V-S/M air compressor and a newly added Ekom Nano DL030 dryer. The distance between the TPG base of the module and the case is 5 mm to leave enough space for the cabling and also create a quasi-laminar flow of the dry air along the whole area of the sensor. The temperature of the modules was previously monitored by four Lascar EMT 1900 LCD thermometers, which was then exchanged in further upgrades with a temperature monitoring interface using LabVIEW, National Instruments. The chiller keeps the coolant at a steady temperature of −28 °C and the thermometers record a module temperature below −5 °C during continuous operation at full power of the readout chips.

Positioning system: A dedicated positioning system was designed with three MacLennan THK KR20/KR26 translational slides with individually controlled MacLennan 17HS-240E stepper motors embedded in a rigid aluminium framed stand with height adjustable feet. The guaranteed precision by the manufacturer of the motors and stages allows a positioning accuracy of 10 µm. The available stroke is up to 94 mm in the x-axis and 165 mm in the z-axis. The motors are controlled by a MacLennan custom built SM9859 three axis control unit comprising three microprocessor based ST5-Q controller driver units on shared communication channels using RS485 USB connection. Movement limits were enforced by installing Baumer switches to the end on each slide.
A remote user control interface was written in LabVIEW to calibrate the position

of the modules and to control the motors with Serial Command Language. This enabled to set the translation speed and to introduce a deceleration before the Baumer switches to avoid bringing the system to an abrupt halt.

4.2.3 Electronics and hardware changes

VELO modules: For a smooth operation, several interlocks introduced for the LHCb experiment needed to be removed, including the low and high voltage interlocks and the temperature interlock.
The high voltage power supply of the two detector modules is a floating ground high voltage source-measurement unit (SMU) type EHS 82 05P-F-XXX by ISEG and was used to supply the bias voltage of up to $-500\,\mathrm{V}$. For the connection between the modules and the repeater boards, 40 cm flexible ribbon cables were used instead of long Kapton cables [10].

Repeater Boards: The Experiment Control System (ECS) card was fully removed. The main purpose of the ECS was to forward the I^2C commands to the Beetle chips. Relevant connections were bridged on the board. The low voltage cards of the two modules were supplied separately by four bench-top power supplies; for module one: ISO-TECH IPS 3303 and IPS 1820D; for module two: ISO-TECH 2023 and DIGIMESS SM5020. The latter is used to power the Beetle chips with $3.3\,\mathrm{V}$, whereas the former powers the repeater driver cards with $\pm 6\,\mathrm{V}$. This was a result of the encountered I^2C problems described below.

It is notable, that the communication via I^2C with the Beetle chips created severe issues. I^2C signals need to have a common ground within a preferably intrinsic system. The transmission of the signals via multiple hardware parts to the VELO detector modules makes the communication vulnerable to interference. As a result, different ground potentials for the driver and receiver were observed. To remove these differences, all grounds of the VELO modules, repeater boards and TELL1 boards were connected to a common ground. Furthermore, the LV supplies were chosen to be floating to introduce a voltage drop of few mV in the cables between the modules and the supplies. In the ground lines, running between the modules and the TELL1 readout boards, there is ideally no current flow, so the ground voltage at the modules and the TELL1 should be the same. Otherwise, if the

supply would be tied to the main ground, the return current will be split along two pathways, so a current would be flowing between the modules and the readout boards and create a voltage difference. In order to suppress any noise that can be picked up in the cables, ferrite clamps were installed. These efforts did not eliminate the communication errors completely, however made them manageable, by communicating the signals by a certain sequentially order to the sensors. The origin of the problem is likely caused by dead strip channels or faulty Beetle chips of the VELO detector module one.
Lastly, the 60 m CAT6 signal cables connecting the repeater boards with the TELL1 boards were replaced by shorter 10 m ones. By replacing the longer cables with shorter ones, it was required to establish a new set of calibration values in clock cycles to avoid non-synchronised sampling (Header cross-talk) of the TELL1 board (see Fig. 4.11).

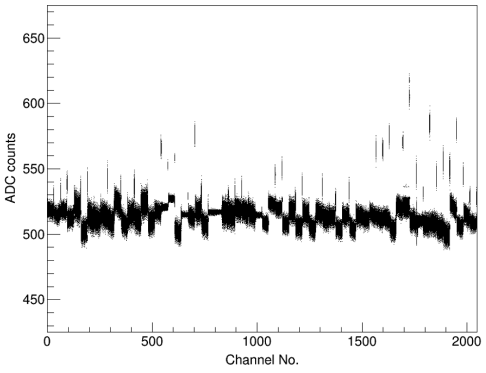

(a) Uncalibrated noise spectrum of a R-sensor.

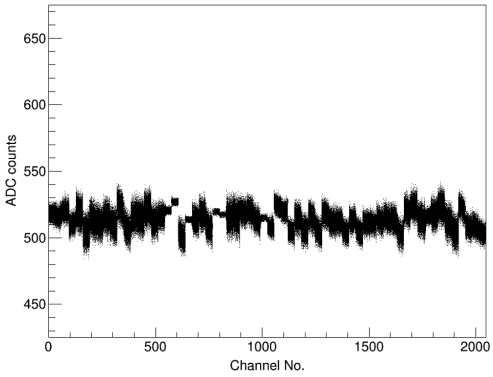

(b) Calibrated noise spectrum of a R-sensor.

Figure 4.11 – Without the configuration of the cable and phase delay in clock cycles, header bits can spill over into the next channel of the link and affect the noise spectrum.

TELL1 boards: Due to the absence of the Timing and Fast Control system and the ODIN readout supervisor, multiple changes had to be introduced for a synchronised data acquisition and readout. Firstly, instead of the ODIN readout supervisor, I^2C readout trigger commands were sent out by small EDA-00978-V1 trigger adapter mezzanine plates, which were implemented on each of the four TELL1 boards.

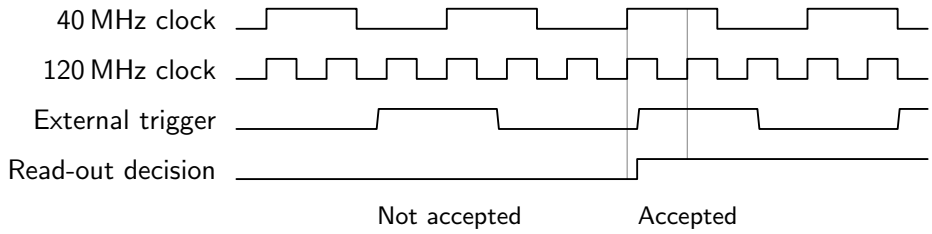

Figure 4.12 – Introduced system to synchronise the proton bunch arrival of a medical accelerator. A readout decision is made, if the rising edge of the external trigger is within the first 0 to 8.3 ns (detected by the 120 MHz clock, shown by the grey lines) of the 40 MHz clock. Other triggers will get rejected.

Secondly, the absence of the TFC system, which synchronises the LHC particle bunch arrival frequency $f_{LHC} = 40\,\text{MHz}$ with the readout chips of the sensors had to be circumvented [106]. The clocks of the TELL1 boards and Beetle chips cannot be changed directly, since non interchangeable quartz crystal oscillators are used to generate the internal frequency. Furthermore, a different frequency, e.g. the RF frequency of a cyclotron, cannot be injected directly. However, the TELL1 boards can be synchronised with another clocked system (not 40 MHz) using the external readout trigger input accepting 3.3 V TTL signals with rising edge detection (see Fig. 4.12). Following a firmware update of the TELL1 boards with the technical support of Guido Haefeli and Oliver Girard, EPFL, Lausanne, Switzerland, the rising edge of the trigger is detected with a newly introduced 120 MHz clock in phase with the 40 MHz TELL1 clock. The trigger is accepted if the rising edge of the external trigger is within the first 0 to 8.3 ns (120 MHz) of the 40 MHz clock and rejects all triggers that fall outside the 8.3 ns window (see Fig. 4.12: readout decision). Therefore, an external trigger of up to 10 kHz will be injected into the TELL1 board with the Keysight 8110A pulse generator. The readout frequency is a result of the chosen output data format *non-zero-suppressed*, limiting the bandwidth frequency by carrying the full raw data information. The pulse generator will be triggered by the sinusoidal cyclotron RF frequency and thus is in phase with the readout trigger. To tune the synchronisation of the proton bunch arrival on the detector and Beetle chips, a coarse delay of multiple clock cycles can be introduced by changing the L0 latency setting of the TELL1 board or the pulse generator can add a fine delay in ns steps.

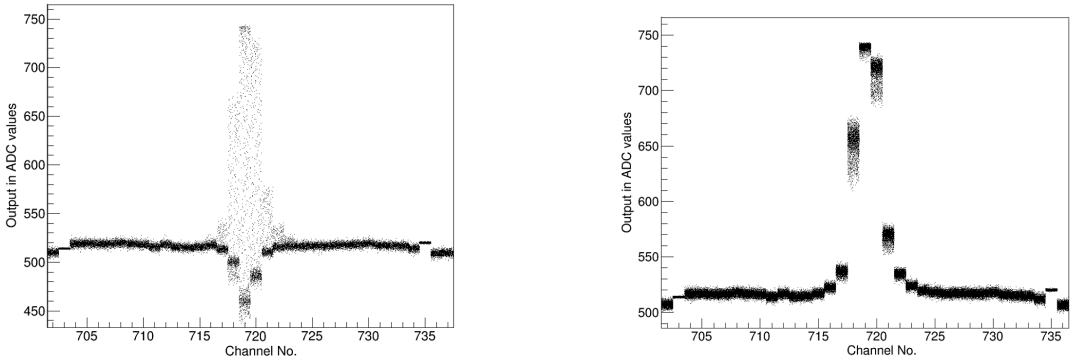

(a) Non-synchronised readout between the LD-1060 and VELO R-sensor.

(b) Synchronised readout between the LD-1060 and VELO R-sensor.

Figure 4.13 – Without synchronisation, the output pulse is sampled at random points (even negative points), decreasing the signal quality significantly.

To test the implemented change, a pulsed infra-red Laser Diode (LD-1060) with a peak wavelength of 1060 nm was used to mimic proton beam bunches generated by a cyclotron. In Fig. 4.13, the comparison between non-synchronised readout and synchronised readout with the laser and one VELO R-sensor is shown. During the non-synchronised readout, the front end pulse is sampled at random points by the Beetle chips. This results into a big spread of the ADC values as seen in Fig. 4.13a. The pedestals (signal response without the laser) are approximately 512 ADCs, equal to half of the available range for the data. A large amount of points are below that pedestal value, which means the output pulse is sampled at a negative point, decreasing the signal quality significantly. In Fig. 4.13b, the ADC values per channel show a much more finite spread and are above the pedestal value, since they are sampled at the peak region of the output pulse maximising the value of the laser signal. Moreover, the integrated ADC count values with their corresponding standard deviations are shown in Tab. 4.2 for the laser Peak-to-Peak voltages from 0.8 V to 1 V. To extract the signal, a noise filter (pedestal value) was applied. The synchronised readout signal in ADC counts is increased by an average of 2.86 times, whereas the average standard deviation for the non-synchronised readout is 5.9% and therefore almost 20 times worse than the average standard deviation of 0.3% for the synchronised readout.

Table 4.2 – Integrated ADC count values with standard deviation for different Peak-to-peak Voltages V_{pp} for the non-synchronised readout and synchronised readout with the pulsed LD-1060.

V_{pp}	**0.8 V**	**0.9 V**	**1 V**
Synchronised	1275984	1863959.3	2164706
Output [ADC]	($\pm$0.42%)	($\pm$0.27%)	($\pm$0.22%)
Non-synchronised	323840.7	751709.7	997398.3
Output [ADC]	($\pm$2.5%)	($\pm$9.2%)	($\pm$6.1%)

4.2.4 Post-processing software platform

After digitisation of the non-zero suppressed data from the VELO detector modules in the TELL1 boards, the data is sent to the data acquisition desktop PC for further post processing. In [10], the recorded data from the preliminary run in the eye proton beamline of the CCC was analysed offline and no online software tools were available. In order to decode, reformat and process the data, the Vetra application is used [107], originally developed as the main monitoring and parameter tuning tool for laboratory testing, commissioning and beam operation of the LHCb VELO detector modules. Tuned for handling the LHC proton-proton collisions data, the Vetra software had to undergo highly non-trivial customisation procedures to be able to process the medical beam experimental data. The changes of the Vetra software were developed by Dr. Tomasz Szumlak, AGH, Poland and are described in the following.

Raw data processing

The output data stream is divided into separate volumes corresponding to each sensor present in the setup and is stored in an optimised persistent binary format (so called MDF file). The NZS data, for each sensor, consists of 2048 numbers that represent digitised raw signals which, in turn, correspond to the 2048 physical channels on each sensor (see Fig. 4.14). In addition, so called, header data containing the chip diagnostic and monitoring information is also attached.

The Vetra processing pipeline is presented in Fig. 4.15. In the first step the binary data is read and respective data streams produced by each sensor are divided into

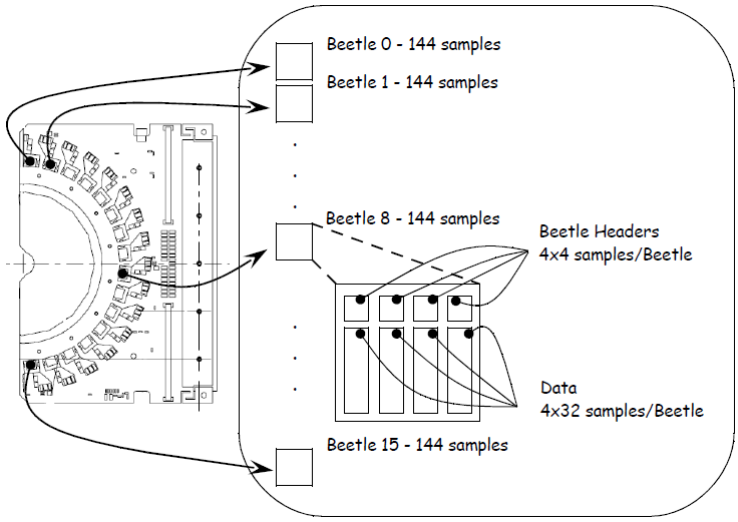

Figure 4.14 – Schematic representation of the NZS data stream produced by each VELO silicon sensor. The analogue signal is probed by the Beetle chips (each comprising 128 individual channels) and stored in an analogue pipeline implemented within chips. When a trigger signal is received, the analogue data is sent via long copper cables to the TELL1 boards for digitisation and processing. The digital resolution of the ADC is 10 bit.

fragments called events and packed into a structure called raw NZS bank and saved into the dynamic memory. Each such event contains the data from every active sensor. The raw banks are subsequently decoded into vectors of size 2048 of values representing ADC counts recorded on each strip. In Fig. 4.16 the raw decoded data are shown. The variations in behaviour of groups of 32 channels (one analogue link) are clearly visible.

Decoded data is processed at the next step by an algorithm, which attempts to evaluate the pedestal (offset) value for each individual readout channel. Digitised signals are in the range of 0-1023 ADC counts, whereas the baseline of the digitised output is around 512 ADC counts. The pedestal subtraction accounts for chip-to-chip and link-to-link variations and compensates their time variation to achieve a more uniform distribution. Typically it is required to collect at least 4000 events to get the stable pedestal values (see Fig. 4.17). After converging, the pedestal following phase of the algorithm is deactivated and the subtraction becomes active. The pedestal subtracted data (see Fig. 4.18) should be centred exactly at zero in case the signal is not present (noise data).

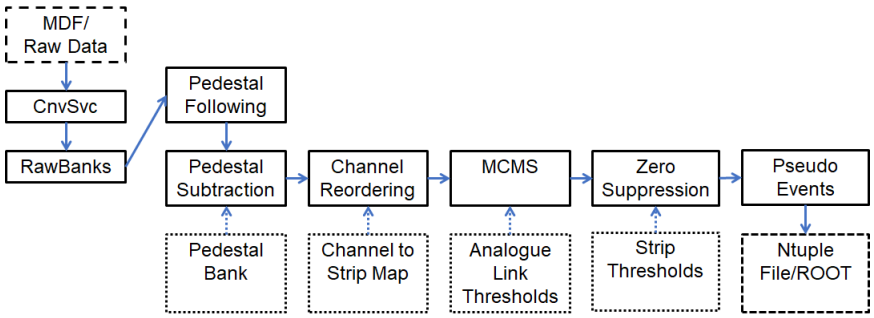

Figure 4.15 – Schematic representation of the raw NZS data processing pipeline. The solid rectangles represent algorithms. Pedestal bank and respective thresholds parameters are determined during special calibration runs.

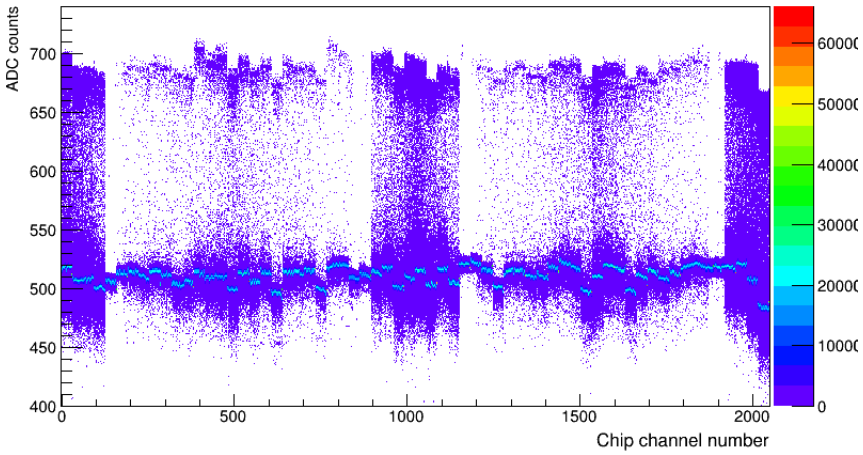

Figure 4.16 – Raw NZS data plotted as a function of readout chip channel. Apart from the offset (pedestal) there is a clear variation between analogue links (groups of 32 consecutive channels).

The VELO sensors feature a complicated topology of strips. Data registered on channels of both PHI- and R-type sensors is scrambled in order to optimise the analogue data transport protocol. This results in a difference between chip channel number and strip number (the latter pertaining to the physical strip position on the sensor). In order to translate the chip channels into the strips a special reordering algorithm is executed next, which implements appropriate mappings for both types of sensors.

The further step of processing attempts is to evaluate the residual shift (common mode noise) of the baseline and remove it. It was decided to use a simple Mean

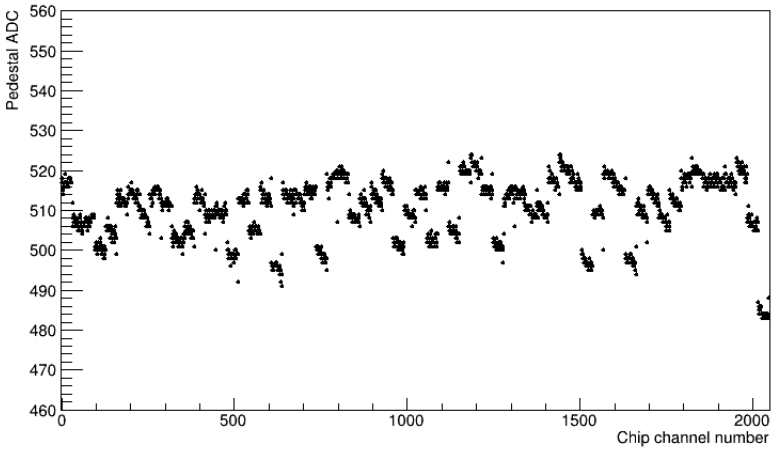

Figure 4.17 – Pedestal bank evaluated for a selected sensor at the following (training) phase. After converging the following algorithm is deactivated and the pedestals become fixed and are subtracted from all subsequent events.

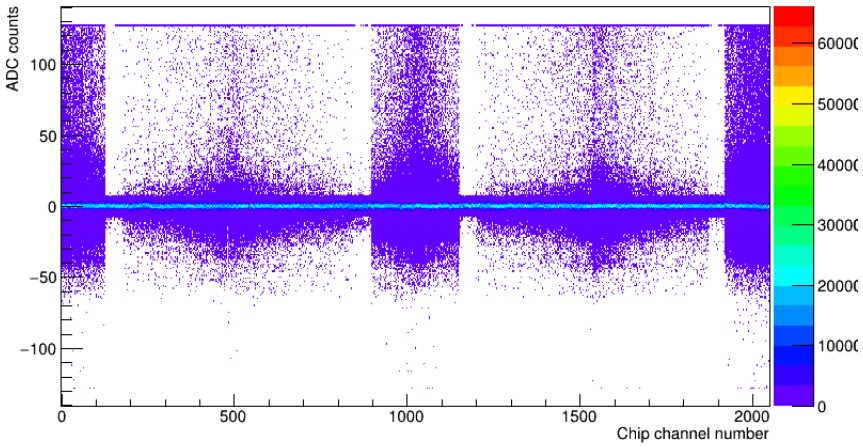

Figure 4.18 – Raw NZS data after pedestal subtraction. Both the offset and the initial variation between analogue links are removed.

Common Mode (MCM) algorithm that fits a flat line (a single parameter model) to the pedestal subtracted data. The algorithm performance critically depends on the hit detection threshold that is tuned for each analogue link separately. The channels with high ADC counts are removed from the MCM shift calculation. The final stage of the raw data processing is zero suppression that reduces significantly the volume of the data that is saved on the disk. The algorithm applies a single

threshold to the common mode corrected data which suppresses all the channels with the low ADC count. The thresholds are evaluated separately for each readout channel during the calibration procedure using the noise.

Since it was not possible to implement the entire LHCb VELO DAQ chain in the test setup, the final event building and reformatting had to be done in the high level software. For this purpose a dedicated algorithm has been implemented for pseudo-event building and data persistence. For convenience the processed hits were stored in the ROOT NTuple format. Each hit was saved in a data frame along with trigger specific information that was necessary for hit association and space points reconstruction (correlation of the R- and PHI-type hits for respective modules).

Analysis framework

The analysis software was prepared as a flexible and modular platform to allow easy extension of its functionality and modification of the input data format. The core part is built using generic services that are initialised, configured and handled by a single application manager object. The architecture of this mini-framework is shown in Fig. 4.19. There are three main services responsible for the following tasks: defining and handling the input and output data streams (I/OSvc), events processing (ProcSvc) and visualisation (VisSvc).

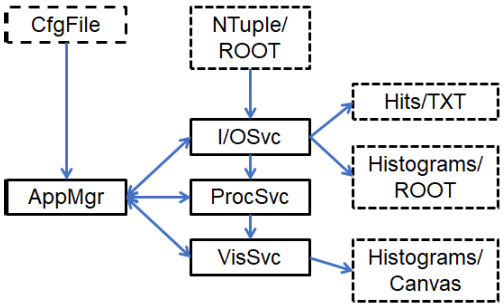

Figure 4.19 – Architecture of the analysis mini-framework for the test beam data analysis. The output data can be stored as ROOT histograms and the reconstructed hits and trigger information is saved as a formatted text file.

The I/OSvc takes as the input the location of a NTuple file on the disk. If the location is valid, a basic check regarding the file content and integrity is performed

and a pointer to a TTree object is initialised and passed to the processing module. Next, the ProcSvc defines the main processing sequence based on the configuration parameters sent by the application manager, e.g. the number of events to process and a data structure corresponding to the pseudo-event format is filled using the data stored in the TTree object. This structure acts also as an interface that abstracts the input data stream and makes the re-processing of the raw experimental data more convenient. Even if the pseudo-event format changes, e.g. more features are needed for the analysis, the code will still be backward compatible. All variables necessary for the data analysis are evaluated at this point. If requested, the VisSvc prepares histograms for the selected quantities, e.g. the pedestal corrected data or hit distributions on a single R- or PHI-sensor and either stores them in the output file or presents them to the user. Since the experimental setup comprised only two VELO modules, it was not possible to run the standard pattern recognition algorithms for hit correlation and space hits reconstruction. This part was done by a separate Matlab software. The input for the 3D space point reconstruction was prepared by the I/OSvc as a plain text file containing information regarding both R- and PHI-type hits and trigger data.

4.3 Summary

In this chapter, the LHCb VELO detector modules were described and the technology transfer from the LHC environment to a stand-alone system was presented. The characteristics of the silicon semiconductor sensor are described by the two sensor types, the R-sensor and PHI-sensor. The strip geometry enables a precise readout in polar coordinates. The most important readout electronics consist of the Beetle chips, sampling the output signal at 40 MHz and the TELL1 boards, sending out the readout triggers and are responsible for the timing control. Necessary changes for an operation outside the LHC environment were identified. To adapt the detector modules to a stand-alone system, several developments were presented. This included the development of a venting and cooling system for safe operation in air. A positioning system was developed for a secure and precise handling of the modules. Several adaptations to the electronics led to a new way to synchronise the readout of the VELO detector modules with the proton bunch arrival and a second instrument. The readout and analysis software was updated and several new features were implemented to achieve quasi online beam monitoring. To conclude, all unique features for the LHC environment have been replaced and adapted, thus a full setup, optimised for the implementation in a proton beamline, is presented. All stated requirements were fulfilled successfully. Challenges in [10] regarding the readout synchronisation and data post-processing were addressed and newly developed systems are in place.

5 Implementation of the LHCb VELO detector modules at the MC40 proton beamline at the University of Birmingham

5.1 Setup of the VELO detector modules at the MC40 proton beamline

The VELO detector modules were characterised using the MC40 cyclotron proton beamline at the University of Birmingham. The research facility was used for five days (two setup days and three measurement days), thus comprehensive tests with the stand-alone system were possible. The cyclotron is equipped with a switching magnet, which extracts the beam in two main beamlines (see Fig. 5.1) [47].

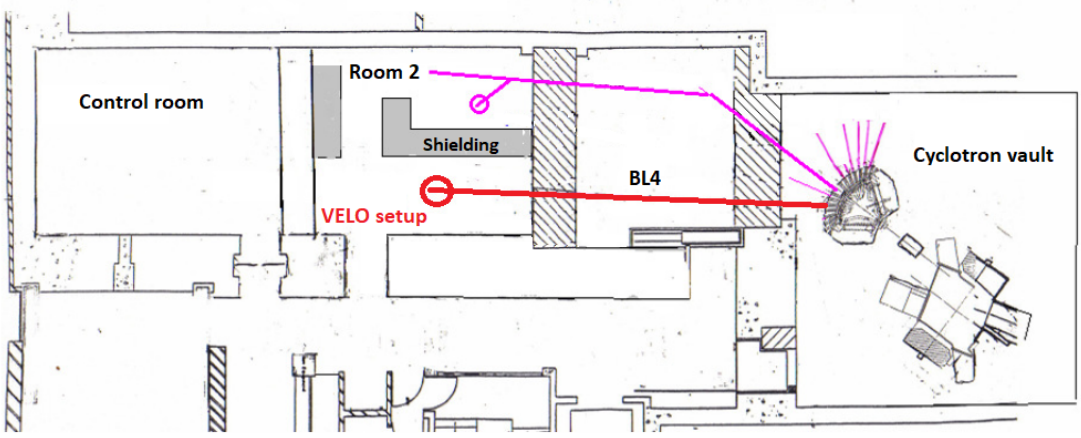

Figure 5.1 – Layout of the irradiation facility at the University of Birmingham, featuring the cyclotron vault, the high intensity irradiation area and the operator control room. The stand-alone setup of the VELO detector modules was built up in the room marked "VELO setup", where the beamline 4 (red line) leads to. Modified after [47].

The stand-alone setup of the VELO detector modules were built up in the room marked for "VELO setup" (see Figs. 5.1 and 5.2). To align the detector modules to the beam centre, a laser was mounted on top of the switching magnet projecting a vertical laser line. Further, the VELO detector modules were placed on a metal bottom base plate for a secure and level stand in the axis perpendicular to the beam.

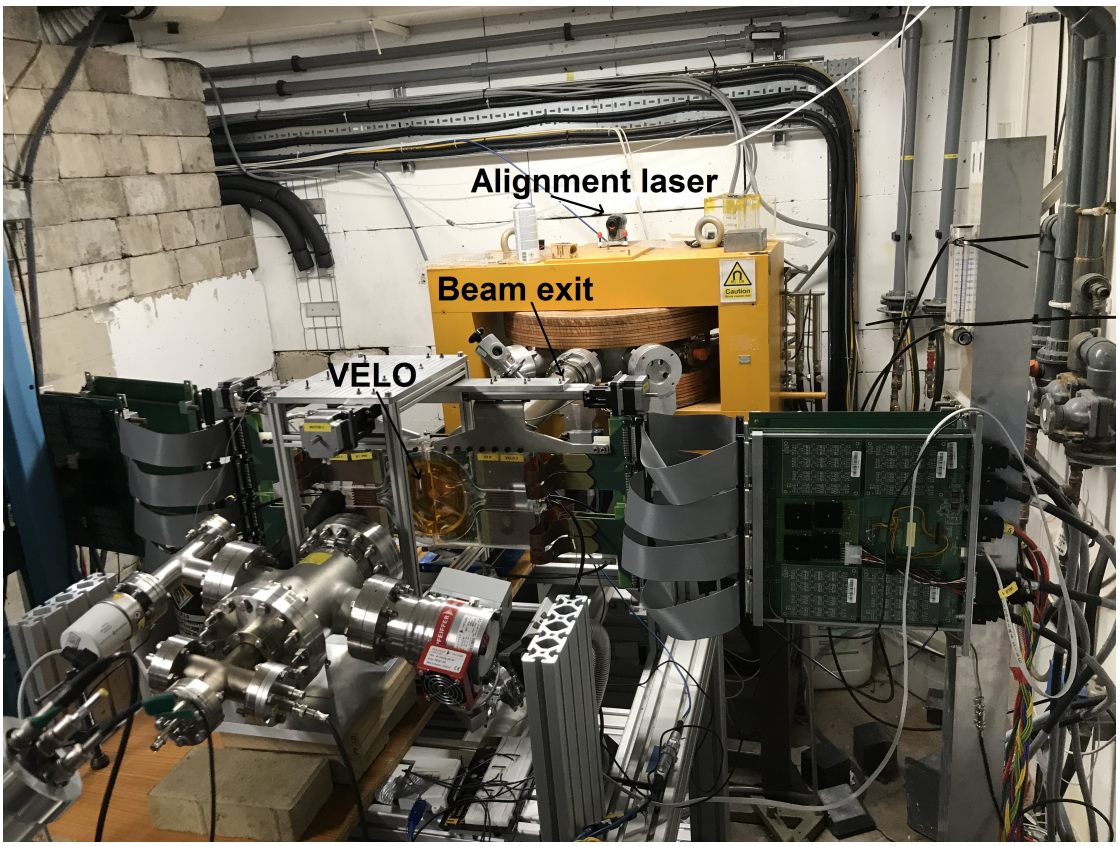

Figure 5.2 – Setup of the VELO detector modules in the irradiation room. On top of the switching magnet, a laser was mounted to align the detector modules with the nozzle pipe, where the beam exits.

5.1.1 Requirements and aims for the irradiation study

The VELO hardware and electronics were specifically changed to match the readout of the VELO detector modules with proton bunch arrival by the RF frequency of the MC40 cyclotron. The changes were described in the previous section 4.2.3 [108]. To correspond the readout signal of the VELO detector modules to the beam current, the in-beam ionisation chamber Type 7862, PTW, read out by the UNIDOSE E electrometer, PTW, was used. The ion-chamber is set up behind the scattering foil and a 50 mm collimator within the beamline. A software trigger to start and stop the readout of both detectors simultaneously was adapted and successfully implemented. Further, the ionisation chamber was used to monitor the beam current during data acquisition.
The schematic of the readout system is shown in Fig. 5.3.

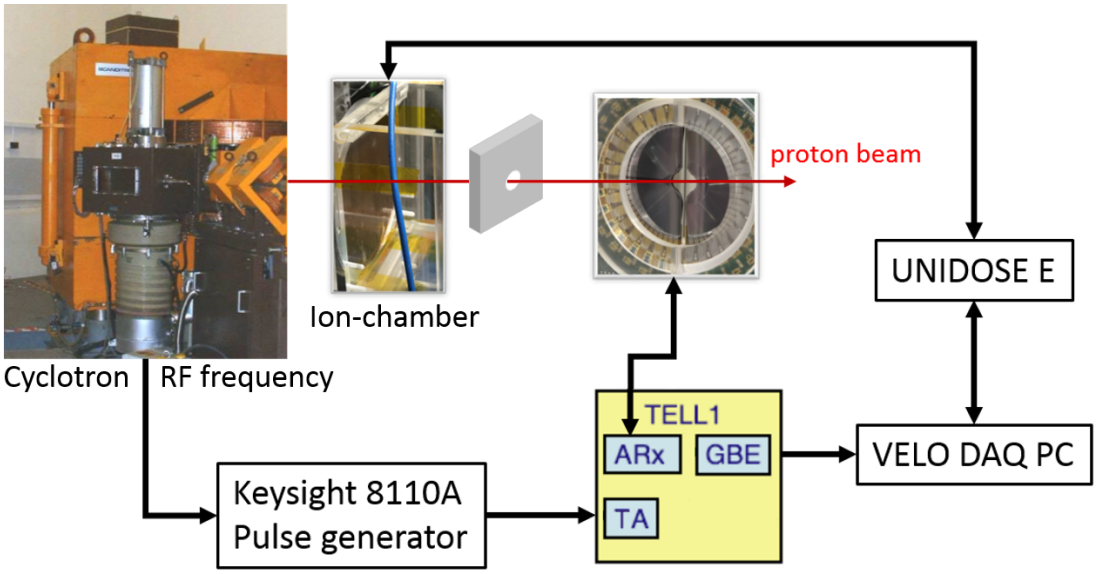

Figure 5.3 – Synchronisation of the readout of the VELO detector and in-beam ion-chamber. A developed software trigger controls the simultaneous data acquisition of the VELO detector and the ion-chamber. The RF frequency of the cyclotron triggers the pulse generator, which injects readout triggers into the TELL1 board.

The main goals of the study are summarised in the following:

1. Application and verification of the introduced changes for a synchronised readout described in the previous section 4.2.3 and in [108].
2. Characterisation of the response of the VELO detector modules to changes of the beam current.
3. Acquisition and characterisation of profiles of the proton beam for different sizes of the beam.
4. Combining the results of the beam current and profile measurements to develop a Halo to Dose correlation for the VELO detector modules.

For the experiment, two VELO detector modules, each consisting of one R- and PHI-sensor, were used. The used terminology for future references is: R1 and PHI1 are the sensors for module 1, positioned on the right side in reference to the proton beam propagation out of the collimator (see Fig. 5.2). R2 and PHI2 are the sensors for module 2, positioned on the left side in reference to the proton beam propagation out of the collimator.

5.2 Results

During the three-day measurement campaign, the following cyclotron settings and positions of the VELO detector modules were used to perform beam current and profile measurements:

Table 5.1 – Summary of the different settings of the cyclotron.

	Day 1	**Day 2**	**Day 3**
Energy	28 MeV	18 MeV	18 MeV
RF frequency	22 MHz	18.21 MHz	18.21 MHz
Diameter of collimator	1 mm - 20 mm	7 mm, 10 mm, 15 mm	7 mm, 10 mm, 15 mm
Beam current	1 nA	0.5 nA - 6 nA	0.2 nA - 3 nA

The VELO detector modules were located 16.8 cm away from the collimator exit. The change of the proton energy from day 1 to day 2 was necessary, since the pulse generator can only accept frequencies up to 20 MHz as external triggers.
From day 2 to day 3, the scattering foil holder within the beam line was damaged. Consequently, the scattering foil had to be removed and the ion-chamber had to be repositioned behind the collimator exit in front of the VELO modules. Further, the size of the proton beam had to be controlled by changing the settings of the magnets.

5.2.1 Preliminary beam parameter consideration

The ultimate goal of the studies is to derive a relationship of the proton beam halo measured by the VELO detector modules and the delivered dose. This requires a correlation between the output of the VELO detector modules and the different collimator sizes. Within the beamline, the proton beam goes through the ionisation chamber with a diameter of 50 mm. Each proton produces 160 electrons inside the ion-chamber. The beam current is calculated for a given number of protons per second:

$$I_{beam} = \frac{N_{pIC} \times e}{160} \quad \left[\frac{C}{s}\right] \tag{5.1}$$

With the electric charge of a proton $e = 1.6022 \times 10^{-19}$ C and N_{pIC} is the number of protons travelling through the ionisation chamber.

The number of protons out of the collimator N_{pColl} can be derived out of the ratio of the area between the collimator A_{Coll} and the ionisation chamber A_{IC}:

$$N_{pColl} = N_{pIC} \times \frac{A_{Coll}}{A_{IC}} \tag{5.2}$$

$$N_{pColl} = N_{pIC} \times \frac{(\frac{d_{Coll}}{2})^2}{25mm^2}, \tag{5.3}$$

where d_{Coll} is the diameter of the collimator.
Therefore, a first correction factor is determined as the area factor k_{area} resulting from Eq. 5.3 and the smallest used collimator diameter of 7 mm.

$$k_{area} = \frac{A_{Coll}}{A_{7mm}} \tag{5.4}$$

The second factor k_{norm} is implementing the area below the normal distribution curve of the proton beam profile. The VELO sensors are only interacting with a fraction of the beam, thus it cannot be disregarded. For larger collimator sizes, the number of protons interacting with the VELO detector out of all protons will increase exponentially. The correction factor k_{norm} is defined as the ratio between the determined percentages of a collimator diameter p_{coll} and the percentage of the collimator diameter of 7 mm.

$$k_{norm} = \frac{p_{coll}}{p_{7mm}} \tag{5.5}$$

To determine the scale of the factors, GEometry ANd Tracking 4 (GEANT4) simulations of the MC40 proton beamline are performed. The beamline model and the scripts were provided by Dr. Tony Price, University of Birmingham, UK and were performed by Jacinta Yap, University of Liverpool, UK. The entries were saved in a text file for further analysis. Beam profiles for collimator diameters of 7 mm, 10 mm, 15 mm and 20 mm were generated. The absorber of the 18 MeV protons in the simulation was chosen to be EBT3 GAFchromic film. Due to the high computing time of 15 hours, a maximum number of 10^8 protons were used to generate the profiles. This corresponds to a beam current of around 0.40 nA. The distribution of the simulated entries for film in one dimension is fitted with the probability density of the normal distribution:

$$F(x) = \frac{1}{\sigma\sqrt{2\pi}} e^{-(x-\mu)^2/2\sigma^2} \tag{5.6}$$

With μ as the mean, σ as the standard deviation and σ^2 as the variance.

To illustrate the differences in the area for the different collimators, Fig. 5.4 compares the fitted normal distribution to the simulated entries for film. The two dashed lines at x=-8 mm and x=8 mm represent the aperture opening of the VELO detector modules. The Full Width Half Maximum (FWHM, 2.35σ) is shown in Tab. 5.2.

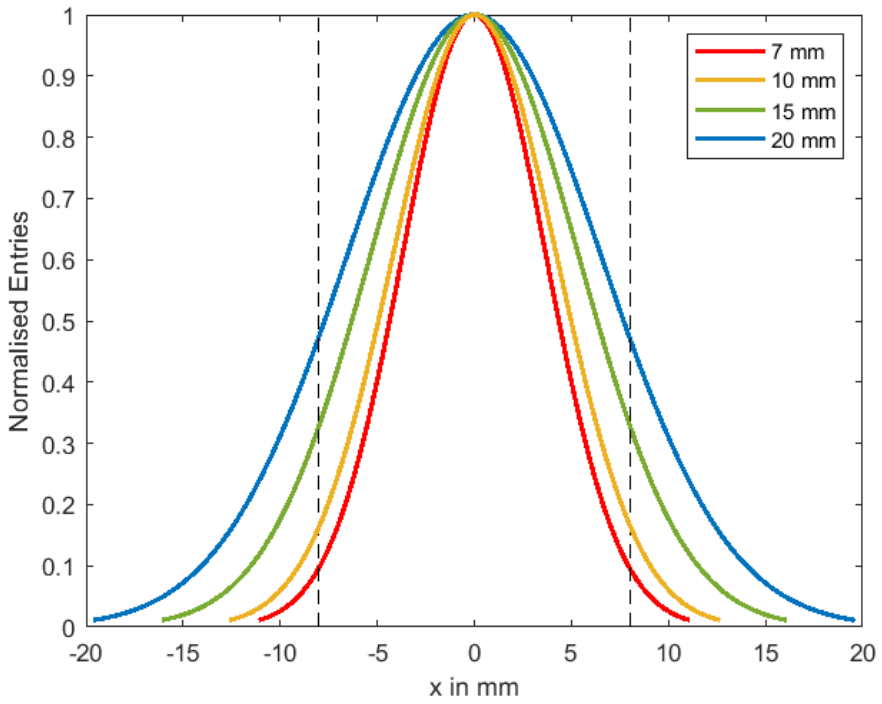

Figure 5.4 – Comparison of the fitted entries of protons in EBT3 GAFchromic film relative to the x-axis for the different collimator diameters. The two dashed lines at x=-8 mm and x=8 mm represent the aperture opening of the VELO detector modules.

The percentage of protons interacting with the VELO detector modules is determined by the cumulative distribution function of the normal distribution Eq. 5.6:

$$p(x) = \int F(x)\mathrm{d}x = \frac{1}{\sigma\sqrt{2\pi}} \int_{-\infty}^{z} e^{-(x-\mu)^2/2\sigma^2}\mathrm{d}x \tag{5.7}$$

To solve the integral the complementary error function is used:

$$p(x) = \frac{1}{2}\mathrm{erfc}\left(\frac{-x}{\sqrt{2}}\right) \tag{5.8}$$

The complementary error function is:

$$\mathrm{erfc}(x) = 1 - \mathrm{erf}(x) = \frac{-x}{\sqrt{2}} \int_{z}^{\infty} e^{-t^2}\mathrm{d}t \tag{5.9}$$

For the four collimator sizes, the following percentages were determined in Tab. 5.2 with Matlab utilising Eq. 5.9.

Table 5.2 – FWHM, Percentage % of the entries larger than 8 mm for different collimator sizes and k_{norm}.

Collimator diameter [mm]	7	10	15	20
FHWM [mm]	8.72	9.93	12.64	15.40
Percentage [%]	6.30	7.92	13.31	22.15
Correction factor k_{norm}	1	1.257	2.113	3.516

The final correction factor k_{corr} for the entries in dependence of the 7 mm collimator reads:

$$k_{corr} = k_{area} \times k_{norm} = \frac{(\frac{d_{Coll}}{2})^2 \cdot p_{coll}}{3.5^2 \cdot 0.063} \tag{5.10}$$

To test the formula, entries for x $>$ 8 mm and x $<$ -8 mm are determined from 10^5 to 10^8 protons for the different collimator sizes. The entries are fitted linearly and the result is shown in Fig. 5.5. The gradients of the linear function for the different collimators are determined and the ratios with the gradient of the 7 mm collimator are calculated. The ratios are compared to the correction factors calculated by Eq. 5.10. The values are summarised in Tab. 5.3.

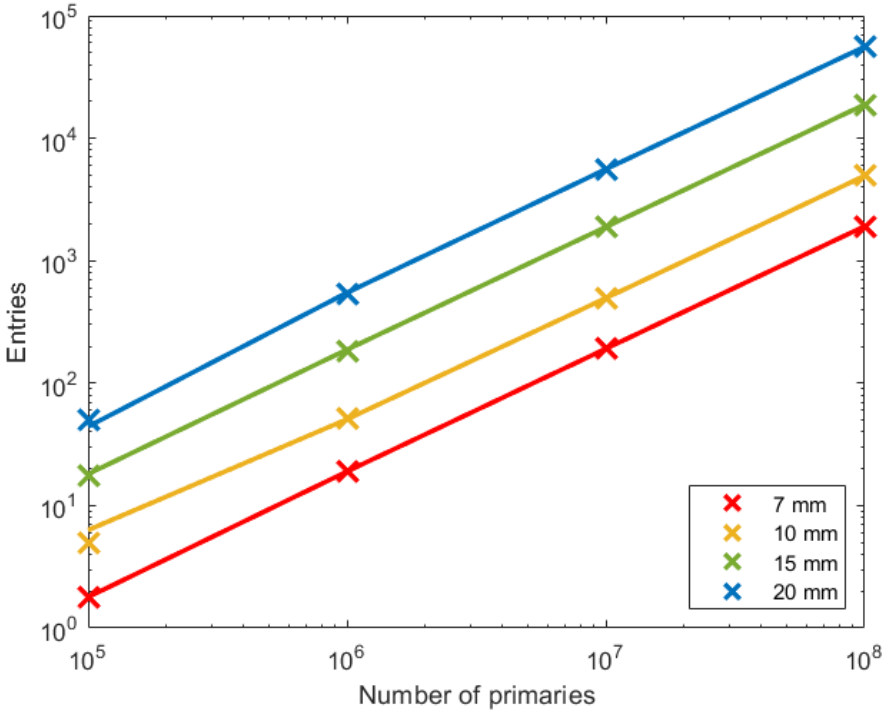

Figure 5.5 – Entries for x > 8 mm and x < −8 *mm* related to the total number of protons and fitted linearly for different collimator sizes.

Table 5.3 – **Comparison of the ratios between the gradients of the linear fit (Fig. 5.5) of different collimator sizes to the 7 mm collimator to the calculated correction factors based on Eq. 5.10.**

Collimator diameter [mm]	**Gradient** $[10^{-5}]$	**Ratio**	**Correction factor** k_{corr}
7	1.9103	1	1
10	4.9288	2.580	2.566
15	18.841	9.863	9.703
20	55.927	29.276	29.276

The calculated ratios and the correction factors agree with each other very well. Therefore, the correction factor of Eq. 5.10 will be applied for the measured results of the VELO detector modules.

5.2.2 Impact of proton irradiation on the VELO detector modules

Saturation of the detector modules

In the LHCb experiment, the VELO detector modules were specifically designed to resolve Minimum Ionising Particles (MIPs) like pions. The energy loss of a MIP in matter is the minimum loss predicted by the Bethe-Bloch-formula. The electron-hole pair generation follows a straggling function best described by a Landau convolved with a Gaussian [109]. According to [109], a pion interacting with 300 µm silicon produces around 22,000 electron-hole pairs. The ionisation energy of 3.6 eV creates one electron-hole pair in silicon, thus the energy loss per µm is 264 $\frac{\text{eV}}{\mu\text{m}}$ and the total energy loss is 79.2 keV. This corresponds to a stopping power of 1.14 $\frac{\text{MeV cm}^2}{\text{g}}$.

In contrast, during the measurements, protons with energies of 28 MeV and 18 MeV were used. According to [110], the proton stopping power in silicon is 21.94 $\frac{\text{MeV cm}^2}{\text{g}}$ for an energy of 18 MeV and 15.51 $\frac{\text{MeV cm}^2}{\text{g}}$ for an energy of 28 MeV. Using the 18 MeV protons as an example, the total energy loss of one proton in the 300 µm silicon of the VELO detector modules is 1.53 MeV, which is more than 19 times higher than the energy loss of a MIP. This corresponds to a creation of 425,000 electron-hole pairs.
When counting particles during the LHCb experiment, a signal is expressed in ADC counts. The noise in each strip channel is typically around 1-3 ADC counts. 15 ADC counts, 5 times higher than the noise signal, is set as a threshold for particle detection. The most probable value for the detected MIP is around 45 ADC counts. Thus, a proton would correspond to a signal of more than 850 ADC counts, well above the detectable limit of 127 ADC counts.

As an example, the distribution of ADC counts of one R1-sensor data set is shown in Fig. 5.6. Using a 7 mm collimator and a proton beam current of 0.06 nA, this current and collimator was one of the lowest setting used during the runs. As predicted, when the R-sensor is detecting a hit, the strip is saturated with an ADC count of 127. In Fig. 5.7, the average total ADC count per hit is calculated for each strip of the R- and PHI-sensor. The shown sum of the ratio for R and PHI is usually 2x127=254 and occurs across the entire sensor area. This means

one hit is saturating the strip, as no significant numbers of hits past r=17 mm are expected.

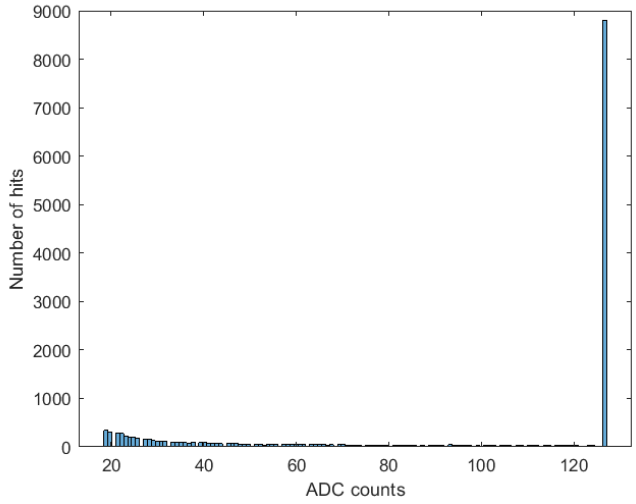

Figure 5.6 – Histogram of the distribution of ADC counts of the R1-sensor of one data set. A 7 mm collimator with a proton beam current of 0.06 nA was used.

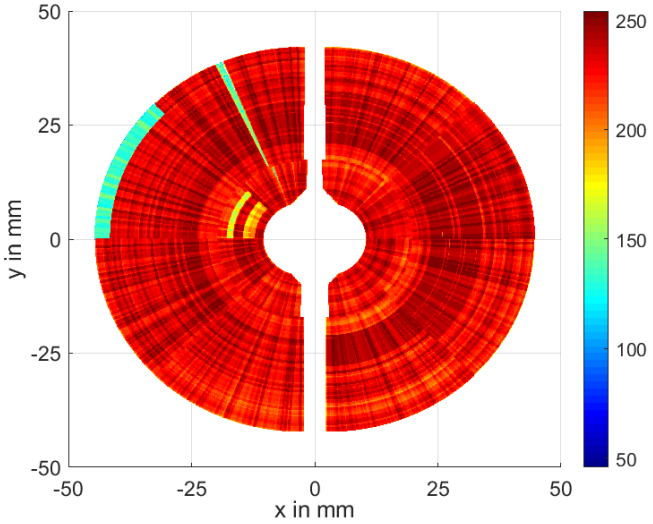

Figure 5.7 – Image of the two modules for a 7 mm collimator. It shows the total ADC counts per registered hits summed up for the R- and PHI-sensor. The detector modules are saturated.

VELO strip and chip channel spill-over and clustering

Besides the clear peak of 127 ADC counts in Fig. 5.6, a small number of hits with ADC counts below the saturation value is counted. To address these, a closer look at the data collection file for the run with the 7 mm collimator is taken (see Tab. 5.4). Two events have been extracted, which show the registered hits with the corresponding ADC counts of the R2-sensor and of the PHI1-sensor.

Table 5.4 – Extract of the data collection file of a run with a 7 mm collimator. The registered hits are shown for two events for the R2-sensor and the PHI1-sensor.

Event	Sensor	Strip	Channel	ADC
17044	R2	1233	942	40
17044	R2	1234	941	121
17044	R2	1235	940	127
17044	R2	1236	939	41
78627	PHI1	171	1533	37
78627	PHI1	173	1528	127
78627	PHI1	176	1517	127
78627	PHI1	992	1583	127
78627	PHI1	1026	1532	127
78627	PHI1	1028	1530	43
78627	PHI1	1036	1518	34
78627	PHI1	1039	1514	28

For the first event example 17044, the R2-sensor registered four hits at the adjacent strips 1233-1236. As only strip 1235 registered the maximum ADC count of 127, the high ionisation charge of one particle induces a signal in the rest of the four strips.

For the second event example 78627, the PHI1-sensor registered eight hits. The first three hits are located in the inner PHI-sector (strips 0-683), whereas the others are located in the outer PHI-sector (strips 684-2047). Due to the scheme with which sensor strips are bonded to the readout chips, adjacent strips are not connected to consecutive Beetle chips channels. Especially in the PHI-sensor, inner and outer strips are mixed in the analogue links. Hence, every strip has a certain Beetle chip channel. The corresponding chip channel numbers for this event are

relatively close together in one group, indicating a cross-talk between the channels due to the large signal. However the possibility is still given that more than one particle is detected.

As a conclusion of this section, using ADC counts to characterise the beam has to be disregarded due to very high saturation levels. Therefore, only hits, the amount of times a strip registered a signal, are counted. To reduce the number of hits caused by one proton, a new spill-over and clusterisation algorithm was implemented and performed after the Vetra processing. At first, every signal below the ADC count of 127 is disregarded. Further, hits on the same strips in subsequent triggers (spill-over) for each sensor are identified and cleaned. The clusterisation algorithm will group the seeding strip or channel with up to three additional adjacent strips or channels together.
Table 5.5 shows an example of the algorithm for the 15 mm collimator with a beam current of 1 nA.

Table 5.5 – Reduction of hits (H) by the spill-over (H_{SO}) and clustering (H_{Clst}) algorithm for the 15 mm collimator with a beam current of 1 nA for each sensor. The relative difference $D_{SO} = H_{SO}/H$ and $D_{Clst} = H_{Clst}/H$ is also shown.

	R1	**PHI1**	**R2**	**PHI2**
H	$40145 \pm 0.97\%$	$36096.8 \pm 0.65\%$	$66583.2 \pm 1.03\%$	$62077.2 \pm 0.93\%$
$\mathbf{H_{SO}}$	$39868.8 \pm 0.94\%$	$35923.8 \pm 0.66\%$	$65888.8 \pm 0.99\%$	$61641 \pm 0.94\%$
$\mathbf{H_{Clst}}$	$31357.2 \pm 0.98\%$	$32824.2 \pm 0.64\%$	$57292.2 \pm 1.08\%$	$59253.6 \pm 0.93\%$
$\mathbf{D_{SO}}$ [%]	0.69	0.48	1.04	0.70
$\mathbf{D_{Clst}}$ [%]	21.78	8.97	13.77	4.41

The spill-over plays only a minor role to reduce the hits, as the difference is just $\lesssim 1\%$. Module 1 shows a much higher reduction of hits by the clustering algorithm than module 2. Dead strips in sectors, where a low number of hits is expected and less clusters are formed, are skewing the total average across the whole sensor. After the applying the algorithm, the hits per event were reduced from 3.1 to 2.4 for the R1-sensor and from 4.2 to 4.0 for the PHI2-sensor.

5.2.3 Phase scan

The external triggers, controlling the VELO detector modules readout, were injected by the pulse generator synchronised by the 18.21 MHz (54.9 ns) RF frequency of the cyclotron. To optimise the proton bunch arrival time on the VELO detector modules and account cable delays within the setup, a phase scan over one RF frequency period was performed. The delay of the pulse generator was changed at steps of 7.5 ns first. If a signal peak was found, the step size was reduced to 2.5 ns around it. In Fig. 5.8, hits are summed up for the two modules and the delay for the highest signal output was found to be 22.5 ns. This setting was then used for the entire measurement day. The measurement has to be repeated every day after the routine maintenance and quality assurance of the accelerator in the morning or if the RF frequency dropped during the course of the day.

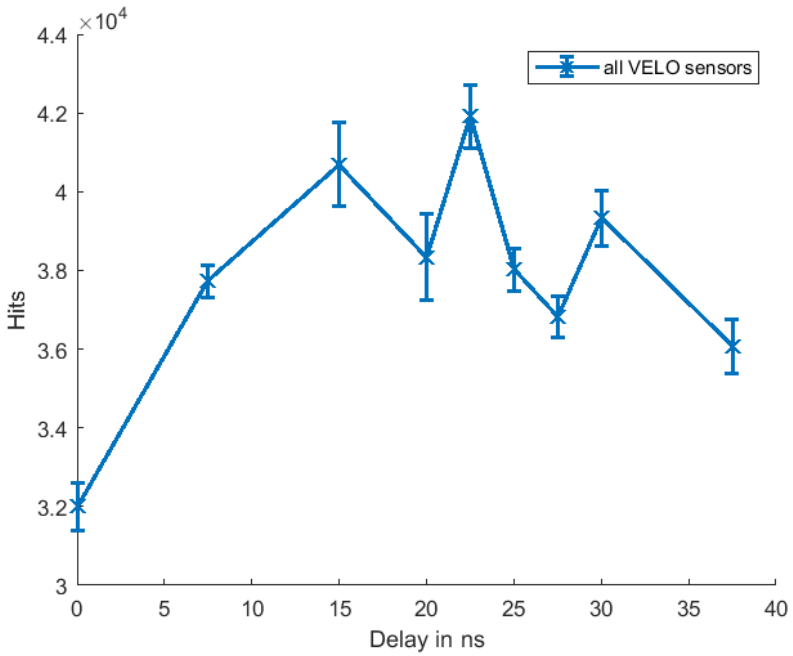

Figure 5.8 – Phase scan over the RF frequency period of 54.9 ns. At 22.5 ns, the highest amount of hits was recorded for all four sensors.

5.2.4 Beam current measurements

In the following, the VELO detector modules were used to monitor different beam currents for the collimators of 7 mm, 10 mm and 15 mm diameter. All collimator sizes are smaller than the aperture size of the VELO modules of 16 mm. Thus, the beam core is likely to pass through the aperture and mainly, the beam halo will be detected. The output of the VELO sensors were correlated to the absolute value of the charge reading (absolute charge) of the electrometer detected by the ion-chamber.

In Fig. 5.9, the results of the beam current measurement for the 15 mm collimator are shown. For each beam current setting, data collection was repeated five times. For each of those runs, the VELO detector modules collected 80k events, thus 20k events per sensor. The readout triggers were sent at a frequency of 1 kHz (1 ms), which results in a measurement time of 20 s per run.
The five runs were averaged and plotted. Comparing the sum of hits for the two modules in Fig. 5.9, the amount of hits of module 2 is larger than module 1. The reason is discussed in detail in the next section, where beam profile measurements are compared. The measured hits for different beam currents follow a clear linear trend. To evaluate the linear regression, the R^2-value is calculated as the ratio of the residual sum of squares S_{res} and the total sum of squares S_{tot}:

$$R^2 = 1 - \frac{S_{res}}{S_{tot}} = 1 - \frac{\sum(H - H_{fit})^2}{\sum(H - H_{mean})^2}, \tag{5.11}$$

where H is the number of hits, H_{fit} is the linear fitted number of hits and H_{mean} is the mean hit value.
For the four sensors, the calculated values are R^2_{R1}=0.996, R^2_{PHI1}=0.997, R^2_{R2}=0.994 and R^2_{PHI2}=0.995. Further, the standard deviation of the hits are shown in Tab. 5.6. The errors are very small for all four sensors, often times below 1%. Therefore, the output of the VELO detector modules is very consistent.

Table 5.6 – Relative standard deviation in % of the hits of the VELO sensors for different beam currents for a 15 mm collimator.

Absolute Charge [10^{-5}**C**]	0.2120	0.4121	0.8149	1.236	1.643	2.021
SD of R1 Hits [%]	1.04	0.98	0.54	0.80	0.89	0.85
SD of PHI1 Hits [%]	0.74	0.64	1.15	0.21	0.68	1.00
SD of R2 Hits [%]	0.95	1.08	0.88	0.61	0.73	1.38
SD of PHI2 Hits [%]	1.58	0.93	0.91	0.70	1.15	1.29

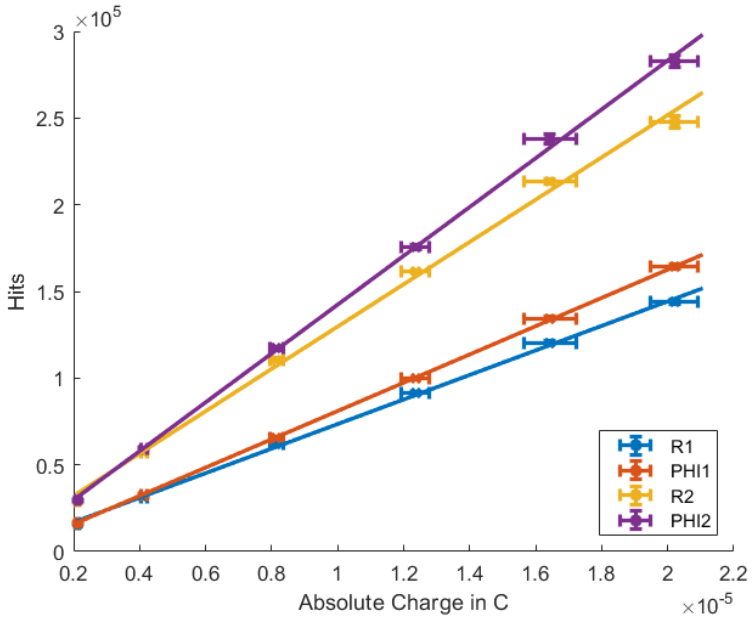

Figure 5.9 – Average hits of the VELO sensors per absolute charge measured by the electrometer using a 15 mm collimator.

However, the output of the electrometer contained larger fluctuations with the smallest standard deviation of 2.3% for the first setting and up to 4.76% for the fifth setting (see Tab. 5.6). To understand these deviations better, the five runs per beam current setting are shown in Fig. 5.10.

Table 5.7 – Uncorrected and time corrected relative standard deviation in % of the absolute charge measured by the electrometer for the 15 mm collimator.

Absolute Charge [10^{-5}**C**]	0.2120	0.4121	0.8149	1.236	1.643	2.021
SD (uncorrected) [%]	2.30	2.25	2.31	3.36	4.76	3.54
SD (corrected) [%]	0.64	0.24	0.56	0.31	4.63	1.00

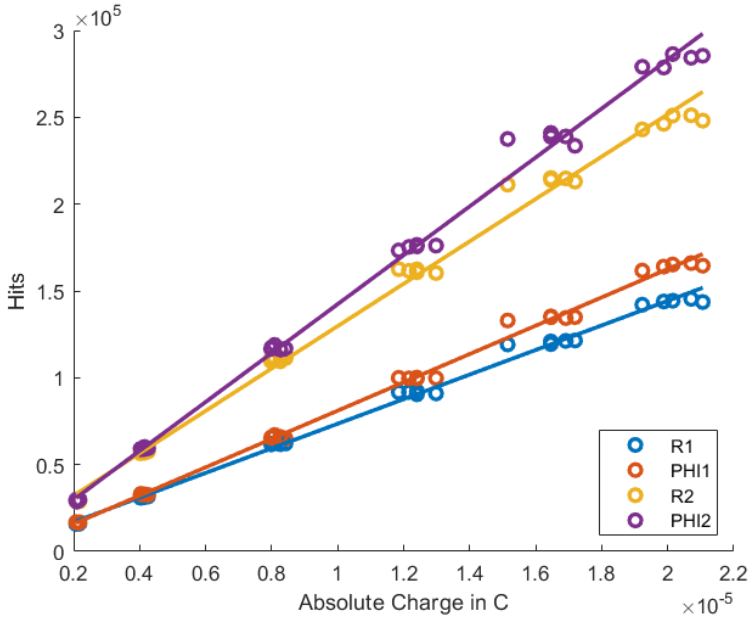

Figure 5.10 – Hits of the VELO sensors per absolute charge measured by the electrometer using a 15 mm collimator.

With increasing beam current, the collected charge values for each run show a slight spread for nearly constant hit values. There are two main sources of this uncertainty. Firstly, the electrometer integrates charge every 0.5 s. As a result for a 20 s run, the expected collection error is already at ±2.5%, which is the usual standard deviation observed in the data. Secondly, a software processing delay in the readout scripts was observed during data taking. The stop signal to finish the charge collection of the electrometer is sent out after the data collection of the VELO detector modules finishes. The completion process of the latter, usually a matter of few ms, took occasionally longer than 0.5 s due to the high occupancy of the PC hardware. Because of the different nature of the command languages to control the VELO detector modules and the electrometer and especially the age of

the VELO readout scripts of more than 10 years, a modification to optimise this process is not foreseeable.
However, a time correction factor for the charge collection can be introduced to account for this error. The correction factor will normalise the charge value to the readout time of 20 s and the results are shown in Fig. 5.11 and Fig. 5.12.

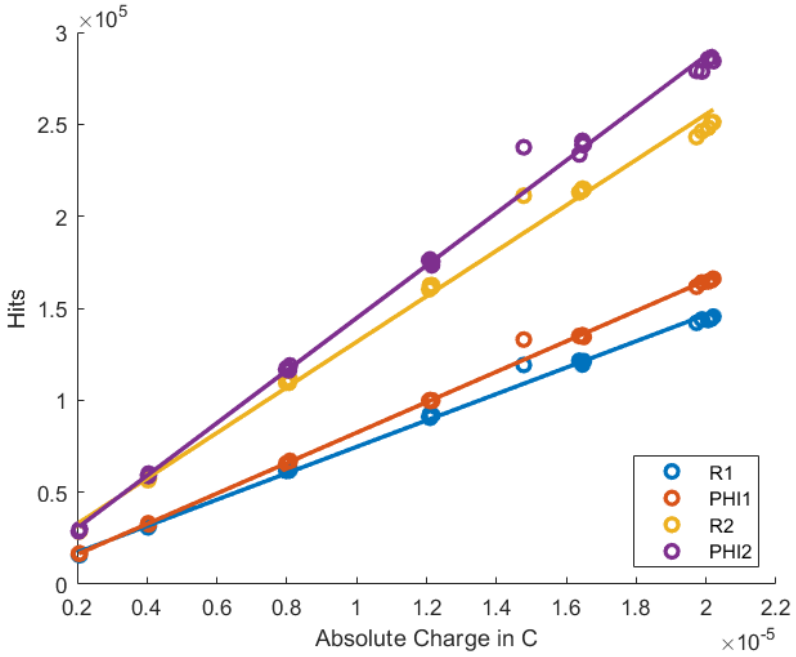

Figure 5.11 – Hits of the VELO sensors per corrected absolute charge measured by the electrometer using a 15 mm collimator.

Except for one outlier in the fifth run, the spread of the charge has been reduced. The standard deviation is 0.55% on average (see Tab. 5.6), almost five times lower than the usual observed error. This also increases the already excellent R^2-value from 0.995 on average for all four sensors to 0.997 for the corrected charge data.

The beam current measurements for the 15 mm showed a nearly perfect behaviour of the VELO detector modules. In the following, the results for the 10 mm collimator are shown in Fig. 5.13 and Fig. 5.14.

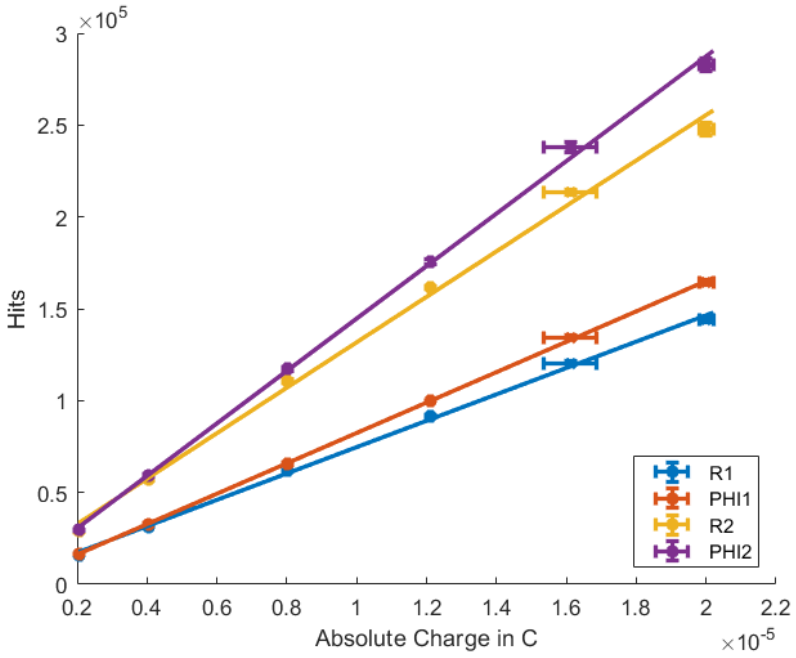

Figure 5.12 – Average hits of the VELO sensors per corrected absolute charge measured by the electrometer using a 15 mm collimator.

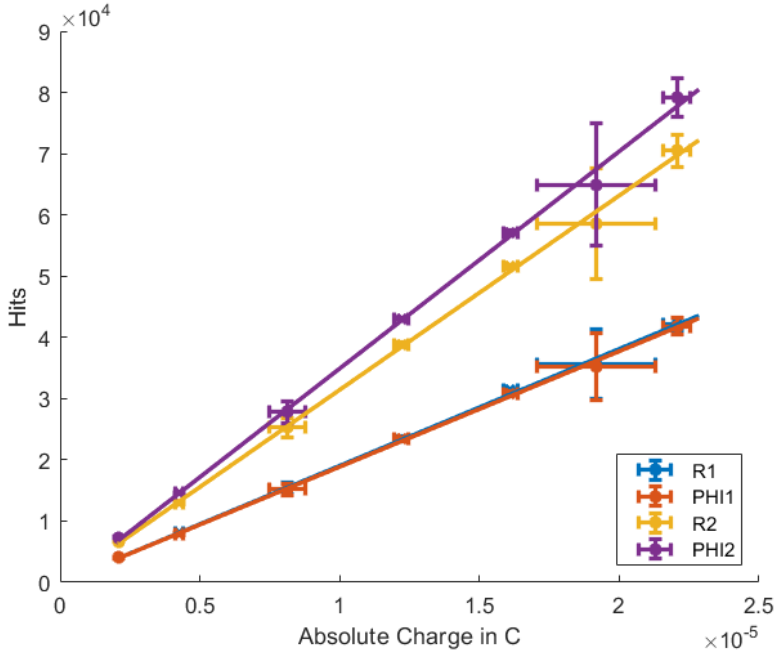

Figure 5.13 – Average hits of the VELO sensors per absolute charge measured by the electrometer using a 10 mm collimator.

In the third and sixth run in Fig. 5.13, exceptionally large error bars are observed for the hits for all VELO sensors. The standard deviation of the hits is 6.33% for the third run and 15.58% for the sixth. Similar large variations are observed for the measured charge and are 8.04% and 11.01% respectively. In Fig. 5.14, instead of three defined areas of five data points for the last three runs, a wide spread of hit and charge values in two areas is observed. This is the direct result of beam current fluctuations and RF drops caused by the cyclotron. However, the measured values are still following the linear trend as shown by the fitted curve. Therefore, the R^2-value is still very good with 0.996 on average for all sensors. Further, for runs without beam current fluctuations, the standard deviation is equal to beam current measurement with the 15 mm collimator of $\leqq 1\%$.

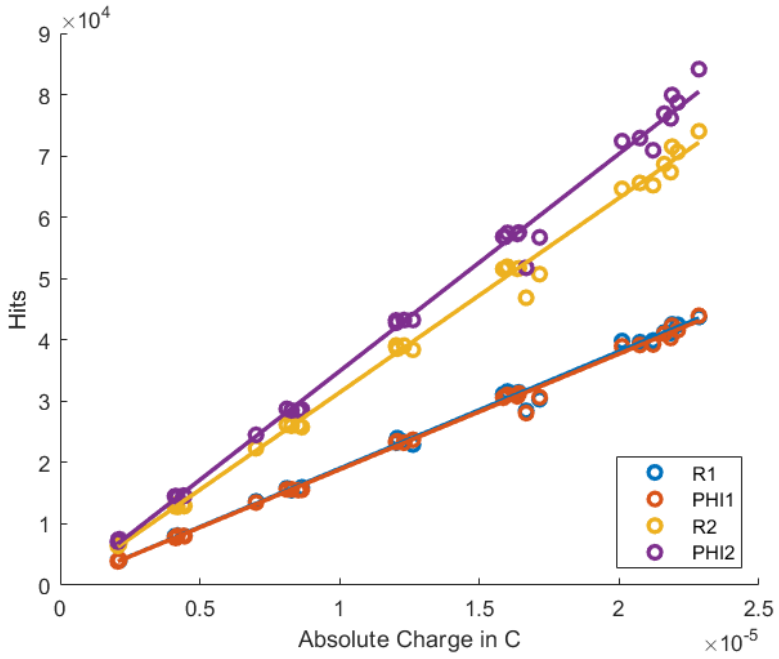

Figure 5.14 – Hits of the VELO sensors per absolute charge measured by the electrometer using a 10 mm collimator. Beam current fluctuations are observed during the last three runs.

The same effects of the charge collection uncertainty for the electrometer (run 1 and 4) and the beam current fluctuation (run 7) were observed for the beam current measurements with the 7 mm collimator. The results are shown in Fig. 5.15 and Fig. 5.16. The R^2-value is 0.995 on average.

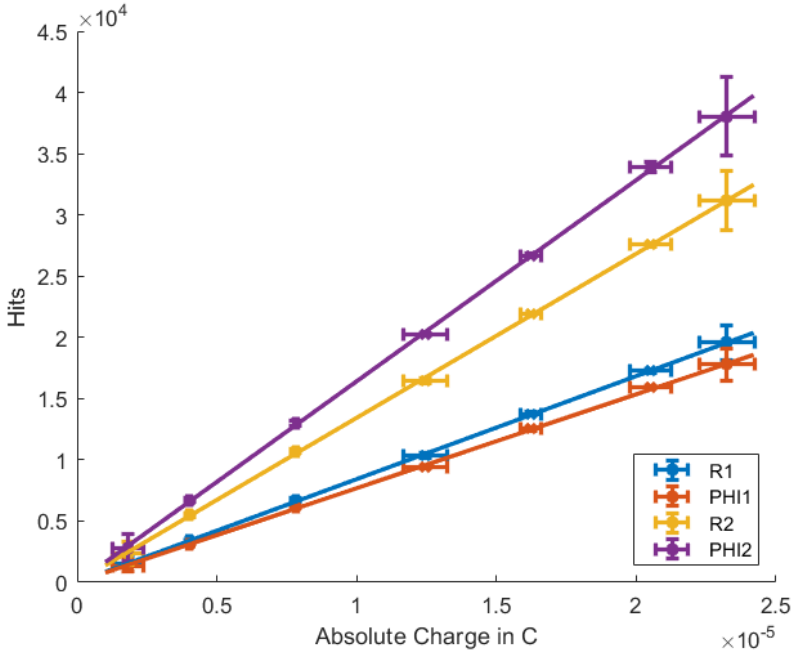

Figure 5.15 – Average hits of the VELO sensors per absolute charge measured by the electrometer using a 7 mm collimator.

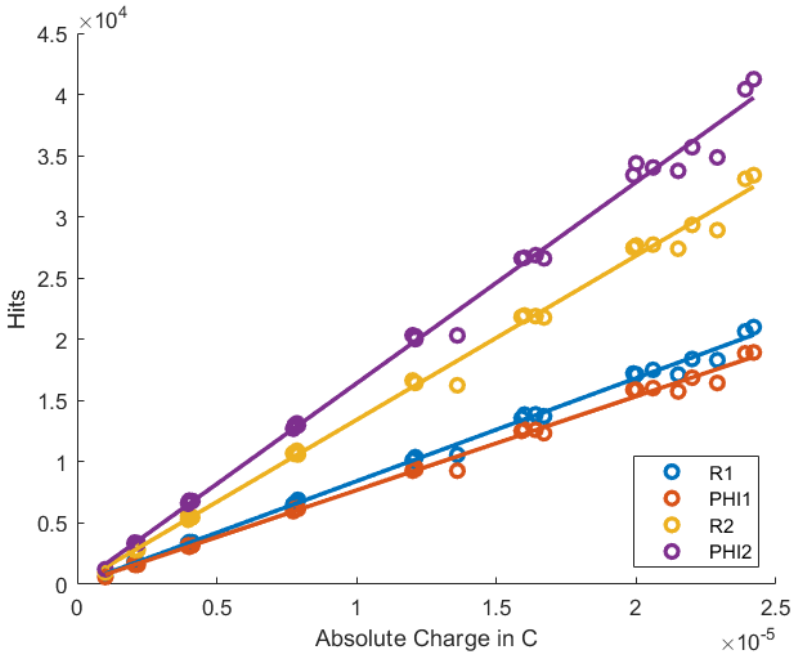

Figure 5.16 – Hits of the VELO sensors per absolute charge measured by the electrometer using a 7 mm collimator.

5.2.5 Beam profile measurements

Initial issues

To picture the beam profile, the VELO detector modules are designed with a unique strip geometry for the R- and PHI-sensor (see Fig. 5.17).

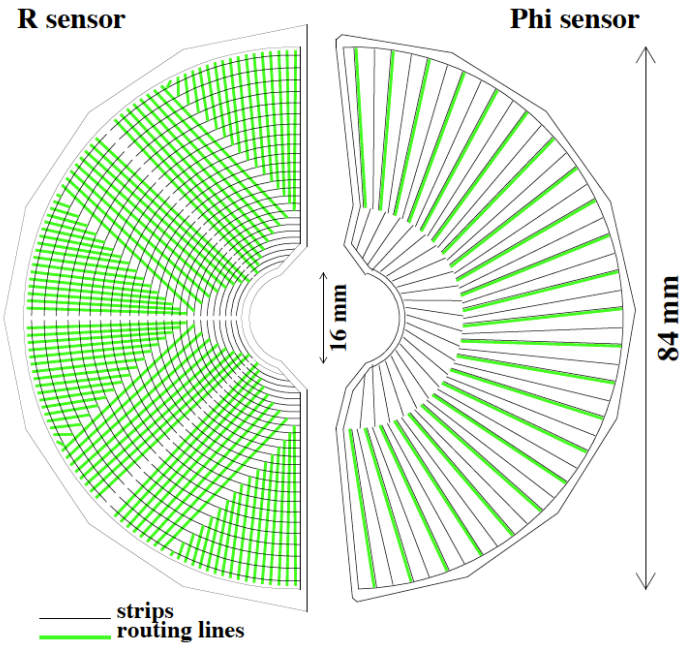

Figure 5.17 – Schematic strip geometry of the R- and PHI-sensor. The green routing lines collect the generated charge from the strips. For the R-sensor the routing lines are perpendicular to the strips and parallel to the PHI-sensor strips. [95]

An example of a hit distribution using the 20 mm collimator of the R1- and PHI1-sensor for module 1 is shown in Fig. 5.18. In the figure, the PHI-sensor is mirrored to the R-sensor for visualisation only. The distribution of hits appears random and not homogeneous, the beam spot is not resolved. The picture itself does not provide enough information. In Fig. 5.19, the total hits relative to the radius of the R1-sensor is shown. A sudden spike in signal at 13 mm and a sudden fall at 21 mm is observed, which cannot be explained with the encountered saturation. If compared with the routing lines in Fig. 5.17, it looks certain that the software is ordering the chip channels to the wrong strips. The reason is an error in the

original LHCb VELO experiment, where the original software corrected wrong cabling of the strips and chips.

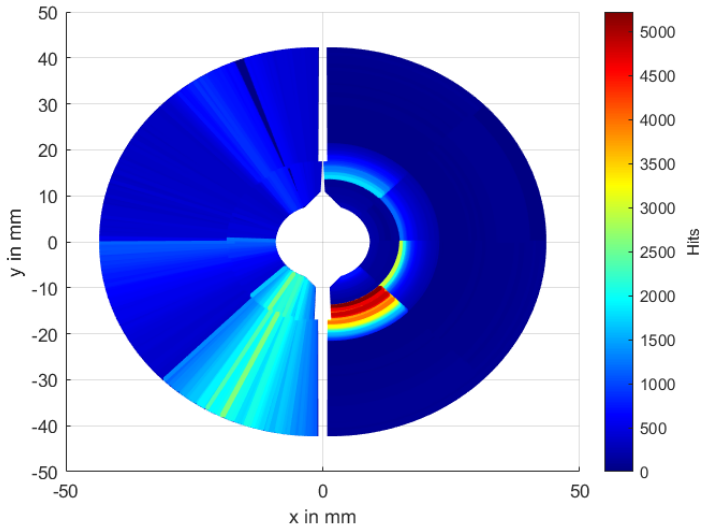

Figure 5.18 – Hit distribution using a 20 mm collimator of the R1- and PHI1-sensor for module 1. The PHI-sensor is mirrored to the R-sensor for visualisation only. Sudden signal spikes are observed for the R- and the PHI-sensor.

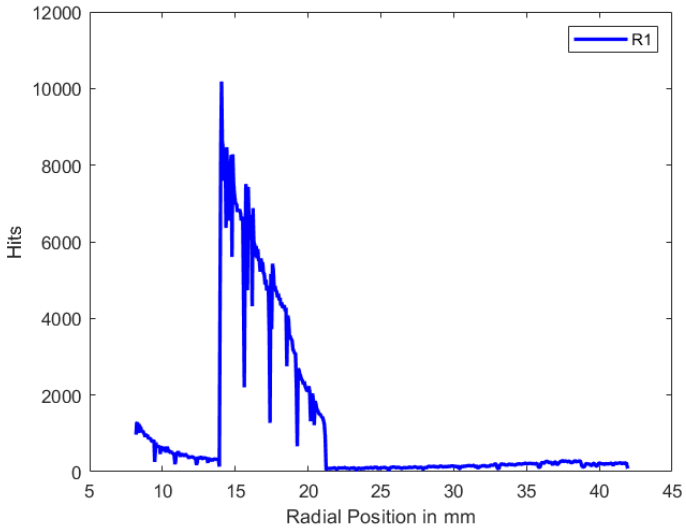

Figure 5.19 – Total hits of the R1-sensor relative to the radius. A sudden spike in signal at 13 mm and a sudden fall at 21 mm is observed indicating a wrong channel ordering (cp. with Fig. 5.17).

However, when the cabling correction was removed from the software, a similar error is observed with the PHI-sensors. In Fig. 5.20 the hits are shown for the inner (strip no. 1-683) and outer sector (strip no. 684-2048) of the PHI1-sensor against their angular position in Degrees. Although the PHI-sensors are not specifically divided into the four sectors as the R-sensors, the software is still grouping the PHI-strips in these sectors accordingly with 171 strips per sector for the inner part and 340 strips per sector for the outer part. The curve does not show smooth transitions but instead three sharp transitions at the sector edges. A closer look shows, that the hit distributions within the sectors should be flipped to achieve a smooth curve. Further, the hits for the inner and outer sector are almost identical, caused by an additional fault in the strip ordering. The mismatch follows a specific pattern for the two sectors, which was identified and corrected.
Ultimately, a software update was performed to solve the wrong strip and channel ordering.

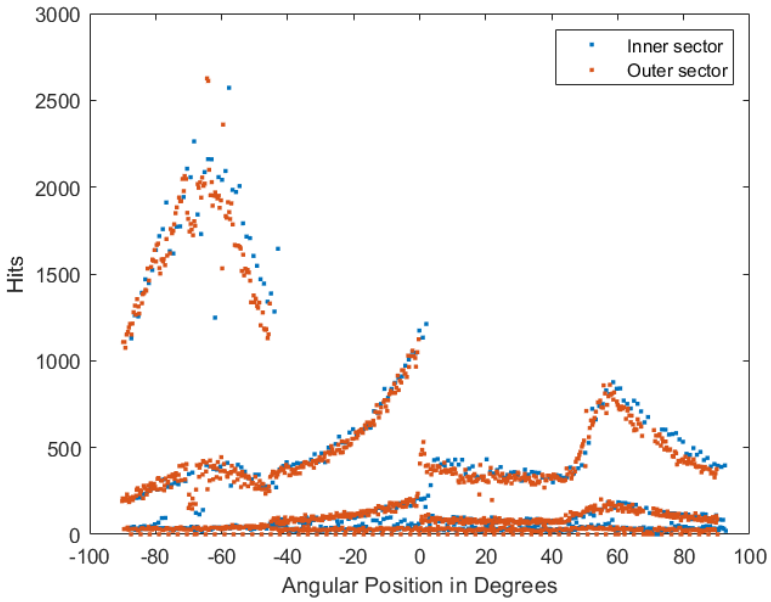

Figure 5.20 – Measured angular positions of the hits of the inner and outer sector of the PHI1-sensor.

For further visualisation of the beam profile, the R- and PHI-sensor is combined to one pixel map. Each hit for each event needs to be correlated to the dedicated the R- and PHI-strip with a beam crossing ID (BCID). As outlined in Fig. 5.3, the

DAQ desktop PC collects all events from the four TELL1 readout boards. Table 5.4 shows the extract of a data file. Only the information of one sensor is stored for one event, since the TELL1 boards operate independently from each other. To get the BCID information to correlate the events, the binary header data needs to be decoded. In [111], the non-zero suppressed data format is described. Each Multi Event Package stores the the event info, where the BCID is encrypted, for the VELO sensors.

After decoding the event info, the Bunch counter (BCnt, 12 bit) and the L0 Event Counter (L0-EvID, 32 bit) were extracted and also saved in the data file for each event. The timing and trigger system in the LHC is described in section 4.2.3. To synchronise all electronics, the readout supervisor ODIN sends a central clock signal to the whole system. In the stand-alone setup, neither ODIN, nor a replacement is present. Therefore, the BCnt for each event is assigned randomly and is not useful to correlate hits. The L0-EvID is incremented on every L0 trigger acceptance or in other words, when the readout trigger is sent out by the TELL1 boards. The L0-EvIDs between the four used TELL1 boards are not synchronised, since the reset cannot be done simultaneously. However, the pulse generator injects the external triggers simultaneously into the four TELL1 boards. The added fine delay during the phase scan optimises the timing, so that the triggers are approximately accepted at the same time. Hence as a proof of principle, the L0-EvIDs can be used to correlate the hits of the R- and PHI-sensor. In practice, three consecutive L0-EvIDs starting from the lowest ID are compared to account for ID skips and timing delays. The hits for the R- and PHI-sensor are correlated only, if the R- and PHI-strips are intersecting each other. The coordinates of the intersection point are saved as a pixel information. For large collimators, as the 20 mm collimator used in this example, a sensor registered around 350k hits per 100k events over five runs, which corresponds to three to four hits per event on average. This results in comparing a combination of almost 10^6 hits to each other, which requires a significant amount of computing time.

Capabilities of the VELO detector modules as a beam profile monitor

Various collimator diameter sizes were used on day 1 for beam profile measurements (cp. Tab 5.1). The proton beam energy used was 28 MeV. Collimator sizes smaller than 7 mm showed a negligible number of hits on the VELO detector modules. The capabilities to picture the proton beam are shown on the example of the 20 mm collimator with a beam current of 1 nA.

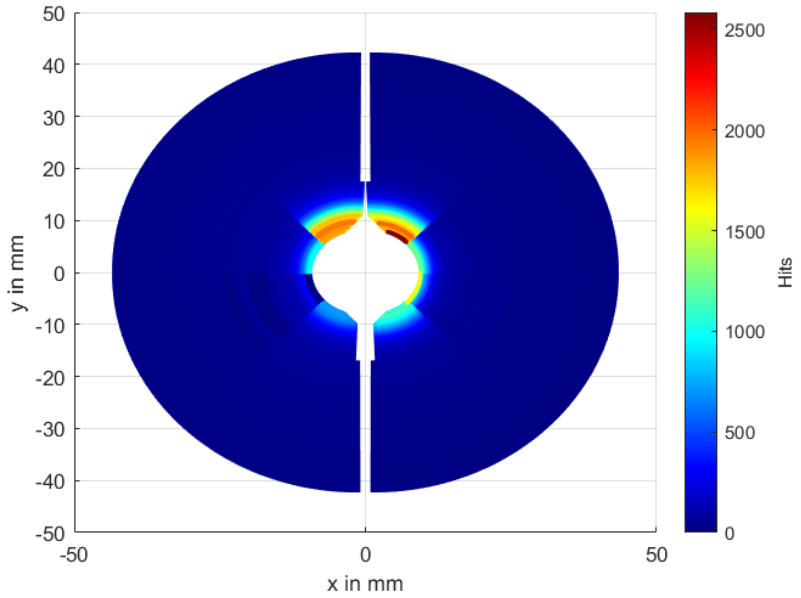

Figure 5.21 – The proton beam on the R1- and R2-sensor. The beam spot is predominantly in the upper right sector.

For an overview of the spatial hit distribution across the two R-sensors, a strip hit map is shown in Fig. 5.21. The four sectors of each R-sensor give more details about the hit distribution. The figure shows increased hits for the R2-sensor. The VELO detector modules seem to be too low from the centre of the beam spot. In total, the R2-sensor registered 336280 hits and the R1-sensor 300129 hits, 10.8% less. However, the different sectors show deviating characteristics. Most registered hits are in the top sector 4 for both sensors. The R1-sensor registered 174332 hits and the R2-sensor registered 160587 hits, thus 7.9% less. The difference in hits for both sensors in sector 3 is very low with a difference of only 1.1%, however is increasing rapidly to the biggest deviation of 60.8% in sector 2 and 31.2% in

sector 1. The reason of the large deviation in sector 2 is due to dead channels in the R1-sensor. This affects the 32 inner strips (strip no. 513-545) and 96 strips in the middle region (strip no. 672-736 and 768-800). If the dead strips of sector 2 are excluded for the R2-sensor, the hit difference between the two sensors is reduced to 4.3%. Figure 5.22 shows the integrated hits of the R1- and R2-sensor for all sectors excluding the dead channels. Since the R2-sensor has less hits registered in sector 1, but significantly more hits registered in sector 4, a non-uniform distribution of the beam spot is also likely. A comparison between the beam profiles is shown in Fig. 5.23. From the radial position of around 11 mm, the profiles show nearly the same trend. The reduced hits in R1 sector 1 impact the profile at around 9.6 mm. With the very high strip density in the inner region of the R-sensor, where strips are just 40 µm apart, changes in the proton beam distribution make a very high difference. A 1 mm deviation of the beam spot corresponds to 25 strips, which register more hits. Comparing the number of hits against the radial position for the sum of sector 4 and sector 1 for both sensors, the profile of the sum of sector 1 would need to be shifted 3.8 mm ± 0.5 mm to match with the profile of the sum of sector 4, which translates to the order of misalignment.

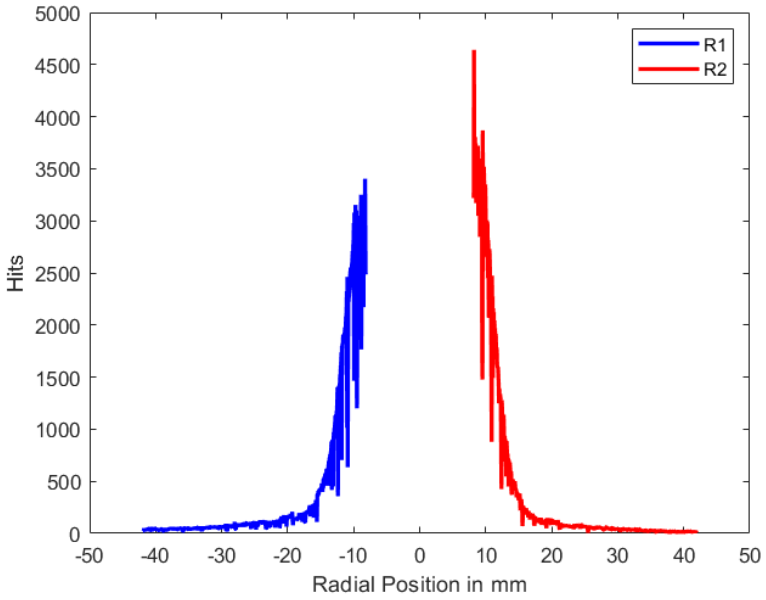

Figure 5.22 – Measured beam profile for the R1- and R2-sensor. More hits were registered by the R2-sensor.

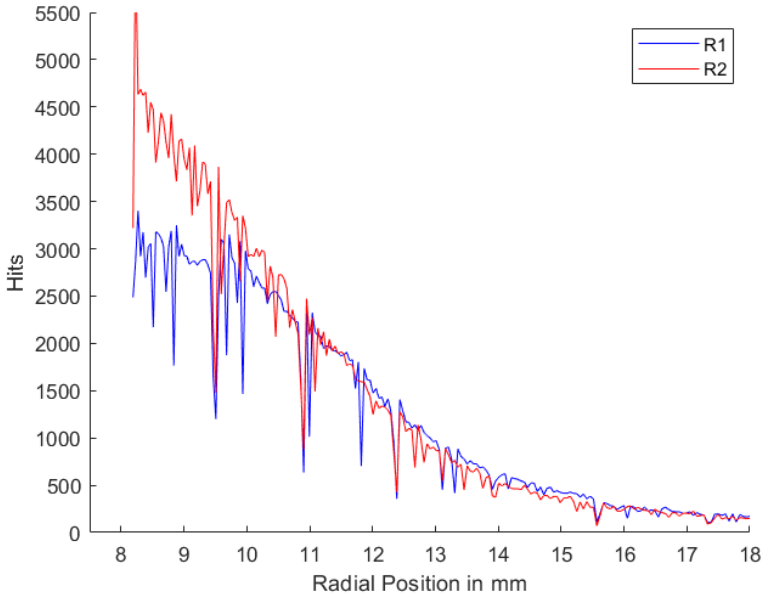

Figure 5.23 – Beam profile for the R1- and R2-sensor. More hits were registered by the R2-sensor up to r=11 mm.

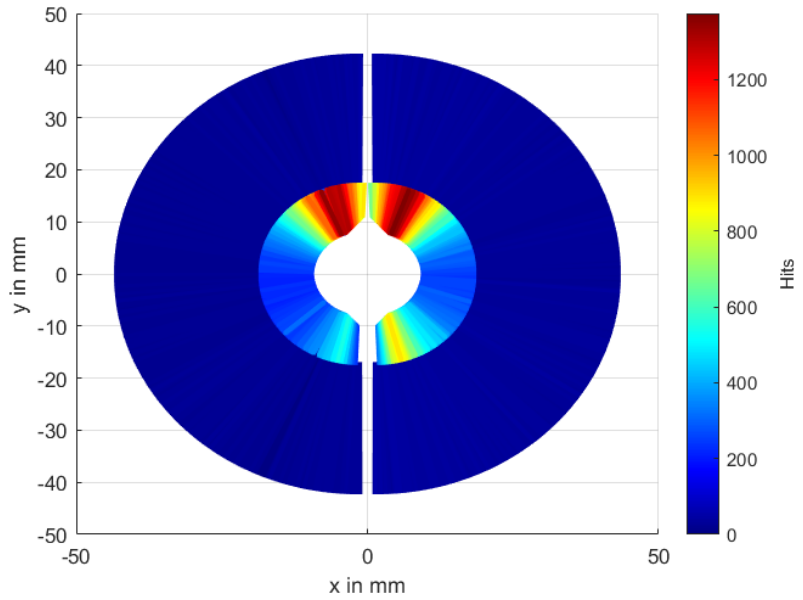

Figure 5.24 – Strip map of the hits on the PHI1- and PHI2-sensor.

Figure 5.24 shows the strip distribution of the hits measured by the PHI1- and PHI2-sensor. The PHI1-sensor shows 11 dead channels in the inner sector (strip

no. 76-86) and 21 dead channel in the outer sector (strip no. 833-854). For a perfect circular beam spot, the angular distribution should be homogeneous over all angles, which is not the case. To illustrate the distribution further, the angular distribution (see Fig. 5.25) and the distribution of the hits between the inner and outer sector for the PHI2-sensor (see Fig. 5.26) are shown. The trend of the angular distribution is the same for both sensors and they are showing more hits in the areas similar to the R-sensors. In total, the PHI1-sensor registered 312562 hits and the PHI2-sensor 381168 hits, 18.0% more. The inner sector of the PHI2-sensor registered 348451 hits and the outer sector 32717 hits, 8.6% of the total. The outer sector starts at r=17.25 mm, where only a small fraction of hits are detected (see Fig. 5.23).

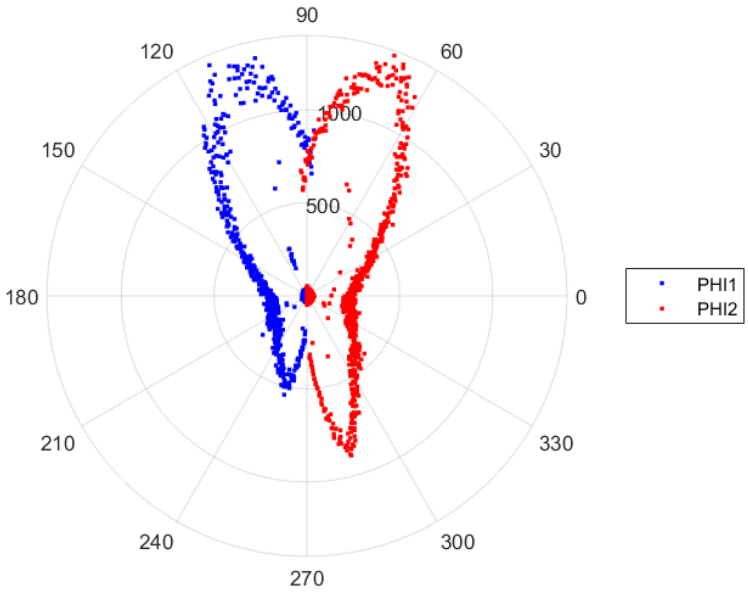

Figure 5.25 – Measured angular distribution in Degrees of the hits by the PHI1- and PHI2-sensor.

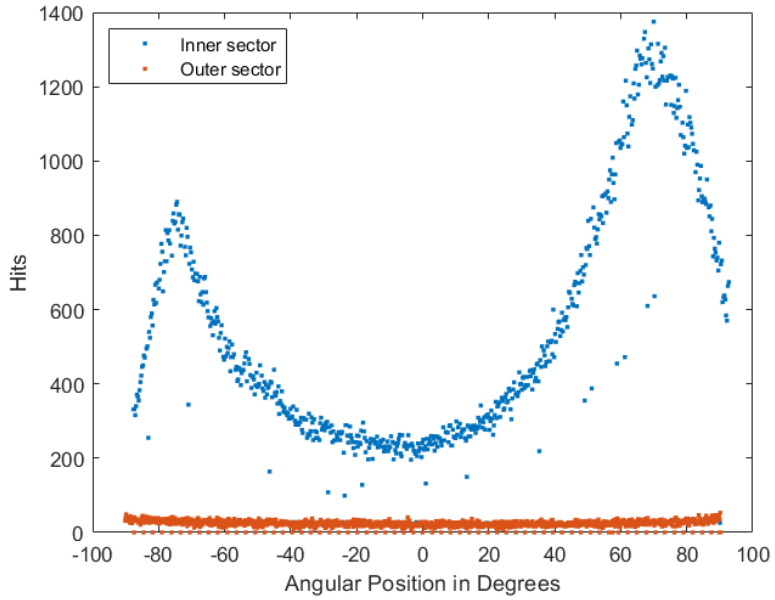

Figure 5.26 – Measured angular positions in Degrees of the hits of the inner and outer sector of the PHI2-sensor.

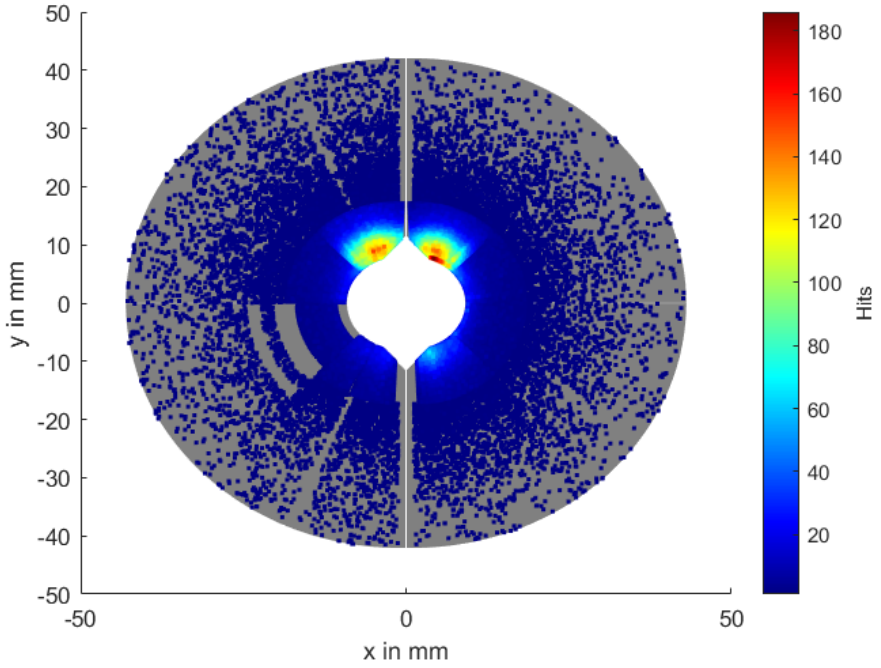

Figure 5.27 – Pixel map of the correlated hits for the two modules.

Finally, the hits of the R-sensors and the PHI-sensors are correlated as described in the previous section. The resulting pixel map is shown in Fig. 5.27. In total, $1.326 \cdot 10^6$ hits for the R1- and PHI1 sensor were correlated. These hits are distributed over 91848 pixels, where the highest number of hits is 151 for one pixel. For the R2-and PHI2-sensor, $1.502 \cdot 10^6$ hits are correlated and are distributed over 101576 pixels. The highest number of hits for one pixel is 186.

In the following, the results for the 10 mm collimator are shown for the proton energy of 28 MeV and 18 MeV for a beam current of around 1 nA.
Figure 5.28 shows the strip maps for the R-sensors and PHI-sensors for 28 MeV protons. In comparison to the 20 mm collimator, the number of hits are drastically reduced. The highest amount of hits of a single strip registered by the two R-sensors is 81, compared to the 2584 registered hits for the 20 mm collimator. In contrast to the 20 mm collimator, the R1-sensor (29956 hits) registered 24.8% more hits than the R2-sensor (22517 hits). The biggest differences in hits are 41.7% in sector 3 and 33.4% in sector 4. The hits against the radial position (see Fig. 5.29a) show a signal loss from the radial positions 8 mm to 10 mm for the R1-sensor. The lack of statistics is most likely the reason for these differences. However, the PHI1-sensor (27603 hits) registered 18.5% less hits than the PHI2-sensor (33848 hits) and is therefore comparable to the hit ratio of the 20 mm collimator. The pixel map (see Fig. 5.29b) for the R1- and PHI1-sensor registered 15857 hits over 14799 pixels, where the highest amount of hits of one pixel is 4. For the R2- and PHI2-sensor, 13191 hits were correlated over 12586 pixels and the highest amount of hits is 5. Therefore, the pixel map is less meaningful.

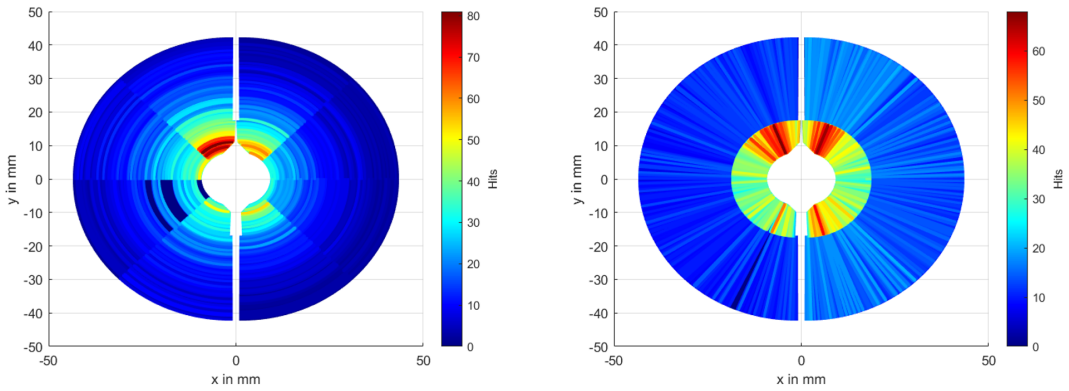

Figure 5.28 – Strip map of the hits of 28 MeV protons on the a) R1- and R2-sensor and b) PHI1- and PHI2-sensor for a 10 mm collimator.

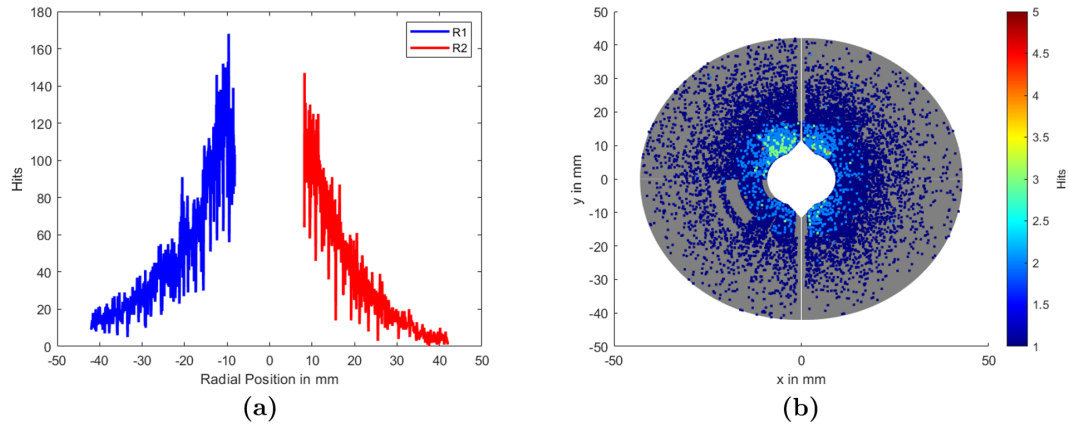

Figure 5.29 – a) Hits of 28 MeV protons against the radius of the R1- and R2-sensor. b) Pixel map of the correlated hits for the two modules.

Using the 10 mm collimator with a 18 MeV proton beam, results are shown in Figs. 5.30 and 5.31. The highest number of registered hits of a single strip is 433 for the two R-sensors. The R2-sensor (59687 hits) registered 38.1% more hits than the R1-sensor (36951 hits) and the PHI2-sensor (67096 hits) registered 45.7% more hits than the PHI1-sensor (36425 hits). 31142 hits were correlated over 22608 pixels for the R1- and PHI1-sensor with the highest amount of 8 hits for one pixel and 60918 hits were correlated over 37786 pixels for the R2- and PHI2-sensor with the highest amount of 12 hits. The beam spot can be clearly identified.

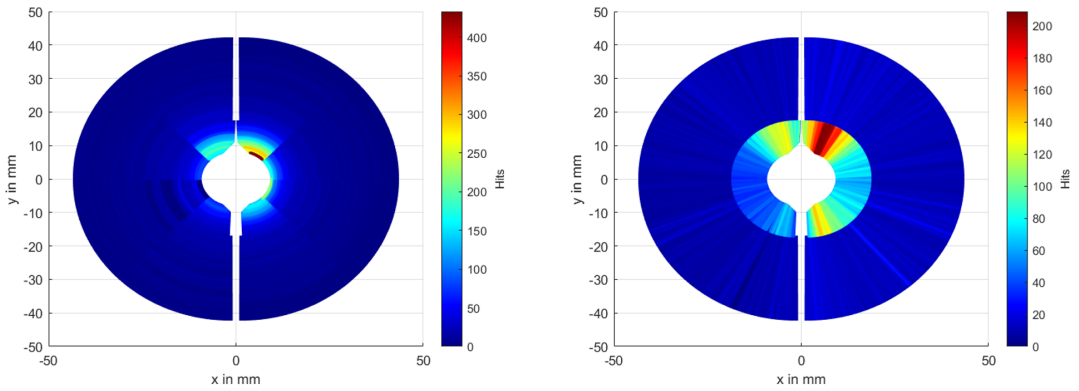

Figure 5.30 – Strip map of the hits of 18 MeV protons on the a) R1- and R2-sensor and b) PHI1- and PHI2-sensor for a 10 mm collimator.

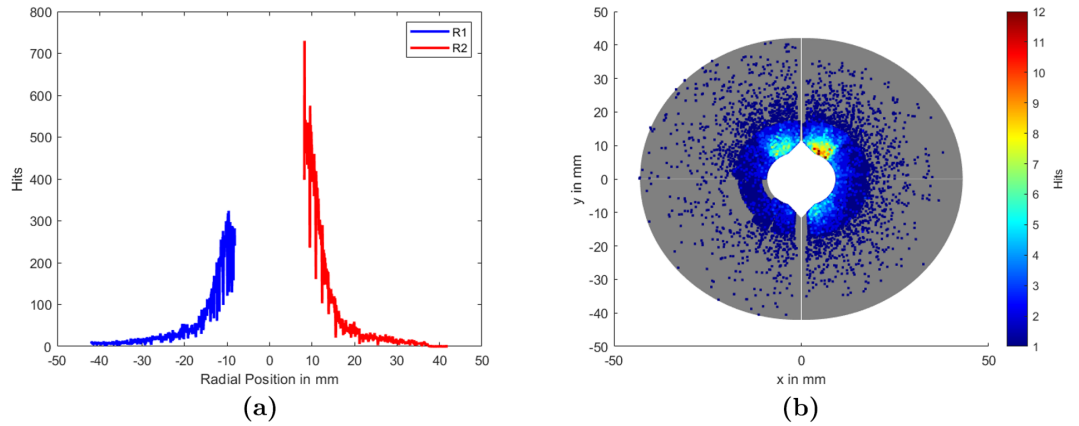

Figure 5.31 – a) Hits of 18 MeV protons against the radius of the R1- and R2-sensor. b) Pixel map of the correlated hits for the two modules.

The VELO detector modules have a very good capability to resolve the beam profile precisely. For a comprehensive study, the radial position and angular information show the extent of the profile and the strip maps of the R- and PHI-sensors visualise the beam spot further. Therefore, careful alignment with 100 µm accuracy needs to be assured to get satisfying results.

In the following section, beam profile measurements with collimators of 7 mm, 10 mm and 15 mm in diameter will be presented and compared to GAFchromic film measurements.

Beam profile comparison with GAFchromic film measurements

In order to compare the measured beam profiles of the VELO detector modules, EBT3 GAFchromic film measurements were performed on day 3. Because the scattering foil had to be removed, the beam needed to be shaped by changing the settings of the magnets. The distortion of the beam profile worsens with increasing diameter of the collimator (see Fig. 5.32a). Consequently, to recreate the original settings of the beam profiles on day 2, when the scattering foil was inserted, further film measurements were performed by Dr. Tony Price after the measurements with the VELO detector modules (see Fig. 5.32b). The conversion of the optical density of the films to an usable output (dose) was done by Jacinta Yap based on [112].

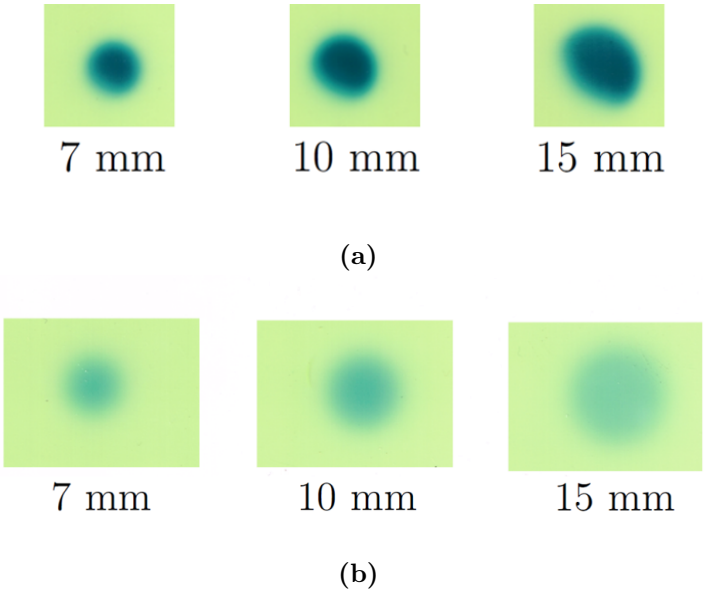

Figure 5.32 – Images of the beam for different collimators for a) day 3 and b) day 2. The removing of the scattering foil at day 3 resulted in distorted beam profiles.

To compare the beam profiles to film, the output of the two R-sensors is normalised at the radial position of +8 mm. The results for day 3 are shown in Figs. 5.33a (10 mm collimator) and 5.33b (15 mm collimator).

The distortion of the beam profile is clearly visible in the R1-sensor. While the region of interest of the film is at the beam centre, the R-sensor is integrating across the whole beam spot. Further, as shown before, the detector modules are slightly off-centred.

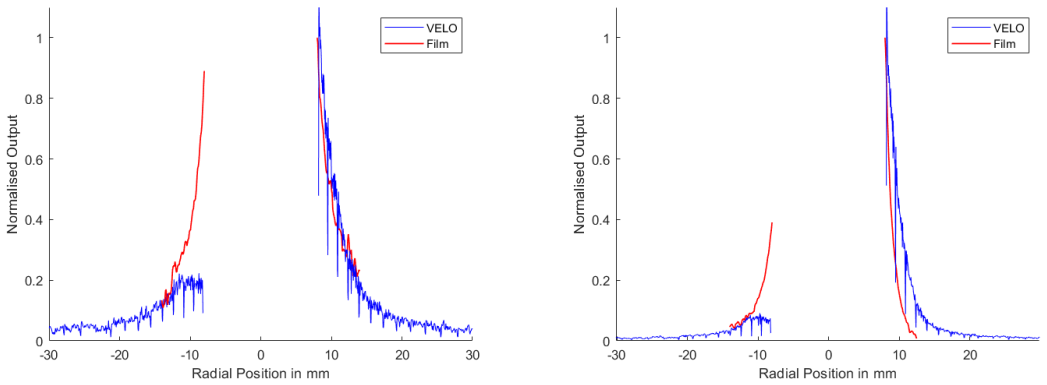

(a) **(b)**

Figure 5.33 – Comparison of the beam profiles of day 3 measured by film and the VELO detector R-sensors: a) 10 mm collimator. b) 15 mm collimator.

The film measurements compared to the VELO measurements of day 2 are shown in Figs. 5.34a and 5.34b. In addition, the simulated beam profiles of Fig. 5.4 are included.

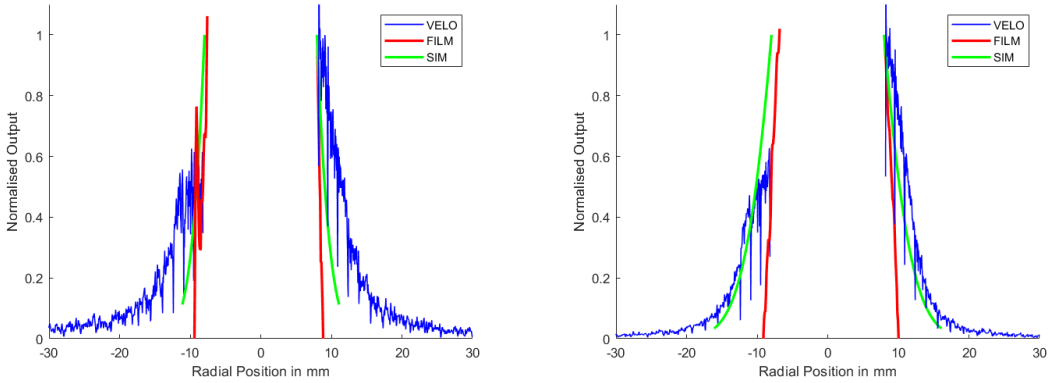

(a) **(b)**

Figure 5.34 – Comparison of the beam profiles of day 2 measured by film, the VELO detector R-sensors and the GEANT4 simulation: a) 10 mm collimator. b) 15 mm collimator.

The film beam profiles show a very steep gradient due to a low beam spot intensity, thus the low dose region is lost in the background. For the 10 mm collimator, the difference of the horizontal translation of the simulated beam profiles to the R-sensors is 2.5 mm±0.3 mm and 1.4 mm±0.2 mm for the 15 mm collimator.

Based on the misalignment of a few mm, the uncertainty is within the achievable accuracy.

In conclusion, the film measurements were heavily compromised by the beam settings on day 3 and by the low exposure on day 2. As a result, the comparison to the VELO detector modules is difficult. The radial profile of the R2-sensor agrees reasonable to the film measurements of day 3 and the simulated profile for day 2.

5.3 Summary

The LHCb VELO detector modules were implemented using the MC40 proton beamline at the University of Birmingham. Objectives of the measurements were to apply the stand-alone setup to a non LHC environment and characterise the detector modules response to changing beam currents and beam sizes. The proton beam saturated the ADC value. Only hits, the amount of times a strip registered a signal, were counted. For a synchronised readout with the proton bunch arrival, a phase scan was performed to identify the signal delay. Beam current measurements showed a very linear response of the VELO detector modules. Uncertainties arose through current fluctuations and the slow sampling rate of the electrometer. Regardless, the standard deviation of the registered hits are very low and equal or below 1%. Beam profile measurements revealed a wrong strip ordering of the R- and PHI-sensor and was corrected. The VELO detector modules were misaligned to the beam spot centre, which resulted in a signal enhancement in the upper sectors. Radial and angular information, strip and pixel maps were used to characterise several characteristics of the beam profile by the VELO detector modules. This gave a comprehensive picture of the proton beam. The beam profiles were also compared with film measurements and GEANT4 simulations. A distorted beam and poor film quality made the comparison difficult, but beam profiles of the R2-sensor agreed reasonable with the films and beam tracking simulations. Therefore, the VELO detector modules are able to detect the beam current and beam profile precisely.

6 Beam Halo to Dose correlation

In the previous sections, the VELO detector modules were assessed as a beam current and a beam profile monitor.
In order to operate the VELO detector modules as a beam monitor, the readings in hits need to be correlated to the clinical dose. In section 5.2.1, the correction factors k_{area} and k_{norm} were identified to relate different outputs for different settings to each other. The correction factors k_{corr} were calculated using Eq. 5.10 in Tab. 5.3 based on the simulated beam profiles and beam currents (see Figs. 5.4, 5.5). The simulated beam profiles showed a reasonable agreement with the measured beam profiles in Figs. 5.34a and 5.34b. Therefore, the established correction factors k_{corr} are used to compare the measured beam current readings of the VELO detector modules.

The beam current measurements of the four sensors are summed up and are compared for the 7 mm, 10 mm and 15 mm collimators. In Fig. 6.1, the fitted curves for the different collimators are shown. In Tab. 6.1, the gradients for the fitted curves of each sensor and the sum are shown and the ratios between the gradients for the different collimators are calculated in Tab. 6.2.

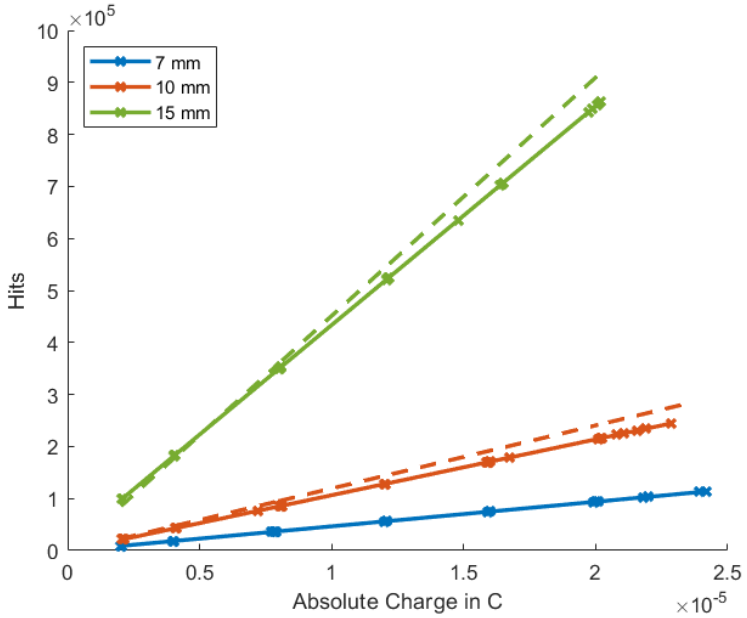

Figure 6.1 – Comparison of the beam current measurements of different collimators with the established correction factor from GEANT4 simulations (dashed line).

Table 6.1 – Gradients of the linear fit (cp. Fig. 6.1) of different collimator sizes for all four sensors.

Collimator diameter [mm]	**Gradient** $[10^9 \frac{\textbf{Hits}}{\textbf{C}}]$				
	R1	PHI1	R2	PHI2	VELO
7	0.87	0.79	1.38	1.69	4.61
10	1.95	1.93	3.24	3.62	10.57
15	7.18	8.27	12.37	14.28	44.29

In Tab. 6.1, the gradients of the four sensors are different. Firstly, module 2 shows a higher gradient because of the slight misalignment to the proton beam as described in the previous section. Secondly, gradient deviations between the modules are significant for the 7 mm collimator (see Fig. 5.16) and are small for the 15 mm collimator (see Fig. 5.9). Further, for the 7 mm collimator, the gradient of the R1-sensor is larger than the gradient of the PHI1-sensor. For module two, this relationship is reversed and the gradient of the PHI2-sensor is larger, however not as large as for module 1. This might be caused by the dead strips. Moreover, the deviations are most likely the result of the size of the proton beam. The FWHM

for the 7 mm collimator is smaller than the VELO detector aperture diameter, thus most of the beam is passing through. For the 15 mm collimator, the FWHM is similar to the VELO detector aperture diameter, thus the core of the proton beam is also interacting with the sensors. The combination of the proton beam interaction with the sensors and the slight misalignment to the beam are the main contributing factors to the observed differences. As a summary, the hits for each detector were added and the gradient for the whole VELO detector modules was determined.

Table 6.2 – Ratios of the linear fit (cp. Fig. 6.1) of different collimator sizes for all four sensors compared to the determined correction factors k_{corr}.

Collimator			**Ratio**			**Correction**
ratio	R1	PHI1	R2	PHI2	VELO	**factor** k_{corr}
10/7	2.25	2.44	2.36	2.14	2.29	2.57
15/10	3.68	4.29	3.81	3.94	4.19	3.78
15/7	8.29	10.48	8.97	8.45	9.61	9.70

Comparing the correction factors k_{corr}, established by the simulations, with the gradient ratios determined for the entire VELO detector in Tab. 6.2, the collimator ratios 10/7 and 15/7 are slightly smaller (-0.28 and -0.09) than k_{corr}. This corresponds to a deviation of 10.9% for collimator ratio 10/7 and of 0.9% for collimator ratio 15/7. The collimator ratio 15/10 is larger (+0.41, 9.8% deviation) than k_{corr}, which hints that the gradient for the 10 mm collimator is underestimated and the gradients for the other collimators might be slightly overestimated. Despite the uncertainties in the measurements, the results are still comparable to k_{corr} and should improve for a well centred detector and a very homogeneous beam.

To give an estimation of the dose, the following characteristics for the VELO detector modules need to be considered. The VELO detector modules are approximated to be pure silicon. From section 5.2.2, it is known that the proton stopping power in silicon is $S = 21.94\ \frac{\text{MeV cm}^2}{\text{g}}$ for an energy of 18 MeV. The density of silicon is $\rho = 2.328\ \frac{\text{g}}{\text{cm}^3}$ and each sensor is $d = 300$ µm thick. The total energy deposited by one proton is:

$$E_p = S \times \rho \times d \tag{6.1}$$

$$E_p = 21.94 \times 2.328 \times 3 \cdot 10^{-2}\ MeV = 1.53\ MeV \tag{6.2}$$

As an example, 90% of all hits in the VELO detector are registered below the radius of 22 mm for the 7 mm collimator. The interacting mass of the four VELO sensors is therefore calculated:

$$m_{VELO} = \rho \times d \times A \tag{6.3}$$

$$m_{VELO} = 4 \times (2.328 \times 3 \cdot 10^{-2} \times \frac{\pi}{2}(2.2^2 - 0.819^2))\ g = 1.83\ g \tag{6.4}$$

The resulting dose per proton is then:

$$D_p = \frac{E_p}{m_{VELO}} = 836.07\ \frac{MeV}{kg} = 1.34 \cdot 10^{-10}\ Gy \tag{6.5}$$

The total number of protons is derived from the charge C from Eq. 5.1. The charge is determined by the inverse hit to charge gradient for the VELO detector modules in Tab. 6.1 with the 7 mm collimator as the basis.
The number of protons is correlated to all collected hits from the VELO detector modules:

$$N_p = Hits_{VELO} \times 2.17 \cdot 10^{-10} \frac{C}{Hits} \cdot \frac{1}{160 \cdot e} \times k^*_{corr} \tag{6.6}$$

The number of protons is corresponding to the total charge measured with the ionisation chamber. The correction factor k^*_{corr} includes the actual number of protons interacting with the VELO detector based on the collimator size and refers to Eqs. 5.3 and 5.4.

The total dose is then derived as:

$$D_{VELO} = Hits_{VELO} \times 8.46 \cdot 10^{6} \frac{1}{Hits} \times k^{*}_{corr} \times 1.34 \cdot 10^{-10}\ Gy \tag{6.7}$$

$$D_{VELO} = Hits_{VELO} \times 1.13 \cdot 10^{-3} \frac{1}{Hits} \times k^{*}_{corr}\ Gy \tag{6.8}$$

As an example, for $5 \cdot 10^{4}$ registered Hits (around $1.1 \cdot 10^{-5}$ C with the 7 mm collimator), the dose, the VELO detector modules received, is approximated:

$$D_{VELO} = 56.5 \times \frac{0.063}{51.02}\ Gy \tag{6.9}$$

$$D_{VELO} = 69.8\ mGy \tag{6.10}$$

Therefore, the beam halo measured in hits by the VELO detector modules is successfully correlated to dose. For dose calculations in another medium such as water, Eq. 6.1 and Eq. 6.3 can be changed accordingly. The calculated dose is put in perspective to compare it to the radiation level in the LHC.

The VELO detector modules are made to withstand the harsh environment of the LHC and are exposed to higher particle fluences than any other silicon detector at the LHC [113]. In [86], the expected dose at different radii and z position was estimated for the four years' LHC Run II and is shown in Fig. 6.2. The maximum radiation damage of all neutrons for the closest radii is approximately $60 \cdot 10^{12}$ MeV neutron equivalents n_{eq} per area cm^2.
For a simple comparison to the calculated dose above, the number is assumed across the area of the detector modules.

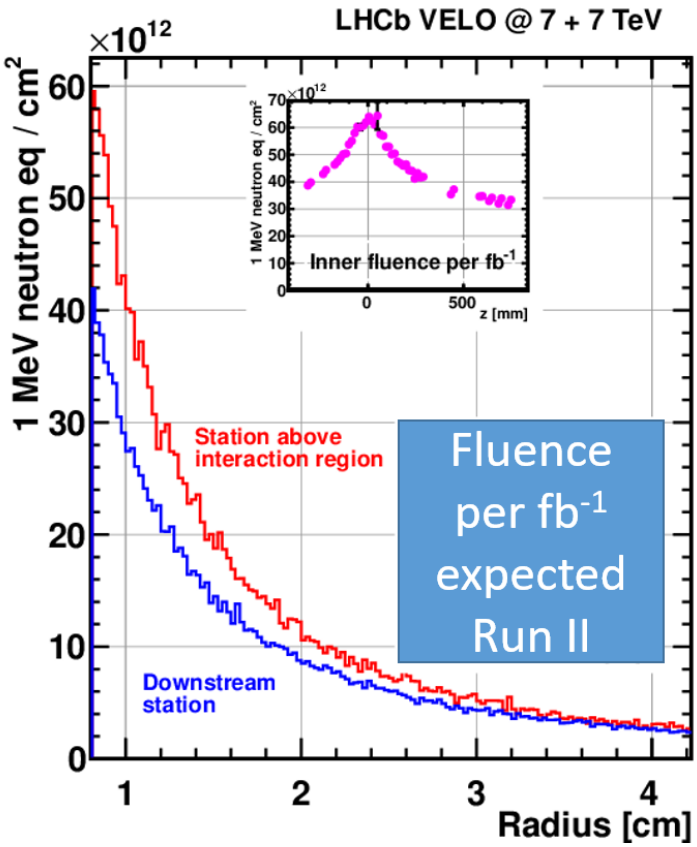

Figure 6.2 – Expected fluence of LHC Run II for the LHCb VELO detector. [113]

The total energy, neutrons are depositing in the detector modules, is:

$$E_{VELOdam} = 60 \cdot 10^{12} \cdot 10^{6} \times 1.602 \cdot 10^{-19}\ J \tag{6.11}$$

$$E_{VELOdam} = 9.61\ J \tag{6.12}$$

For the calculated weight of the four VELO sensors of 7.44 g the radiation damage dose is:

$$D_{VELOdam} = 1291.7\ \frac{J}{kg} \tag{6.13}$$

The dose is rather small by design, so very few neutrons deposit their energy in the very thin sensor making it long lasting.

However, the main process is the interaction of the collision particles with the silicon sensor and the creation of electron-hole pairs. In section 5.2.2, the most

probable energy loss value for a pion per µm silicon is 264 $\frac{\text{eV}}{\mu\text{m}}$. Using this value for the VELO detector modules, it is estimated that 100 particles are created on average at every proton-proton collision at 40 MHz. Further assuming for all angles, only 20% of the particles will go through the VELO detector modules and the number of detected particles is decreasing exponentially with increasing radius as shown in Fig. 6.2. Thus, the 3σ is at a radius of around 19 mm (information provided by Dr. David Hutchcroft, University of Liverpool, through private communication).
The total dose of random energy loss (i.e. scattering electrons) in silicon is:

$$E_{loss} = 264 \ \frac{1.602 \cdot 10^{-19} \ J}{\mu m} \times 300 \ \mu m \times 40 \cdot 10^{6} \ Hz \times 100 \times 0.2 \tag{6.14}$$

$$E_{loss} = 1.015 \cdot 10^{-5} \ \frac{J}{s} \tag{6.15}$$

$$D_{loss} = 7.87 \cdot 10^{-3} \ \frac{J}{kg \ s} \tag{6.16}$$

The LHC is operated 200 days a year and the beam is colliding around 80% of the time, thus one operational year is around $1.382 \cdot 10^{7}$ seconds.

$$D_{totloss} = 7.87 \ 10^{-3} \frac{J}{kg \ s} \times 1.382 \cdot 10^{7} \ s \tag{6.17}$$

$$D_{totloss} = 108.8 \ kGy \tag{6.18}$$

The accumulated dose is therefore 108.8 kGy per year and for the four years of operations in Run II, the total dose of the energy loss is 435.2 kGy. Adding the radiation damage, the total received dose is around 436.5 kGy.

During the measurement at the MC40 cyclotron proton beamline, the acquisition time of one data set was 20 s. According to Eq. 6.10, the received dose for the VELO detector modules is then 209.4 mGy per min. That means, it would need more than $2.08 \cdot 10^{6}$ minutes or almost 36700 hours of continuous beam irradiation to reach the dose levels at the LHC. This guarantees a reliable operation for years.

6.1 Summary

The derivation of the Halo to Dose relationship was the objective of the measurements performed using the MC40 cyclotron at the University of Birmingham. The concept of the Halo to Dose relationship was derived by the correction factors based on the GEANT4 beam tracking simulations. The measurement results of the beam current and different beam sizes were combined to calculate gradients of the linear fit and collimator ratios. Compared to the correction factors based on the simulations, the values showed a deviation of 10.9% for the 10/7 collimator ratio, 0.9% for 15/7 and 9.8% for 15/10. Due to the encountered misalignment and beam current fluctuations, the uncertainties are acceptable. However, for the use in medical accelerators and benchmark studies, the uncertainty must be below $<2\%$. The extensive knowledge of the beam parameters measured by the VELO detector modules were summarised and used to derive Eq. 6.8. The example calculation of the dose was compared to the dose level of the LHC Run II and a long operation time over several years is possible. The VELO detector modules showed the capability to operate as a proton beam monitor.

7 Discussion

7.1 The LHCb VELO detector modules as a beam monitor in a proton beamline

The LHCb VELO detector modules were installed at the MC40 cyclotron proton beamline at the University of Birmingham and extensive beam current and beam profile measurements were performed and characterised. Several hardware and software changes were implemented and used for the first time to achieve a synchronised readout and an optimised measurement of the proton beam. These changes are: the external trigger provided by the pulse generator synchronised with the RF frequency of the cyclotron to synchronise the proton bunch arrival on the VELO modules and the software trigger to synchronise the VELO detector readout with the readout of the external ionisation chamber.

7.1.1 Evaluation of the measurement results

The newly developed and synchronised readout system was tested and tuned with the phase scan measurement described in section 5.2.3.
The phase scan measurement demonstrated that the signal peak and working point to sample the arriving proton bunches on the detector was found successfully. As a result, very small hit standard deviations of approximately 1% throughout stable beam current measurements were observed. The implemented software trigger enabled successfully the simultaneous readout of the detector modules with the ion-chamber. Occasionally due to high GPU occupation of the DAQ desktop, the stop trigger to the ionisation chamber was slightly delayed after the VELO detector readout was finished. The triggers are a major advancement to the measurements done in [10], where no synchronised readout between the VELO detector

modules and the used Faraday Cup happened. This resulted in a range of combined uncertainties reaching as high as 15%, while observed errors in the current measurements were 2.5%. To summarise, both implementations were successful and are maximising the potential of hardware and software changes of the VELO detector modules.

Various settings of the cyclotron listed in Tab. 5.1 were tested. Beam current measurements showed that the VELO detector modules registered hits increasing linearly with the measured charge; even when beam current fluctuations during the data acquisition were experienced. The standard deviation was $\lesssim$1%. The measured charge by the electrometer showed a standard deviation of around 2.5% due to the processing delay described above and the integrated readout time of 0.5 s. The error was reduced by applying a time correction factor through the exact knowledge of the VELO readout time.

The first assessment of the beam profile measurements revealed a software issue, where the readout strips were assigned to the wrong channels in the readout chips. As a consequence, a false picture of the beam profile with distinguished cut off points was produced. The error was corrected by adapting the software and beam profile maps for the R-sensor and PHI-sensor. This revealed a slight misalignment of the VELO detector modules to the centre of the proton beam. During the alignment process, the laser system and rulers used to set up the modules allowed only a mm accuracy. This is not sufficient for the VELO strip architecture with a minimum strip separation of 40 µm. During the measurements, the analysing software was not capable of displaying the beam profile and therefore the misalignment was only observed after the campaign. However, the further developed post processing software shows the images of the beam quasi online now and can be used to address observed misalignments.

Further, the beam profiles were compared to GEANT4 simulations and GAFchromic film measurements. The film measurements on the third day suffered from the missing scattering foil, damaged the previous day. The results showed a distorted profile, which made the comparison more complicated. Nevertheless, the compared profiles of the 10 mm and 15 mm diameter collimator with the VELO detector module 2 showed a good agreement. Additionally, the film measurements with the scattering foil performed after the measurements, showed a beam spot with a

very low intensity. The low dose profile tail, especially interesting for the VELO detector, was mainly lost in the background. Thus, there is a scope to improve the quality of the film measurements in future studies. However, the performed GEANT4 simulations showed a sufficient agreement with the beam profiles monitored with the VELO detector modules.

The results of the GEANT4 simulations, the beam current and beam profile measurement of the VELO detector modules were combined to correlate the measured beam Halo to Dose for the first time. First, the beam current measurements to the different collimators were summarised and compared to the established correction factors from the GEANT4 simulations. The difference to the correction factors ranged from 0.9% to 10.9%. Further, the beam Halo to Dose relationship was derived with the acquired data sets. The relationship is dependent on the stopping power of the particles, which is well tabulated in literature and easily adaptable. With the found relationship, a beam Halo to Dose database for the MC40 proton beamline can be established and benchmarked for future measurements.

7.1.2 Advantages and challenges of the LHCb VELO detector modules as a proton beam monitor

The non-invasive, silicon-based detector geometry is the main advantage of the LHCb VELO detector modules. There are no similar existing detector technologies for medical accelerators. The beam monitor could require less time for daily calibration and calculations in chapter 6 showed the longevity over several years, which invasive silicon beam monitors are lacking.
The VELO detector modules showed the capability to measure the beam current and image the beam profile precisely. The detector is potentially capable to detect single protons. With the synchronised proton bunch sampling on the detector, the technology is able to measure even the smallest beam currents much smaller than common beam currents of 1 nA. The pitch between the strips is 40 µm to 100 µm and allows to detect very small deviations of the beam profile, exceeding the usual required resolution of 0.5 mm. Compared with GEANT4 beam tracking simulations, a beam Halo to Dose correlation was derived successfully. This required extensive knowledge of the beamline and a benchmark from simulation studies.

With an established database, the VELO detector modules are an effective tool to characterise the proton beamline.

The challenges are mainly the result of the original use of the detector modules in the LHCb experiment. Many functions needed for the operation at the LHCb experiment were disabled for the current setup. However, the extensive hardware setup, including the power supplies, TELL1 boards, repeater boards and cables for each sensor, had to remain to provide the basic functionality, such as providing the power to the readout chips. This results in a rather large footprint and makes it difficult to adjust the system for different integration sites. Further, the VELO detector is calibrated to detect minimum ionising particles, thus the proton beam saturates the ADC values and removes them as a characterising variable. Because the strip detector has such a high resolution, the alignment system must be very precise and must be automated to minimise setup time.
Additionally, the LHCb VELO strip technology is discontinued at the LHC. The age of the technology resulted in making comprises, such as using a pulse generator between the cyclotron and the TELL1 boards to synchronise the RF frequency or using different programming languages for the DAQ codes to synchronise the readout between the VELO detector modules and the ionisation chamber. The needed technical expertise or personnel, which was involved in the development of the detector modules, to change the discussed limitations, is no longer available, as developments for a new detector technology continued. The high complexity to fulfil the requirements at the LHC makes it difficult to transfer the technology fully to a medical environment.

Ideas to improve the current system and mitigate the challenges are described in the following section.

7.1.3 Possibilities for improvement of the stand-alone detector system

The stand-alone system was optimised for the integration into a proton beamline. Although many additional features were introduced for the VELO detector modules, the development is not yet exhausted. The solution to synchronise the proton bunch arrival with the detector readout was found effective; however, a method to bypass the pulse generator to inject the external trigger from the RF cyclotron

frequency would be desirable. With the current hardware settings of the TELL1 board, this is not possible. Ideally, the software trigger for external detectors could be integrated in the VELO detector readout scripts, however due to the old age of the scripts of over ten years, they are discontinued and obsolete for improvement. An improvement would be to exchange the slow charge integrating electrometer with a faster detector e.g. the Keithley 6485 Picoammeter with an integration time of the current of up to 0.2 ms, which was faulty during the measurement campaign. The faster electrometer will also calibrate the detector more precisely. The used ionisation chamber was provided by the University of Birmingham. The Faraday Cup, developed by [10], suffers from an impedance mismatch. Several attempts to overcome the problem with a Quarter Wavelength Transformer or Pi-resistor network failed, thus a redesign is necessary to potentially be able to detect single proton bunches.

Secondly, to further optimise the pre-processing software, a comprehensive user interface to control the DAQ of the TELL1 board, synchronised with the external trigger, to power the Beetle chips and to initialise the data transfer would simplify the use of the detector. Since the current scripts are 10+ years old and mainly written in C, a strong computational background is needed to pursue this. Moreover, an improved Vetra software should include the spill-over and clusterisation algorithm. Also, hit and space correlations of the two detector types would make the analysis faster and the measured data even more accurate.

7.1.4 Assessment of the LHCb detector modules as a proton beam monitor

To evaluate the characteristics of the LHCb VELO detector modules to monitor the beam current and the beam profile, the six most important characteristics were listed in chapter 3: Sensitivity, accuracy, resolution, dynamic range, measurement speed and reliability. As shown in the experiment, generally, all the measured parameters could be resolved precisely. Due to the requirements at the LHCb experiments to resolve MIPs, the sensitivity of the VELO detector modules exceeds the current requirements and causes saturation when protons hit the detector. A dedicated post-processing algorithm can mitigate the issue and enhance the VELO detector modules to count single protons. The accuracy of the VELO detector modules for the beam current measurements is excellent with an error usually $\lesssim 1\%$.

The strip geometry with µm resolution can resolve the beam profile accurately. A saturation of the hit counts was not observed during the measurements. During the measurement campaign, usually a TELL1 board readout trigger frequency of 1 kHz (1 ms) was used. With the current hardware configurations of the system based on the non-zero suppressed data, a maximum trigger of 20 kHz (50 µs) can be achieved. The technology was designed for a maximum readout frequency of 1.1 MHz (∼900 ns) [86]. The current setting compares to the speed of ionisation chambers and with the option to increase the speed further, future high dose rate treatment methods can be monitored. Furthermore, beam current fluctuations were also picked up precisely. After the measurements, the processing of the software to display the monitored parameters takes around 30 s. This is also due to the fact that the MDF files have a relatively large size with almost 600 MB for a 20 s data acquisition run. As calculated in chapter 6, the VELO detector modules are radiation hard and guarantee a long life time duration for a reliable use. The characteristics of the VELO detector modules are therefore sufficient. The VELO detector modules qualify as a beam monitor for medical accelerators.

7.2 The impact of the LHCb VELO detector modules of current and future beamlines and beam delivery systems

The need for a non-invasive beam current and profile monitor inside the beamline of medical accelerators is given and highly desirable. In the following, the feasibility of using the VELO detector modules as a beam monitor for beamlines and beam delivery systems is assessed based on the detailed evaluation of the measurements at the MC40 proton beamline in the previous section. This includes showing the possible application areas within the beamline, what detectors are needed for which part and what detectors are currently available. Finally, options are explored to equip the beamline with additional detector types next to the VELO detector modules.

First, the application areas within the beamline for the detector modules are outlined. Beam diagnostics are needed for the beam transfer line and beam delivery system. The accelerator, which is usually a compact system in cyclotron based facilities, will not be focussed.
The beam transfer line needs to preserve the pencil proton beam under high vacuum conditions to keep the spot size and emittance small and the beam current and energy the same. In Tab. 3.1 in chapter 3, multiple detector technologies are shown. Commonly used invasive detectors (ICs, scintillation screens) will degrade the pencil proton beam in the beam transfer line.
In the LHC beamline, the LHCb VELO detector was used in vacuum conditions. With the development to a stand-alone system, the operation in air was also achieved. The flexibility to apply it to different areas is an advantage. The VELO detector modules have the capability to observe the beam current and the beam profile precisely at the same time. Comparable non-invasive beam current monitors and beam profile monitors, which use the principle of electromagnetic induction, are used separately in the beam transfer line. This offers the opportunity for a reduction of the number of instruments and the used material. By installing a second pair of VELO detector modules, also the 3D beam trajectory of the particle beam can be recorded.

After the beam transfer line follows the treatment head or nozzle, the main application area for ionisation chambers. The application of the VELO detector modules

will vary by the beam delivery modes of the facility. Modern therapy facilities will use high proton energies of up to 250 MeV with a scanning system. The proton beam is steered by the sweeper magnets to a maximal field size of 40×30 cm^2 and the shape of the scanned layers is highly inhomogeneous. The large plane-parallel ionisation chamber can cover these field sizes easily and reproduce the shape. As a result, the architecture of the LHCb VELO detector is not optimal to monitor the rapidly changing beam spot in that area.

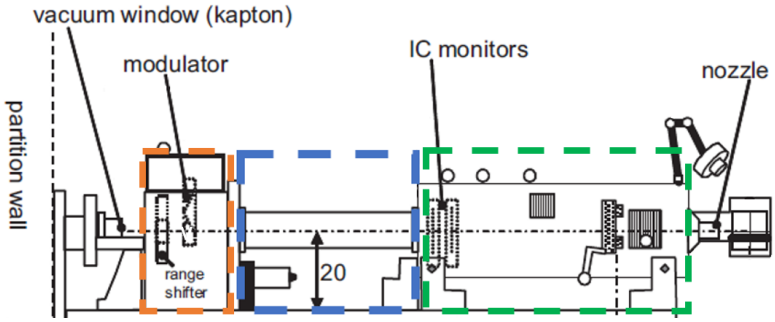

Figure 7.1 – Sketch of the CCC proton therapy beamline. The blue box marks the integration zone of the VELO detector modules. They are placed between the modulator box (orange) and diagnostic box (green). The present aluminium pipe will be removed. Adapted to [9].

In contrast, double scattering systems are applied mainly for ocular tumour treatments with low energy protons of 62 MeV like in the Clatterbridge Cancer Centre. Considered sometimes as obsolete, there is still a need for ocular proton therapy beamlines [114]. The scattered proton beam after the two foils shows a much more homogeneous shape. In this case, the beam monitoring is easily doable for the VELO detector modules and currently used ionisation chambers would have no advantage to them. The case was studied in [108], the integration zone for the VELO detector modules is between the modulator box and diagnostics box (see Fig. 7.1). The FWHM of the simulated primary proton beam between the beginning and the end of the integration zone is from around 22.1 mm to 25.7 mm. When the VELO detector modules are implemented, GEANT4 simulations on the interaction with the proton beam showed a negligible energy loss of 0.07% at the distance closest to the modulator box to 0.18% at the distance closest to the diagnostic box.

To summarise, the VELO detector modules show a strong potential to be applied

either in the beam transfer line before the sweeper magnets, if the facility uses a scanning system or behind the double scattering system.

7.2.1 Detector systems for current and future beamlines

Looking forward to the design of current and future beamlines, it is no surprise that non-invasive beam monitoring will be the desired path. However, invasive technologies, such as screens, wires and ionisation chambers have the big advantages of being simple to use and cheap. Further, for the beam scanning technology with inhomogeneous field sizes and spot maps, there is no alternative to interact directly with the entire beam to assure the quality and precision. Thus, ionisation chambers still have the best price and performance ratio in the beam delivery system.

However, the beam transfer line can benefit hugely by reducing the detector material interacting with the beam. Many developments are ongoing and can assist the VELO detector modules in characterising the beam. At the medical treatment facility PROSCAN at the Paul Scherrer Institut (PSI) the proton beam current (0.1–40 nA) is measured by ion chambers. To replace these, S. Srinivasan and P. Duperrex [115] developed a dielectric-filled reentrant cavity resonator to measure the low-intensity proton beam current. The resonant cavity matched the second harmonic of the pulse repetition rate of the beam extracted from the cyclotron for the measurement. Further minimal invasive detector technologies, which have been used for different applications are available to be transferred to medical beamlines. Developed for transverse profile diagnostics of electron and proton beams in the High Luminosity LHC, the 2D beam profile monitor based on a supersonic gas curtain is a viable alternative for medical accelerators [116]. A thin supersonic gas curtain crosses the primary beam and fluorescence caused by the interaction between the beam and gas curtain is detected using a specially designed imaging system. This method is very flexible to use within the beamline, since electromagnetic fields have no influence on the detection.
Measurements of the emittance with the pepper pot method or quadrupole scans with screens are destructive or highly invasive. In [117], K. Nesteruk presents the 4PrOBεaM (4-Profiler Online Beam Emittance Measurement) system to measure the transverse RMS beam emittance. The integrated system with four doped silica

fibres passes across the beam and the produced scintillating light is transported to a readout device and its intensity is plotted online as a function of the fibre position. In this way, the beam size, shape, and position can be precisely determined. This detector was only used at a 18 MeV proton beamline, but the monitor can operate in pulsed and continuous beams and detect intensities from 1 pA to tens of μA and is thus ideally suited for application in hadron therapy. As described in section 3.3.2 for detector solutions at the end of the beamline, silicon-based pixel sensors like Medipix3 can potentially replace film measurements to measure the beam current and size online.

These detector technologies can be combined with the VELO detector modules to form one comprehensive monitoring solution for proton and heavy ion beams in treatment beamlines. This will provide detailed information about the beam intensity, profile, halo, position and emittance, thus fully characterising the beam and monitoring the dose delivered to the patient without stopping the accelerator. This would reduce the machine preparation and Quality Assurance time significantly and ultimately save lives by treating more patients.

7.3 Summary

The non-invasive, silicon-based detector technology is novel and highly desirable. The accuracy of the VELO detector modules for the beam current measurements is excellent with an error usually $\lesssim$1%. The strip geometry with µm resolution can resolve the beam profile accurately. A beam Halo to Dose database for the MC40 proton beamline can be established and benchmarked for future measurements. The relevant beam monitor characteristics, e.g. accuracy or sensitivity, of the VELO detector modules are therefore sufficient. Hence, the VELO detector modules qualify as a beam monitor for medical accelerators. Methods to reduce the used hardware and to further optimise the software are shown and would be desirable, but will be difficult to implement in the outdated technology. The VELO detector modules are able to be operated in air or vacuum and show a strong potential to be applied either in the beam transfer line before the sweeper magnets, if the facility uses a scanning system or behind the double scattering system. Combining the VELO detector modules with newly developed non-invasive beam monitors, e.g. the 2D beam profile monitor based on a supersonic gas curtain or 4PrOBεaM, can achieve a full characterisation of the beam.

8 Conclusion

8.1 The LHCb VELO detector modules as a non-invasive, silicon-based beam monitor for medical accelerators

In this work, a novel silicon semiconductor detector technology for medical accelerators was explored. The chosen, non-invasive online beam monitor is based on the VErtex LOcator, originally developed for the Large Hadron Collider beauty experiment at CERN. The unique semi-circular detector geometry offers the possibility to correlate the proton beam through halo measurements without interfering with the beam core. As current systems in use are either invasive, e.g. ionisation chambers, or measure single beam quantities, e.g. current transformers, the LHCb VELO detector modules present a highly desirable and novel beam instrument solution.

Various technical adaptations to the original setup were performed to develop a stand-alone system. A commercial chiller and dryer were used to operate the detector in ambient air for temperatures of the sensors below 0 °C. This prevented the degradation of the silicon sensor and suppressed noise. The VELO detector modules were embedded in a plastic case including the entrance and exit of the cooling and venting pipes to guarantee a safe and smooth operation. The case was connected to a precise positioning system consisting of three translational stages with a position accuracy of below 1 mm in the beam propagation direction z and its transverse plane x. Substantial amount of work was dedicated to optimise the electronics. A stable communication from the TELL1 board to the Beetle chips via I^2C was established by providing separate power supplies for the modules and by optimising the grounding of the system. The configuration of a new set of delay parameters in clock cycles for correct data sampling due to hardware and cable changes was also performed.

The major new developments in this work were the matching of the readout of the VELO detector modules with the proton bunch arrival given by the RF frequency of the cyclotron to sample at positive points of the output pulse and the upgrade of the software for quasi online beam monitoring. The original system is tuned to the particle bunch arrival frequency $f_{LHC} = 40\,\text{MHz}$ and thus, the clocks of the Beetle chips and TELL1 boards cannot be changed directly. The solution was to introduce another clocked system and update the TELL1 board firmware with a newly introduced 120 MHz clock in phase with the 40 MHz TELL1 clock. An external readout trigger is injected by a pulse generator, which is synchronised by the RF frequency of the cyclotron. A test with a pulsed infra-red Laser Diode, synchronised with the readout of the VELO detector modules, increased the measured signal by an average of 2.86 times, whereas the average standard deviation was down almost 20 times. In order to decode, reformat and process the data, the used Vetra application was subject to a highly non-trivial customisation procedure to be able to process the medical beam experimental data. This included the conversion of the binary data to a readable format and safe storage. Various algorithms were included to normalise the offset (pedestal subtraction), to reduce storage (zero suppression) and to set signal thresholds. Further, an analysis framework was built to visualise histograms including the pedestal corrected data or hit distributions on a single R- or PHI-sensor.
The adaptations to the stand-alone setup fulfilled the requirements to implement the VELO detector modules at the MC40 proton beamline at the University of Birmingham. Different beam sizes of spot diameters from 7 mm to 20 mm and beam currents from 0.2 nA to 6 nA were recorded by the VELO detector modules. Beam current measurements showed that the registered hits increased linearly with the measured charge with standard deviations usually $\lesssim 1\%$. This proves the success of the implemented synchronisation methods. The VELO detector modules were misaligned to the beam spot centre, which was visible in the radial and angular beam profile figures. Dead channels for module 1 were observed, thus it should be replaced. Nevertheless, the developed pattern recognition algorithm based on the TELL1 board event counter enabled the hit correlation and space hits reconstruction. This allowed pixel maps generation of the two modules and gives a comprehensive picture of the proton beam.

The success of the measurement was also determined by comparing the results of the VELO detector modules with derived correction factors based on GEANT4 simulations. The correction factors differed around 10.9% for the 10/7 collimator ratio and only 0.9% for the 15/7 collimator ratio. The errors can be traced to the misalignment and the beam current fluctuations. The final objective of the measurements, to derive a halo to dose relationship was successfully achieved. The equation combines the knowledge of the proton energy, the hits on the VELO detector modules and the measured charge. In a simple comparison of the received dose to accumulated dose of LHC Run II, the detector system is capable of a long operation time of several years. All technical aspects for operating the LHCb VELO detector modules as a beam monitor are sufficiently shown. The system can be used to benchmark existing beamlines of medical accelerators.

8.2 Outlook

Regarding beam parameter specifications, the VELO detector modules are sensitive, accurate and have a good resolution for beam current and profile measurements and interact only with a fraction of the beam. The advantages of a non-invasive beam monitor are clear and the use of silicon semiconductor technology is sharply on the rise in medical accelerators. The increased speed and easy maintenance will reduce the time used for Quality Assurance and thus allow more time for patient treatment. However, the main disadvantages of this detector are the outdated electronics hardware and pre-processing software. In the following several outlooks are given, which cover the developments of the VELO detector modules, alternative design solutions and future detector studies for medical accelerators.

Future R&D possibilities

Continuing the research project would directly connect to the possible improvements described in section 7.1.3. The next step for the detector system would be the integration into the Clatterbridge Cancer Centre, the original plan of the

entire project and a real clinical environment. Several circumstances, e.g. a heavily increased patient number and staff changes, made it impossible to accomplish it in the time frame of this project. Further, the detector modules should be characterised by heavy ion beams in facilities such as the MedAustron or the GSI Helmholtz Centre for Heavy Ion Research. These interesting studies would show the performance of the VELO detector for clinical beams and be a validation and comparison to the measurements at the MC40 proton beamline. Further research aspects include detector saturation studies, if higher currents hit the counting limit or if heavy ions oversaturate the detector. Signals may not be distinguished or in the worst case, sensor damage is observed. The large footprint of the system requires careful planning and time allocation and is therefore not flexible in use.

Future design possibilities

The redesign of the sensor and electronics for a smaller system and more efficient data transfer would be highly recommended; however, it is rather difficult due to the outdated technology and missing expertise. Many functions and parts based on the original LHCb experiment are hard to circumvent. Thus, in a theoretical scenario, what design parameters should be chosen for medical accelerators?

1. Material size reduction of the sensor and strip geometry
   Integrating detectors in beamlines, the cost of silicon-based technologies is an important factor. Thus, the size of the detecting area needs to be optimised. VELO detector modules would excel in observing nearly Gaussian shaped proton beams in the beam transfer line or in facilities with passive beam shaping. The sensor geometry and strip size can be adapted accordingly. As an example, the spot sizes of the proton beam of the IBA S2C2 cyclotron are usually larger than 3 mm and smaller than 8 mm [118], thus the aperture size of the detector modules of 8 mm is still reasonable. However, the pitch between the strips can be generalised to 100 µm as a reasonable resolution. To further reduce material and cost, the radius of the active detector can be reduced from 42 mm to 30 mm to cover a sufficiently large 60 mm field size. For Gaussian shaped proton beams, the R-sensor provides generally enough information of the beam size. For a better resolution the sectors can be increased from four to eight. Therefore, the PHI-sensor can be removed

and 50% of the material and electronics with it. If the combined information of the R- and PHI-sensor is viewed too valuable, pixel detectors, an example is described below, would be the alternative.

2. Reducing and optimising hardware and electronics
   As mentioned in section 7.1.3, additional hardware is needed to cover the long distances in the LHC tunnel. In an optimised version, the TELL1 board should be the only module to handle the processing of the power supply, signal communication and synchronisation. This would make the repeater boards and the used pulse generator obsolete. A dedicated software framework around the functions of the TELL1 board needs to be built to fit into the control systems used in medical accelerator facilities. The readout chips need to be adaptable in their sampling rate, thus tuning to the different frequencies of cyclotrons is possible. Also, the sensitivity of the chips has to be adjusted to detect protons.

As an already ready to use alternative, the new LHCb VELO detector upgrade VELOpix uses pixel sensor technology [119, 120].
The detector consists of a 256×256 pixel array (55 µm per side), resulting in a sensitive area of 14.08×14.08 mm^2 (see Fig. 8.1). The silicon semiconductor technology of the pixel is reduced to 200 µm thickness. One of the main improvements of the new detector is the VELOpix ASIC [121], which is based on the electronic design of the Timepix3 ASIC and increases the readout from 1.1 MHz to 40 MHz with a bandwidth of 20 Gb/s. The modules will feature also mechanical changes, such as a refined cooling system through micro-channels in a silicon substrate, directly beneath the ASIC chips, since the power consumption and heat production will double. Furthermore, the VELOpix will be 3 mm closer to the LHC beam and needs to handle 20 times more fluence of $8 \cdot 10^{15}$ MeV $\cdot\, n_{eq}/cm^2$, increasing the needed radiation hardness substantially.

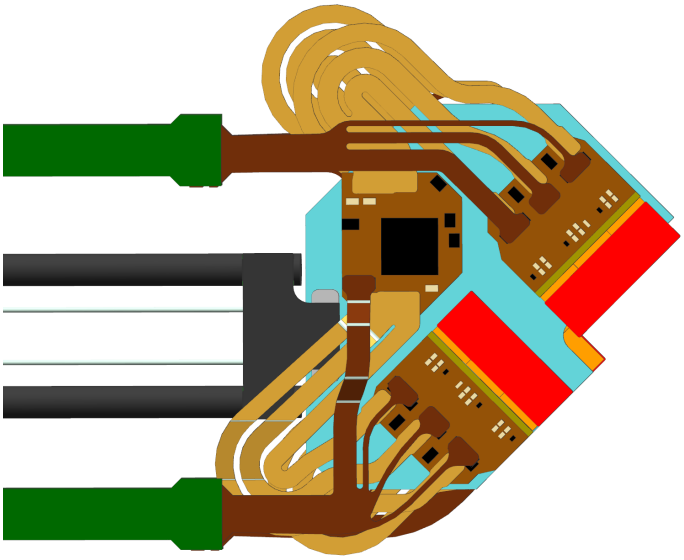

Figure 8.1 – The VELOPix detector for the LHC upgrade. Each side has two sensors (red), read out by the newly developed ASICs (orange) cooled by the micro-channels in a silicon substrate (blue) [122].

The increased readout speed would enable to monitor single bunches in a proton beam and to measure the beam energy potentially. This could lead to an even better performance status report of the accelerator. The technology to build an optimised detector for medical accelerators is therefore accessible. As the developments of Medipix and Timepix detectors have shown, a redesign for the targeted application areas was proven to be successful. Through the findings of the study of this thesis, it is strongly encourage to pursue the development of this non-invasive silicon-based detector technology for medical accelerators.

Future beamline detector system possibilities

The research into novel detector solutions is a constitutional foundation in accelerator science and technology. The developments are usually focussed on a specific purpose for a specific medical accelerator type. For a comprehensive detector solution to measure all relevant beam parameters, a collaboration of key players needs to be identified. Examples for different kinds of detectors are given in section 7.2.1. These three to four players should build a diagnostic test bench at a facility

using advanced particle beams. The goal should be to combine existing or new non-invasive detectors to one diagnostics solution. The development needs to focus on a smart and compact design to follow a straightforward route to commercialisation. This requires the inclusion of one of the market leaders for proton therapy systems, such as IBA or Varian, and closely following the metrology for particle beams published by the national metrology institutes, such as NPL in the UK or PTB in Germany. This all in one diagnostic solution offers a further reduction in the accelerator maintenance.

List of Abbreviations

LHC Large Hadron Collider

LHCb Large Hadron Collider beauty experiment

VELO Vertex Locator

CERN European Organisation for Nuclear Research

CCC Clatterbridge Cancer Center

FC Faraday Cup

DNA Desoxyribonucleinacid

CSD continuous slowing down

MCS multiple Coulomb scattering

SOBP spread out Bragg peak

LINAC linear accelerator

HIMAC Heavy Ion Medical Accelerator in Chiba

RF radio frequency

QA Quality Assurance

IAEA International Atomic Energy Agency

TRS Technical Report Series

IC ionisation chamber

LET linear energy transfer

MU Monitor Unit

OD optical density

CI Cockcroft Institute

TPG Thermal Pyrolitic Graphite

CF carbon fibre

NTC Negative Temperature Coefficient

FE front end

TELL1 Trigger Electronics and Level 1

I^{2}C Inter-Integrated Circuit

2PACL 2-Phase Accumulator Controlled Loop

LV low voltage

HV high voltage

ECS Experiment Control System

ARx analogue receiver

NZS non-zero-suppressed

ZS zero-suppressed

FPGA Field-Programmable Gate Array

ADC Analogue to Digital Conversion

CCPC Credit-Card PC

TFC Timing and Fast Control

DAQ Data Acquisition

PCN pipe column number

MEP multi event packages

GEANT4 GEometry ANd Tracking 4

FWHM Full Width Half Maximum

MIP Minimum Ionising Particle

BCID beam crossing identity

L0-EvID L0 Event Counter

BCnt Bunch counter

ASIC Application-specific integrated circuit

List of Figures

1.1 Setup of the test measurement with one LHCb VELO detector module at the proton beamline of the Clatterbridge Cancer Centre. 3

1.2 a) Proton beam halo hit map of the LHCb VELO detector module. b) Extent of the proton beam halo for different distances from the aperture. 4

1.3 a) Setup of the stand-alone LHCb VELO detector modules at CCC. The detector modules are in the integration zone between the green repeater boards. The Faraday Cup is positioned at the beam exit. b) Measured results for three different positions of the modules in the integration zone. It shows the average increase of the integrated ADC values in the PHI-sensor per readout event versus the proton beam intensity measured by the FC. 5

2.1 Dominating photon-matter interactions according to the atomic number Z and photon energy. For organic tissue Z=7 (red line), the Compton effect is the most common interaction with photons for the therapeutic energy range from 6 MeV to 25 MeV. (Modified after [12].) 13

2.2 Proton-matter interactions: a) Continuous slowing down (CSD) process via inelastic Coulomb interaction, b) Multiple Coulomb scattering (MSC) via elastic scattering with nucleus c) Inelastic nuclear interaction. [14] . 15

2.3 Proton mass stopping power S in water (black line) plotted against the energy based on Eq. 2.5. Additionally, the equivalent range (red line, Eq. 2.7), assuming the CSD approach, is plotted. [14] 17

2.4 Depth dose distribution in water of a photon beam (E_{ph}= 15 MeV), of a single Bragg-peak and of a spread-out Bragg peak (SOBP) of protons (E_{max}= 200 MeV). The target volume lies between the two dashed lines. The unwanted 'dose bath' of photons (dark grey area) can be spared by using protons. [21] 19

2.5 Concept of describing the pencil proton beam dose distribution. Dashed lines are 10% and 0.01% isodoses drawn to scale [23]. 21

2.6 Schematic picture of a cyclotron [15]. Protons are extracted from ionised gas (proton source). An alternating electric field is applied between two or four D-shaped electrodes (Dees) to accelerate the protons. 23
2.7 Setup of a double-scattering system used at the MGH Francis H. Burr Proton Beam Therapy Center [36]. 26
2.8 Double scattering and beam modulation system of the CCC. Beam is passing through the two scattering foils (A) and is shaped by the range shifter and modulation wheel (B, C). Beam monitoring ICs (F) and cross wires (G) to measure dose and profile. Nozzle and aperture (H) for final beam shaping. [37] 27
2.9 Deflection of the pencil beam via sweeper magnets in x- and y-direction of a scanning system. The layers (grey) are adapted to the three dimensional tumour volume (light grey lines). [38] 28
2.10 Schematic sketch of the nozzle used for pencil beam scanning at MGH. Quadrupole magnets control the beam size, a pair of scanning dipoles deflect the beam to the desired position and ion-chambers measure the dose, position and beam profiles. [15] 29
2.11 Schematic dose distribution for a target volume (white circle) for a single field delivered by a passive scattering and scanning system. More sparing of the healthy tissue of high dose levels can be achieved by scanning systems. [40] . . 29
2.12 Layout of the irradiation facility of the University of Birmingham, featuring the cyclotron vault, the high intensity irradiation area, and the operator control room. Two experimental rooms are dedicated for studies. These include studies for detectors used at ATLAS (room 2) or for Medical and Nuclear physics experiments (room 1). [47] 31
2.13 Dedicated experimental room with height adjustable table behind the final collimator for studies with the LHCb VELO detector modules. . . . 33

3.1 Ion beam passing through the parallel-plate ionisation chamber filled with nitrogen, which creates ion pairs accelerated towards the cathode and anode. [50] 39
3.2 a) Schematics of IC1 and IC2 of the PSI parallel-plate ionisation chambers b) Schematics of strip ionisation chamber. [50] 41
3.3 Cross-sections of (a) radiographic silver halide film and (b) radiochromic EBT-3 film [59]. 44

3.4 a) N-type semiconductor b) P-type semiconductor 47
3.5 P-n junction and forming of the depletion layer. 48
3.6 a) P-n junction without voltage b) P-n junction with reverse bias voltage 49
3.7 a) Layout of a single cell of a hybrid pixel detector used for Medipix3 and Timepix3 b) Hybrid pixel matrix [74] 50

4.1 Overview of the complete LHCb VELO experiment at the LHC in CERN. There are 42 silicon detectors in total to pick out produced B mesons. [84] 53
4.2 Cross-section of a VELO silicon sensor of type $n^+ - in - n$. When ionising particles hit the bulk and create electron-hole pairs, the bias voltage depletes the sensor, so that electrons drift towards the implants. A SiO_2 layer forms an AC coupling to the strip implants. The Aluminium readout strips transport the signals to the front-end electronics via the routine layer. [89] 55
4.3 Schematics of the VELO R-sensor and PHI-sensor. Each sensor consists of 2048 readout strips. The R-sensor is structured in four sectors with radially oriented strips and the PHI-sensor consists of two sectors and angled strips. [84] 56
4.4 Picture of a VELO module used for beam monitoring in the Cockcroft Institute. 57
4.5 Schematic block diagram of the Beetle readout chip. Sampled analogue signals are amplified, shaped and stored in a buffer until a readout signal is received. [93] 59
4.6 Pulse shape of the output of the Beetle chips. The rise time t_r is not more than 25 ns and the remainder R has to be below 30% to meet the requirements of the LHC bunch-crossing. [93] 60
4.7 The layout plan of the TELL1 board with its major components. For the LHCb VELO system, the optical receiver card (ORX) is substituted by two more ARx cards. The LEMO connectors can be used to inject external trigger (see section 4.2). [97] 61
4.8 The main readout process with the electronic parts. A readout trigger is sent out by the TELL1 board via the Repeater board to the Beetle chips (violet squares). Modified after [84]. 63

4.9 Overview about the timing calibration on real beam data. A trigger decision T0 is done by the TFC system. The readout supervisor ODIN controls the readout of the TELL1 board. The time between the triggered event and the arrival of the readout trigger is exactly 4 µs (160 clock cycles). Hardware and cable delays need to be integrated. [103] . 65
4.10 a) The VELO detector modules embedded in a plastic case including the entrance and exit of the cooling and venting pipes b) Schematic of the airflow to guarantee a safe and smooth operation. Signal transmission to additional electronic parts is shown in Fig. 4.8. 67
4.11 Without the configuration of the cable and phase delay in clock cycles, header bits can spill over into the next channel of the link and affect the noise spectrum. 70
4.12 Introduced system to synchronise the proton bunch arrival of a medical accelerator. A readout decision is made, if the rising edge of the external trigger is within the first 0 to 8.3 ns (detected by the 120 MHz clock, shown by the grey lines) of the 40 MHz clock. Other triggers will get rejected. 71
4.13 Without synchronisation, the output pulse is sampled at random points (even negative points), decreasing the signal quality significantly. 72
4.14 Schematic representation of the NZS data stream produced by each VELO silicon sensor. The analogue signal is probed by the Beetle chips (each comprising 128 individual channels) and stored in an analogue pipeline implemented within chips. When a trigger signal is received, the analogue data is sent via long copper cables to the TELL1 boards for digitisation and processing. The digital resolution of the ADC is 10 bit. 74
4.15 Schematic representation of the raw NZS data processing pipeline. The solid rectangles represent algorithms. Pedestal bank and respective thresholds parameters are determined during special calibration runs. 75
4.16 Raw NZS data plotted as a function of readout chip channel. Apart from the offset (pedestal) there is a clear variation between analogue links (groups of 32 consecutive channels). 75

4.17 Pedestal bank evaluated for a selected sensor at the following (training) phase. After converging the following algorithm is deactivated and the pedestals become fixed and are subtracted from all subsequent events. 76
4.18 Raw NZS data after pedestal subtraction. Both the offset and the initial variation between analogue links are removed. 76
4.19 Architecture of the analysis mini-framework for the test beam data analysis. The output data can be stored as ROOT histograms and the reconstructed hits and trigger information is saved as a formatted text file. 77

5.1 Layout of the irradiation facility at the University of Birmingham, featuring the cyclotron vault, the high intensity irradiation area and the operator control room. The stand-alone setup of the VELO detector modules was built up in the room marked "VELO setup", where the beamline 4 (red line) leads to. Modified after [47]. 81
5.2 Setup of the VELO detector modules in the irradiation room. On top of the switching magnet, a laser was mounted to align the detector modules with the nozzle pipe, where the beam exits. 82
5.3 Synchronisation of the readout of the VELO detector and in-beam ion-chamber. A developed software trigger controls the simultaneous data acquisition of the VELO detector and the ion-chamber. The RF frequency of the cyclotron triggers the pulse generator, which injects readout triggers into the TELL1 board. 83
5.4 Comparison of the fitted entries of protons in EBT3 GAFchromic film relative to the x-axis for the different collimator diameters. The two dashed lines at x=-8 mm and x=8 mm represent the aperture opening of the VELO detector modules. 88
5.5 Entries for x $>$ 8 mm and x < -8 *mm* related to the total number of protons and fitted linearly for different collimator sizes. 90
5.6 Histogram of the distribution of ADC counts of the R1-sensor of one data set. A 7 mm collimator with a proton beam current of 0.06 nA was used. 92

5.7 Image of the two modules for a 7 mm collimator. It shows the total ADC counts per registered hits summed up for the R- and PHI-sensor. The detector modules are saturated. 92
5.8 Phase scan over the RF frequency period of 54.9 ns. At 22.5 ns, the highest amount of hits was recorded for all four sensors. 95
5.9 Average hits of the VELO sensors per absolute charge measured by the electrometer using a 15 mm collimator. 97
5.10 Hits of the VELO sensors per absolute charge measured by the electrometer using a 15 mm collimator. 98
5.11 Hits of the VELO sensors per corrected absolute charge measured by the electrometer using a 15 mm collimator. 99
5.12 Average hits of the VELO sensors per corrected absolute charge measured by the electrometer using a 15 mm collimator. 100
5.13 Average hits of the VELO sensors per absolute charge measured by the electrometer using a 10 mm collimator. 100
5.14 Hits of the VELO sensors per absolute charge measured by the electrometer using a 10 mm collimator. Beam current fluctuations are observed during the last three runs. 101
5.15 Average hits of the VELO sensors per absolute charge measured by the electrometer using a 7 mm collimator. 102
5.16 Hits of the VELO sensors per absolute charge measured by the electrometer using a 7 mm collimator. 102
5.17 Schematic strip geometry of the R- and PHI-sensor. The green routing lines collect the generated charge from the strips. For the R-sensor the routing lines are perpendicular to the strips and parallel to the PHI-sensor strips. [95] 103
5.18 Hit distribution using a 20 mm collimator of the R1- and PHI1-sensor for module 1. The PHI-sensor is mirrored to the R-sensor for visualisation only. Sudden signal spikes are observed for the R- and the PHI-sensor. . 104
5.19 Total hits of the R1-sensor relative to the radius. A sudden spike in signal at 13 mm and a sudden fall at 21 mm is observed indicating a wrong channel ordering (cp. with Fig. 5.17). 104
5.20 Measured angular positions of the hits of the inner and outer sector of the PHI1-sensor. 105

5.21 The proton beam on the R1- and R2-sensor. The beam spot is predominantly in the upper right sector. . . . 107
5.22 Measured beam profile for the R1- and R2-sensor. More hits were registered by the R2-sensor. . . . 108
5.23 Beam profile for the R1- and R2-sensor. More hits were registered by the R2-sensor up to r=11 mm. . . . 109
5.24 Strip map of the hits on the PHI1- and PHI2-sensor. . . . 109
5.25 Measured angular distribution in Degrees of the hits by the PHI1- and PHI2-sensor. . . . 110
5.26 Measured angular positions in Degrees of the hits of the inner and outer sector of the PHI2-sensor. . . . 111
5.27 Pixel map of the correlated hits for the two modules. . . . 111
5.28 Strip map of the hits of 28 MeV protons on the a) R1- and R2-sensor and b) PHI1- and PHI2-sensor for a 10 mm collimator. . . . 113
5.29 a) Hits of 28 MeV protons against the radius of the R1- and R2-sensor. b) Pixel map of the correlated hits for the two modules. . . . 113
5.30 Strip map of the hits of 18 MeV protons on the a) R1- and R2-sensor and b) PHI1- and PHI2-sensor for a 10 mm collimator. . . . 114
5.31 a) Hits of 18 MeV protons against the radius of the R1- and R2-sensor. b) Pixel map of the correlated hits for the two modules. . . . 114
5.32 Images of the beam for different collimators for a) day 3 and b) day 2. The removing of the scattering foil at day 3 resulted in distorted beam profiles. . . . 115
5.33 Comparison of the beam profiles of day 3 measured by film and the VELO detector R-sensors: a) 10 mm collimator. b) 15 mm collimator. . 116
5.34 Comparison of the beam profiles of day 2 measured by film, the VELO detector R-sensors and the GEANT4 simulation: a) 10 mm collimator. b) 15 mm collimator. . . . 116

6.1 Comparison of the beam current measurements of different collimators with the established correction factor from GEANT4 simulations (dashed line). . . . 120
6.2 Expected fluence of LHC Run II for the LHCb VELO detector. [113] . . 124

7.1 Sketch of the CCC proton therapy beamline. The blue box marks the integration zone of the VELO detector modules. They are placed between the modulator box (orange) and diagnostic box (green). The present aluminium pipe will be removed. Adapted to [9]. 134

8.1 The VELOPix detector for the LHC upgrade. Each side has two sensors (red), read out by the newly developed ASICs (orange) cooled by the micro-channels in a silicon substrate (blue) [122]. 144

List of Tables

2.1 **Cyclotron time structure and beam parameters.** 32

3.1 **Overview of detectors used in medical accelerators [6, 51].** . . . 38

4.1 **Characteristics of the VELO detector modules.** 55
4.2 **Integrated ADC count values with standard deviation for different Peak-to-peak Voltages V_{pp} for the non-synchronised readout and synchronised readout with the pulsed LD-1060.** 73

5.1 **Summary of the different settings of the cyclotron.** 85
5.2 **FWHM, Percentage % of the entries larger than 8 mm for different collimator sizes and k_{norm}.** 89
5.3 **Comparison of the ratios between the gradients of the linear fit (Fig. 5.5) of different collimator sizes to the 7 mm collimator to the calculated correction factors based on Eq. 5.10.** 90
5.4 **Extract of the data collection file of a run with a 7 mm collimator. The registered hits are shown for two events for the R2-sensor and the PHI1-sensor.** 93
5.5 **Reduction of hits (H) by the spill-over ($\mathrm{H_{SO}}$) and clustering ($\mathrm{H_{Clst}}$) algorithm for the 15 mm collimator with a beam current of 1 nA for each sensor. The relative difference $\mathrm{D_{SO}} = \mathrm{H_{SO}}/\mathrm{H}$ and $\mathrm{D_{Clst}} = \mathrm{H_{Clst}}/\mathrm{H}$ is also shown.** 94
5.6 **Relative standard deviation in % of the hits of the VELO sensors for different beam currents for a 15 mm collimator.** 97
5.7 **Uncorrected and time corrected relative standard deviation in % of the absolute charge measured by the electrometer for the 15 mm collimator.** 98

6.1 **Gradients of the linear fit (cp. Fig. 6.1) of different collimator sizes for all four sensors.** 120

6.2 **Ratios of the linear fit (cp. Fig. 6.1) of different collimator sizes for all four sensors compared to the determined correction factors k_{corr}.** 121

Bibliography

[1] Cancer Research UK. Worldwide cancer statistics. Website, 2020. Online available at `https://www.cancerresearchuk.org/health-professional/cancer-statistics/worldwide-cancer`, last visit: 31/05/2020.

[2] World Health Organisation. Global Cancer Observatory (GCO). Website, 2020. Online available at `http://gco.iarc.fr/`, last visit: 31/05/2020.

[3] Cancer Research UK. Treatment for cancer. Website, 2020. Online available at `https://www.cancerresearchuk.org/about-cancer/cancer-in-general/treatment`, last visit: 31/05/2020.

[4] Robert R Wilson. Radiological use of fast protons. *Radiology*, 47(5):487–491, 1946.

[5] Thomas R Bortfeld and Jay S Loeffler. Three ways to make proton therapy affordable. *Nature News*, 549(7673):451, 2017.

[6] Peter Fork. Lecture Notes on Beam Instrumentation and Diagnostics. *Joint University Accelerator School*, 2017.

[7] G Casse et al. LHCb: A LHCb-VELO module as beam quality monitor for proton therapy beam at the Clatterbridge Centre for Oncology. In *Conference: Workshop" Physics for Health in Europe"*, number Poster-2010-140, 2010.

[8] O Actis, D Meer, and S König. Precise on-line position measurement for particle therapy. *Journal of Instrumentation*, 9(12):C12037, 2014.

[9] Andrzej Kacperek. Protontherapy of eye tumours in the UK: A review of treatment at Clatterbridge. *Applied Radiation and Isotopes*, 67:378–386, 2009.

[10] Tomasz Cybulski. *A Non-Invasive Beam Current Monitor for a Medical Accelerator*. PhD thesis, University of Liverpool, Liverpool, 2017.

[11] Frank Herbert Attix. *Introduction to radiological physics and radiation dosimetry*. John Wiley & Sons, Weinheim, 2008.

[12] Wolfgang Demtröder. *Experimentalphysik 4*, volume 4. Springer, Berlin, 2005.

[13] Hans Bethe. Zur Theorie des Durchgangs schneller Korpuskularstrahlen durch Materie. *Annalen der Physik*, 397:325–400, 1930.

[14] Wayne D Newhauser and Rui Zhang. The physics of proton therapy. *Physics in Medicine & Biology*, 60(8):R155, 2015.

[15] Harald Paganetti. *Proton therapy physics*. CRC press, Boston, 2nd edition, 2018.

[16] Felix Bloch. Zur Bremsung rasch bewegter Teilchen beim Durchgang durch Materie. *Annalen der Physik*, 408(3):285–320, 1933.

[17] Robley Dunglison Evans and RD Evans. The atomic nucleus. 1955.

[18] Thomas Bortfeld. An analytical approximation of the Bragg curve for therapeutic proton beams. *Medical Physics*, 24:2024–2033, 1997.

[19] Thomas Bortfeld and Wolfgang Schlegel. An analytical approximation of depth - dose distributions for therapeutic proton beams. *Physics in Medicine and Biology*, 41:1331–1339, 1996.

[20] Katia Parodi and Thomas Bortfeld. A filtering approach based on gaussian-powelaw convolutions for local PET verification of proton radiotherapy. *Physics in Medicine and Biology*, 51:1991, 2006.

[21] Bettina Schaffner. *Range precision of therapeutic proton beams*. PhD thesis, Swiss Federal Institute of Technology, Zürich, 1997.

[22] Helmut Wiedemann. *Particle accelerator physics*. Springer, Berlin, 2015.

[23] Bernard Gottschalk et al. On the nuclear halo of a proton pencil beam stopping in water. *Physics in Medicine & Biology*, 60(14):5627, 2015.

[24] E Pedroni et al. Experimental characterization and physical modelling of the dose distribution of scanned proton pencil beams. *Physics in Medicine & Biology*, 50(3):541, 2005.

[25] Wilhelm Conrad Röntgen. On a new kind of rays. *Science*, 3(59):227–231, 1896.

[26] Gustaf Ising. Prinzip einer Methode zur Herstellung von Kanalstrahlen hoher Voltzahl. *Ark. Mat. Astron. Fys.*, 18:1–4, 1924.

[27] Rolf Wideröe. Über ein neues Prinzip zur Herstellung hoher Spannungen. In *Arbeiten aus dem Elektrotechnischen Institut der Technischen Hochschule Aachen*, pages 157–176. Springer, 1929.

[28] David I Thwaites and John B Tuohy. Back to the future: the history and development of the clinical linear accelerator. *Physics in Medicine & Biology*, 51(13):R343, 2006.

[29] Ernest O Lawrence and Niels E Edlefsen. On the production of high speed protons. *Science*, 72(1867):376, 1930.

[30] John H Lawrence. Proton irradiation of the pituitary. *Cancer*, 10(4):795–798, 1957.

[31] Herman Winick and Sebastian Doniach. *Synchrotron radiation research*. Springer Science & Business Media, Berlin, 2012.

[32] Ugo Amaldi. Cancer therapy with particle accelerators. *Nuclear Physics A*, 654(1-2):C375–C399, 1999.

[33] PTCOG. Patient statistics. Website, 2020. Online available at `https://ptcog.ch/index.php/patient-statistics`, last visit: 31/05/2020.

[34] WJGM Kleeven et al. The IBA superconducting synchrocyclotron project S2C2. In *Proc. Cyclotrons*, pages 1–5, 2013.

[35] Tianyu Zhao et al. Commissioning and initial experience with the first clinical gantry-mounted proton therapy system. *Journal of applied clinical medical physics*, 17(2):24–40, 2016.

[36] Michael Gotein. *Radiation Oncology: A Physicist's-Eye View*. Springer, Boston, 1st edition, 2008.

[37] J Yap et al. Beam characterisation studies of the 62 MeV proton therapy beamline at the Clatterbridge Cancer Centre. *Physica Medica*, 77:108–120, 2020.

[38] Hanno Krieger. *Beam Instrumentation and Diagnostics*. Vieweg und Teubner Verlag, Berlin, 2nd edition, 2012.

[39] Hanne M Kooy et al. A case study in proton pencil-beam scanning delivery. *International Journal of Radiation Oncology* Biology* Physics*, 76(2):624–630, 2010.

[40] Ben Clasie. Implementing a Proton Beam Scanning System within an Operating Clinical Facility. Technical report, Massachusetts General Hospital, 2012.

[41] Antony Lomax. Intensity modulation methods for proton radiotherapy. *Physics in Medicine and Biology*, 44:185–205, 1999.

[42] AJ Lomax. Intensity modulated proton therapy and its sensitivity to treatment uncertainties 1: the potential effects of calculational uncertainties. *Physics in Medicine & Biology*, 53(4):1027, 2008.

[43] AJ Lomax. Intensity modulated proton therapy and its sensitivity to treatment uncertainties 2: the potential effects of inter-fraction and inter-field motions. *Physics in Medicine & Biology*, 53(4):1043, 2008.

[44] Antje-Christin Knopf and Antony Lomax. In vivo proton range verification: a review. *Physics in Medicine & Biology*, 58(15):R131, 2013.

[45] Alexander Gerbershagen et al. A novel beam optics concept in a particle therapy gantry utilizing the advantages of superconducting magnets. *Zeitschrift für Medizinische Physik*, 26(3):224–237, 2016.

[46] Yoshiyuki Iwata et al. Superconducting Gantry for Carbon-Ion Radiotherapy. In *9th Int. Particle Accelerator Conf.(IPAC'18), Vancouver, BC, Canada, April 29-May 4, 2018*, pages 1232–1236. JACOW Publishing, Geneva, Switzerland, 2018.

[47] P. Allport et al. Recent results and experience with the Birmingham MC40 irradiation facility. *JINST*, 12:C03075–C03075, 2017.

[48] IAEA TRS-398. Absorbed Dose Determination in External Beam Radiotherapy: An International Code of Practice for Dosimetry based on Standards of Absorbed Dose to Water. Technical report, INTERNATIONAL ATOMIC ENERGY AGENCY, Vienna, 2006.

[49] F Osmic et al. Overview of the Beam diagnostics in the MedAustron Accelerator: Design choices and test Beam commissioning. In *2nd IPAC proceedings*, volume 1205201, page MOPPR002, 2012.

[50] Edited by R. Bailey. Proceedings of the CAS–CERN Accelerator School: Accelerators for Medical Applications. *CERN Yellow Reports: School Proceedings*, 2017.

[51] C. P. Karger et al. Dosimetry for ion beam radiotherapy. *Phys. Med. Biol.*, 55:R193, 2010.

[52] Pedro Andreo et al. *Fundamentals of Ionising Radiation Dosimetry*. Wiley-VCH Verlag GmbH & Co., Weinheim, Germany, 1st edition, 2017.

[53] G. F. Knoll. *Radiation Detection and Measurment*. John Wiley & Sons Inc., Hoboken, New Jersey, USA, 4th edition, 2010.

[54] Shixiong Lin et al. More than 10 years experience of beam monitoring with the Gantry 1 spot scanning proton therapy facility at PSI. *Med. Phys.*, 36:R303, 2009.

[55] S Giordanengo et al. The CNAO dose delivery system for modulated scanning ion beam radiotherapy. *Medical physics*, 42(1):263–275, 2015.

[56] C Courtois et al. Characterization and performances of a monitoring ionization chamber dedicated to IBA-universal irradiation head for Pencil Beam Scanning. *Nuclear Instruments and Methods in Physics Research Section A: Accelerators, Spectrometers, Detectors and Associated Equipment*, 736:112–117, 2014.

[57] Marco Durante, Elke Bräuer-Krisch, and Mark Hill. Faster and safer? FLASH ultra-high dose rate in radiotherapy. *The British journal of radiology*, 91(1082):20170628, 2018.

[58] O Actis et al. A comprehensive and efficient daily quality assurance for PBS proton therapy. *Physics in Medicine & Biology*, 62(5):1661, 2017.

[59] Joao Seco et al. Review on the characteristics of radiation detectors for dosimetry and imaging. *Phys. Med. Biol.*, 59:R303, 2014.

[60] Slobodan Devic. Radiochromic film dosimetry: Past, present, and future. *Phys. Med.*, 27:122–34, 2010.

[61] Slobodan Devic et al. Linearization of dose-response curve of the radiochromic film dosimetry system. *Med. Phys.*, 39:4850–7, 2012.

[62] P. Hofmann. *Solid State Physics : An Introduction.* John Wiley & Sons, Berlin, 2015.

[63] James D. Patterson and Bernard Bailey. *Solid-state physics : Introduction to the theory.* Springer, Cham, 2018.

[64] Joginder Singh Galsin. Chapter 14 - Semiconductors. In Joginder Singh Galsin, editor, *Solid State Physics*, pages 299 – 319. Academic Press, 2019.

[65] Philip Allport. Applications of silicon strip and pixel-based particle tracking detectors. *Nature Reviews Physics*, pages 1–10, 2019.

[66] ATLAS Collaboration. Technical design report for the ATLAS inner tracker strip detector. Technical report, CERN, Geneva, 2017.

[67] Mara Bruzzi. Novel silicon devices for radiation therapy monitoring. *Nuclear Instruments and Methods in Physics Research Section A: Accelerators, Spectrometers, Detectors and Associated Equipment*, 809:105–112, 2016.

[68] Simona Giordanengo and Hugo Palmans. Dose detectors, sensors, and their applications. *Medical Physics*, 45(11):e1051–e1072, 2018.

[69] AR Jones. The application of some direct current properties of silicon junction detectors to γ-ray dosimetry. *Physics in Medicine & Biology*, 8(4):451, 1963.

[70] G. McAuley et al. Evaluation of the dosimetric properties of a diode detector for small field proton radiosurgery. *Journal of applied clinical medical physics*, 16(6):51–64, 2015.

[71] PD Bradley, AB Rosenfeld, and M Zaider. Solid state microdosimetry. *Nuclear Instruments and Methods in Physics Research Section B: Beam Interactions with Materials and Atoms*, 184(1-2):135–157, 2001.

[72] F Gómez et al. Measurement of carbon ion microdosimetric distributions with ultrathin 3D silicon diodes. *Physics in Medicine & Biology*, 61(11):4036, 2016.

[73] C. Granja et al. Resolving power of pixel detector Timepix for wide-range electron, proton and ion detection. *Nuclear Instruments and Methods in Physics Research Section A: Accelerators, Spectrometers, Detectors and Associated Equipment*, 908:60–71, 2018.

[74] Maurice Garcia-Sciveres and Norbert Wermes. A review of advances in pixel detectors for experiments with high rate and radiation. *Reports on Progress in Physics*, 81(6):066101, 2018.

[75] HF-W. Sadrozinski et al. Ultra-fast silicon detectors. *Nuclear Instruments and Methods in Physics Research Section A: Accelerators, Spectrometers, Detectors and Associated Equipment*, 730:226–231, 2013.

[76] N. Cartiglia et al. Performance of ultra-fast silicon detectors. *Journal of instrumentation*, 9(02):C02001, 2014.

[77] N. Cartiglia et al. Beam test results of a 16 ps timing system based on ultra-fast silicon detectors. *Nuclear Instruments and Methods in Physics Research Section A: Accelerators, Spectrometers, Detectors and Associated Equipment*, 850:83–88, 2017.

[78] Jacinta Yap, Navrit Bal, et al. Beam characterisation using Medipix3 and EBT3 film at the Clatterbridge Proton Therapy Beamline. In *Proc. 10th International Particle Accelerator Conference (IPAC'19), Melbourne, Australia, 19 - 24 May 2019, 2019*, page THPMP033, July 2019.

[79] L Opalka et al. 3D measurement of the radiation distribution in a water phantom in a hadron therapy beam. *Journal of Instrumentation*, 7(01):C01085, 2012.

[80] S. Levasseur et al. Time-Resolved Transverse Beam Profile Measurements with a Rest Gas Ionisation Profile Monitor Based on Hybrid Pixel Detectors. In *Proc. 9th International Particle Accelerator Conference (IPAC'18), Vancouver, BC, Canada, April 29-May 4, 2018*, pages 2361–2364, June 2018.

[81] Tony Price et al. Expected proton signal sizes in the PRaVDA range telescope for proton Computed Tomography. *Journal of Instrumentation*, 10(05):P05013, 2015.

[82] JT Taylor et al. Proton tracking for medical imaging and dosimetry. *Journal of Instrumentation*, 10(02):C02015, 2015.

[83] C Talamonti et al. Dosimetric characterization with 62 MeV protons of a silicon-segmented detector for 2D dose verifications in radiotherapy. *Nuclear Instruments and Methods in Physics Research Section A: Accelerators, Spectrometers, Detectors and Associated Equipment*, 596(1):126–130, 2008.

[84] The LHCb Collaboration. The LHCb detector at LHC. *Journal of Instrumentation*, 3(08):S08005, 2008.

[85] The LHCb Collaboration. Technical Design Report Reoptimized Detector Design and Performance. Technical report, CERN, Geneva, 2003.

[86] The LHCb Collaboration. LHCb VELO (VErtex LOcator: Technical Design Report. Technical report, CERN, Geneva, 2001.

[87] A.G. Bates. The LHCb VELO: Status and Upgrade Developments. Technical report, CERN, Geneva, 2001.

[88] The LHCb Collaboration. Further optimisation of the VELO material. Technical report, CERN, Geneva, 2001.

[89] Aras Papdelis. *Characterisation and commissioning of the LHCb VELO detector*. PhD thesis, Vrije University, Amsterdam, 2009.

[90] The LHCb Collaboration. R-measuring sensor. Technical report, CERN, Geneva, 2004.

[91] The LHCb Collaboration. Technical Design Report Re-optimized Detector Design and Performance. Technical report, CERN, Geneva, 2003.

[92] The LHCb Collaboration. Phi-measuring sensor. Technical report, CERN, Geneva, 2004.

[93] Sven Loechner. The Beetle Reference Manual – chip version 1.3, 1.4 and 1.5. Technical report, CERN, Geneva, 2006.

[94] B. Verlaat. CO2 cooling for the LHCb-VELO experiment at CERN. In *8th IIF/IIR Gustav Lorentzen Conference on Natural Working Fluids*, 2008.

[95] The LHCb Collaboration. Performance of the LHCb Vertex Locator. Technical report, CERN, Geneva, 2014.

[96] Guido Haefeli. Specification and common readout board for LHCb. Technical report, CERN, Geneva, 2003.

[97] Guido Haefeli. *Contribution to the development of the acquisition electronics for the LHCb experiment.* PhD thesis, EPFL, Lausanne, 2004.

[98] Tomasz Szumlak. Application of the Beetle Cross Talk Correction algorithm for the VELO detector. Technical report, CERN, Geneva, 2009.

[99] Guido Haefeli. LHCb VELO and ST clusterization on TELL1. Technical report, CERN, Geneva, 2006.

[100] Tomasz Szumlak. Reconstruction of Cluster Positions in the LHCb VELO. Technical report, CERN, Geneva, 2007.

[101] Flavio Fontanelli. CC-PC Gluecard Application and User's Guide. Technical report, CERN, Geneva, 2005.

[102] The LHCb Collaboration. LHCb Trigger System Technical Design Report. Technical report, CERN, Geneva, 2003.

[103] Kazu Akiba. Description of the VELO timing system and its configuration. Technical report, CERN, Geneva, 2011.

[104] Richard Jacobsson. Timing and Fast Control. Technical report, CERN, Geneva, 2001.

[105] Richard Jacobsson. The final LHCb readout supervisor "ODIN". Technical report, CERN, Geneva, 2002.

[106] R. Schnuerer et al. Implementation of a Non-invasive Online Beam Monitor at a 60 MeV Proton Therapy Beamline. In *9th IPAC proceedings, Vancouver, Canada*, 2018.

[107] T Szumlak and C Parkes. Description of the Vetra Project and its Application for the VELO Detector. Technical Report LHCb-2008-022. CERN-LHCb-2008-022, CERN, Geneva, 2008.

[108] R. Schnuerer et al. Development of the LHCb VELO Detector Modules into a Standalone, Non-Invasive Online Beam Monitor for Medical Accelerators. *Instr.*, 3:1–12, 2018.

[109] Markus Friedl. Energy Loss. Website, 2001. Online available at `http://www.hephy.at/user/friedl/diss/html/node10.html`, last visit: 24/02/2020.

[110] NIST. PSTAR. Website, 2019. Online available at `https://physics.nist.gov/PhysRefData/Star/Text/PSTAR-t.html`, last visit: 24/02/2020.

[111] Guido Haefeli and Alex Gong. VELO and ST non-zero suppressed bank data format. Technical report, CERN, Geneva, 2008.

[112] Slobodan Devic et al. Dosimetric properties of improved GafChromic films for seven different digitizers. *Medical physics*, 31(9):2392–2401, 2004.

[113] A Affolder et al. Radiation damage in the LHCb Vertex Locator. *Journal of Instrumentation*, 8(08):P08002, 2013.

[114] Jan Hrbacek et al. Practice patterns analysis of ocular proton therapy centers: the international OPTIC survey. *International Journal of Radiation Oncology*Biology*Physics*, 95(1):336–343, 2016.

[115] Sudharsan Srinivasan and Pierre-André Duperrex. Dielectric-filled reentrant cavity resonator as a low-intensity proton beam diagnostic. *Instruments*, 2(4):24, 2018.

[116] N Kumar et al. Non-invasive beam profile monitor for medical accelerators. *Physica Medica*, 73:173–178, 2020.

[117] Konrad Pawel Nesteruk et al. A system for online beam emittance measurements and proton beam characterization. *Journal of instrumentation*, 13(01):P01011, 2018.

[118] Rajesh Pidikiti et al. Commissioning of the world's first compact pencil-beam scanning proton therapy system. *Journal of applied clinical medical physics*, 19(1):94–105, 2018.

[119] The LHCb collaboration. LHCb VELO upgrade technical design report. 2013.

[120] Karol Hennessy. LHCb VELO upgrade. *Nuclear Instruments and Methods in Physics Research Section A: Accelerators, Spectrometers, Detectors and Associated Equipment*, 845:97–100, 2017.

[121] M Van Beuzekom et al. VeloPix ASIC development for LHCb VELO upgrade. *Nuclear Instruments and Methods in Physics Research Section A: Accelerators, Spectrometers, Detectors and Associated Equipment*, 731:92–96, 2013.

[122] LHCb VELO Group. The LHCb VELO upgrade. Website, 2020. Online available at `https://lbtwiki.cern.ch/bin/view/VELOVeloUpgradePresentationMaterial`, last visit: 02/10/2020.